

GENERATION OF OPTIMIZED VORONOI BASED INTERIOR STRUCTURES
FOR IMPROVED MECHANICAL PROPERTIES

A THESIS SUBMITTED TO
THE GRADUATE SCHOOL OF NATURAL AND APPLIED SCIENCES
OF
MIDDLE EAST TECHNICAL UNIVERSITY

BY

ANIL CAN ÖNCEL

IN PARTIAL FULFILLMENT OF THE REQUIREMENTS
FOR
THE DEGREE OF MASTER OF SCIENCE
IN
MECHANICAL ENGINEERING

SEPTEMBER 2019

Approval of the thesis:

**GENERATION OF OPTIMIZED VORONOI BASED INTERIOR
STRUCTURES FOR IMPROVED MECHANICAL PROPERTIES**

submitted by **ANIL CAN ÖNCEL** in partial fulfillment of the requirements for the degree of **Master of Science in Mechanical Engineering Department, Middle East Technical University** by,

Prof. Dr. Halil Kalıpçılar
Dean, Graduate School of **Natural and Applied Sciences**

Prof. Dr. M. A. Sahir Arıkan
Head of Department, **Mechanical Engineering**

Assist. Prof. Dr. Ulaş Yaman
Supervisor, **Mechanical Engineering, METU**

Examining Committee Members:

Assoc. Prof. Dr. Melik Dölen
Mechanical Engineering, METU

Assist. Prof. Dr. Ulaş Yaman
Mechanical Engineering, METU

Assoc. Prof. Dr. Merve Erdal
Mechanical Engineering, METU

Assist. Prof. Dr. Orkun Özşahin
Mechanical Engineering, METU

Assist. Prof. Dr. Recep Muhammet Görgülüarslan
Mechanical Engineering, TOBB ETÜ

Date: 05.09.2019

I hereby declare that all information in this document has been obtained and presented in accordance with academic rules and ethical conduct. I also declare that, as required by these rules and conduct, I have fully cited and referenced all material and results that are not original to this work.

Name, Surname: Anıl Can Öncel

Signature:

ABSTRACT

GENERATION OF OPTIMIZED VORONOI BASED INTERIOR STRUCTURES FOR IMPROVED MECHANICAL PROPERTIES

Öncel, Anıl Can
Master of Science, Mechanical Engineering
Supervisor: Assist. Prof. Dr. Ulaş Yaman

September 2019, 127 pages

General design approaches are related with and inspired by natural examples. Since evolution itself pushes beings to their full potentials in the most efficient way, it is important for us to understand, observe and mimic the nature itself. In this study, naturally inspired internal structures are constructed by using hollow Voronoi cells and models are optimized to meet the design requirements. For this purpose, design volume firstly undergoes topology optimization with specific load and support conditions and the volume is divided into several density regions. Cell generation algorithm advances according to the average Von-Misses and principal stress values and deflections in these corresponding regions. The number of Voronoi sites in structurally critical regions is higher than other regions. Thus, the results of the optimization are reflected on the models. Since the Voronoi based interior has high porosity, the selected test models are manufactured via Fused Filament Fabrication process. The proposed approach is tested on several cases and the performance of the method is compared with respect to the cases having random Voronoi site distributions and regular infill patterns. According to the test results, strength-to-weight ratios of the tested artefacts are enhanced.

Keywords: Additive Manufacturing, Voronoi Cells, Topology Optimization

ÖZ

GELİŞTİRİLMİŞ MEKANİK ÖZELLİKLER İÇİN OPTİMİZE EDİLMİŞ VORONOI TABANLI İÇ YAPILARIN ÜRETİMİ

Öncel, Anıl Can
Yüksek Lisans, Makina Mühendisliği
Tez Danışmanı: Dr. Öğr. Üyesi Ulaş Yaman

Eylül 2019, 127 sayfa

Genel tasarım yaklaşımları doğada karşılaşılan örneklerle ilgilidir ve bunlardan ilham alır. Evrimin kendisi, varlıkları tam potansiyellerine en verimli şekilde zorladığından, doğanın kendisini anlamamız, gözlemlememiz ve taklit etmemiz önemlidir. Bu çalışmada, doğal yapılardan ilham alan iç yapılar, içi boş Voronoi hücreleri kullanılarak inşa edilmiştir ve modeller, tasarım gereksinimlerini karşılamak üzere optimize edilmiştir. Bu amaçla, tasarım modeli öncelikle belirli yük ve destek koşullarıyla topoloji optimizasyonuna tabi tutulur ve ardından model hacmi birkaç yoğunluk bölgesine bölünür. Hücre üretimi algoritması, ortalama Von Mises ve ana stres değerleri ile beraber bölgelerdeki deplasman değerlerine göre ilerler ve bu sebep ile yapısal olarak kritik bölgelerdeki Voronoi tohum sayısı diğerlerinden daha fazladır. Böylelikle optimizasyonun sonuçları modellere yansır. Voronoi bazlı iç yapı yüksek gözenekliliğe sahip olduğundan, seçilen test modelleri FFF tipi eklemeli üretim işlemi ile üretilmiştir. Önerilen yaklaşım belirlenen modeller üzerinde test edilmiş ve yöntemin başarımı rastgele Voronoi alan dağılımına ve düzenli dolgu desenlerine sahip olan modeller ile karşılaştırılmıştır. Test sonuçlarına göre, test edilen parçaların güç-ağırlık oranları iyileştirilmiştir.

Anahtar Kelimeler: Eklemeli İmalat, Voronoi Hücreleri, Topoloji Optimizasyonu

To my mother...

ACKNOWLEDGEMENTS

I would like to thank to my supervisor Assist. Prof. Dr. Ulaş Yaman for invaluable helps and for giving chance to me to work with him. Besides, technical infrastructure of this work is supported by the Aircraft integration Engineering Department of ASELSAN. Thus, the author would like to thank a lot to HAEMM of ASELSAN for their superior support during the work.

I would also like to thank to my mother for her golden guidance and supports.

TABLE OF CONTENTS

ABSTRACT	v
ÖZ	vii
ACKNOWLEDGEMENTS	x
TABLE OF CONTENTS	xi
LIST OF TABLES	xiii
LIST OF FIGURES	xiv
LIST OF ABBREVIATIONS	xxi
LIST OF SYMBOLS	xxiii
1. INTRODUCTION	1
1.1. General Concept	1
1.2. State of the art.....	3
1.3. Motivation	6
1.4. Objective	7
1.5. Content	8
2. LITERATURE REVIEW	11
2.1. Introduction	11
2.2. Voronoi Studies and Applications.....	11
2.3. Automated Methodologies and Algorithms in AM.....	16
2.4. Porous Regular Infills.....	22
2.5. Porous Irregular Infills	31
2.6. Multi-Material Porous Infills.....	42
3. METHODOLOGY 2.5D	47

3.1. Introduction.....	47
3.2. Manual 2.5D Test.....	47
3.2.1. Proposed Approach and Test Cases	47
3.2.2. Models	55
3.2.3. Limitations of Manual 2.5D Test and Possible Future Directions	60
3.3. Auto 2.5D Test.....	61
3.3.1. Proposed Approach and Test Cases	61
3.3.2. Models	68
3.3.3. Experiments.....	74
3.3.4. Limitations of Auto 2.5D Test and Possible Future Directions	91
4. METHODOLOGY 3D	95
4.1. Introduction.....	95
4.2. Proposed Approach and Test Cases	95
4.3. Models.....	101
4.4. Limitations of Methodology 3D and Possible Future Directions	115
5. CONCLUSIONS & FUTURE WORKS	119
5.1. Conclusions.....	119
5.2. Future Works.....	120
REFERENCES	123

LIST OF TABLES

TABLES

Table 3.1. FEA results of beam models.	58
Table 3.2. Results of FEA.	59
Table 3.3. Main aspects of the algorithm [61].	62
Table 3.4. Three point bending beam system, dimensions of 120x30x10 mm [61].	70
Table 3.5. Cantilever beam system, dimensions of 80x45x10 mm [61].	70
Table 3.6. Compression beam system, dimensions of 100x50x10 mm [61].	70
Table 3.7. Weight measurements of the printed beams.	77
Table 3.8. Results of the tests [61].	78
Table 3.9. Properties of the models at the limit loads [61].	79
Table 3.10. Weights of the printed artefacts.	81
Table 3.11. Results of the tests.	83
Table 3.12. Properties of the models at the limit loads.	84
Table 3.13. Properties of the models at the limit loads.	86
Table 4.1. Bounding box dimensions of the 3D models.	101
Table 4.2. Expected performances of the close shell 3D models.	107
Table 4.3. Deflection comparisons of the 3D close-shell and spongy models.	113
Table 4.4. Weight reduction and performance comparisons of the 3D close shell and spongy models.	113

LIST OF FIGURES

FIGURES

Figure 1.1. Voronoi patterns in nature; thirsty dirt (top left), skin of a giraffe (top right), flippers of a sea turtle (bottom left) and wings of a fly (bottom right).....	5
Figure 1.2. Voronoi formations in 2D (top row) and in 3D (bottom row). Left column: five Voronoi seeds are initially generated. Middle column: Voronoi cells start to grow and intersect with each other. Right column: resultant Voronoi cells.	6
Figure 2.1. 2D CfCVDT mesh examples [15].....	12
Figure 2.2. Territorial behavior of fish and resultant Voronoi pattern [17].	13
Figure 2.3. 3D Voronoi bone tissue model [7].	15
Figure 2.4. Deformed cylinder models from left to right; deformed models, stationary printed artefacts, pneumatically deformed artefacts and differences between input poses and deformed artefacts [21].	17
Figure 2.5. Left, horse model that is able to stand alone by the help of tail touch together with two feet and printed artefact that is able to stand alone on its single feet. Right, big head T-Rex is able to stand alone due to precise center of gravity adjustment [23].....	18
Figure 2.6. Complex 3D mold of dragon and casted artefact [24].	19
Figure 2.7. Stress field of the model (left) and generated infill pattern (right) [6]....	21
Figure 2.8. A cantilever beam problem with boundary and load conditions (left), printed beam models by proposed and HOC method (right) [9].	23
Figure 2.9. Modeled arm model of the quadcopter: (a) Initial model, (b) result of regular TO, (c) truss like design, (d) proposed optimization [31].	25
Figure 2.10. Experimental results of uniform and non-uniform density brackets and printed artefacts [33].	26
Figure 2.11. Cantilever beam design: geometry and conditions (top left), TO result and cell distribution (top right), printed artefacts (bottom) [35].	28

Figure 2.12. Three point bending beam models with different infills (top) and experimental validation (bottom) [10].	29
Figure 2.13. Irregular lattice formation of the structure of New Balance base [40].	32
Figure 2.14. Printed artefacts with isotropic (green curve) and anisotropic (red curve) Voronoi infills (left) and load-displacement curves (right) [41].	33
Figure 2.15. Complex model of elastically deformable finger [11].	34
Figure 2.16. (a) Implant region and loading conditions, (b) projection of principal stresses for layer development, (c) printed artefact [44].	35
Figure 2.17. Left, orthotropic pipe model that protects the geometry of the inner pipe under same loading condition. Right, printed shoe base accordingly to strength, bending stiffness and density considerations [12].	36
Figure 2.18. Bunny and tooth interior comparison, left; traditional hollowing methodology. Right, proposed medial axis tree formation [46].	37
Figure 2.19. Proposed methodology is compared numerically with honeycomb-like interior and rhombic infill while keeping the volume fractions similar. Results state that there is an improved stiffness in both case [5].	38
Figure 2.20. Scaffold modelling stages. (a) Closed volume is populated. (b) 3D Voronoi cells are generated. (c) Voronoi cells are hollowed by scaled portions. (d) Voronoi contours are capture. (e) Captured inner and outer contours. (f) Contours are smoothed by mesh operations [47].	39
Figure 2.21. Proposed method chain. Left to right load and boundary conditions and optimization iterations are showed for Kitten model [48].	40
Figure 2.22. Left real bone with an implant is shown. Middle represents the CAD model of femur bone rod and right shows the printed model [49].	41
Figure 2.23. 3D model of Kitten (left), TPMS channels (middle) and injected material (right) [53].	44
Figure 2.24. The pipeline of OpenFab [54].	44
Figure 3.1. Left, 10 meters solid beam model is subjected 1kN force at each tip and simply supported at the middle. It is made of Al 2024 and weight of it is 13350 kg, modeled in Inspire 2016. Right, the dimensions of real F-16 Fighting Falcon with	

wingspan of 10 meters. Empty weight of the aircraft is 9207 kg and max. take-off weight is 21772 kg. Simplified beam system is shown on F-16 figure, dashed rectangle represents beam, red arrows show 1kN forces and flipped red triangle represents support region. 51

Figure 3.2. The evaluation of optimized truss-like structure. 52

Figure 3.3. Original optimized 3D beam model (above), smoothed model (middle) and current system (below). 53

Figure 3.4. Optimized Voronoi distribution with 600 Voronoi cells. Generation (a), comparison with actual TO result (b) and with smoothed TO result (c). Final applicable model (d). 54

Figure 3.5. Simple L beam, short arm is 100 mm, long arm is 150 mm, the sharp inner corner is filleted with the radius of 15 mm and the in-plane thickness is 10 mm. Tip of the longer arm is subjected to 100 N while short one is fixed. 54

Figure 3.6. Optimized 3D geometry by Inspire 2016 (top), 2D optimized Vorono infill pattern with 150 seeds in critical region, 50 seeds in low density region (bottom-left) and 2D random Voronoi infill pattern with total 200 seeds (bottom-right). 55

Figure 3.7. FEM of beams in stationary and deflected states, (a) Optimized Voronoi, (b) Smoothened and (c) Solid. 57

Figure 3.8. Deflection shape and stress distribution of random Voronoi L beam (first row) and optimized Voronoi L beam (second row). 59

Figure 3.9. General flow chart of the proposed method [61]. 61

Figure 3.10. Flow chart of the proposed method [61]. 64

Figure 3.11. Green circle represents objective region in which material (Voronoi site walls) should be maximized. Initial geometry (a) supplies limited amount of material to the corresponding region. Adding sites in the region increases the amount of material (b) [61]. 65

Figure 3.12. Cross points represent effective sites. (a) All Voronoi cells grow at the same rate in the beginning. (b) Effective cell growth is limited by the isocurves of high density regions. (c) Remaining cells continue to grow until they fully fill the low density regions [61]. 65

Figure 3.13. System review: (a) Support region (red), load region (blue) and boundary region (green), (b) TO result (black and white) [61].	69
Figure 3.14. Cross sections and the beam models of the two models are given. Randomly distributed Voronoi cells are shown in (a). Ratio between axial stress in the beam elements and yield stress of the material is visualized in (b). Optimized distributions of Voronoi cells are shown in (c). Ratio between axial stress in the beam elements and yield stress of the material is visualized in (d) [61].	71
Figure 3.15. Un-deformed geometries are represented with black lines and deformed shapes of the three point bending beam models are given, top for optimized Voronoi infills and bottom for random Voronoi infills. Local failure of three point bending beam with random infill at the loading tip is seen.	72
Figure 3.16. Un-deformed geometries are represented with black lines and deformed shapes of the cantilever beam models are given, left for optimized Voronoi infills and right for random Voronoi infills. Local failure of cantilever beam with random infill at the loading tip is seen.	73
Figure 3.17. Un-deformed geometries are represented with black lines and deformed shapes of the compression beam models are given, left for optimized Voronoi infills and right for random Voronoi infills. Random compression beam model deflects more in the left side, which causes asymmetric compression.	73
Figure 3.18. Experimental setup, random and optimized compression Voronoi beams.	75
Figure 3.19. Experimental setup, optimized three point bending Voronoi beam.	76
Figure 3.20. Experimental setup, random and optimized cantilever Voronoi beams.	76
Figure 3.21. Load-displacement curves of the test specimens. Red lines represent compression beams, blues are for simply supported beams and blacks are for cantilever beams while thinner ones for random Voronoi and thicker ones are for optimized Voronoi infills [61].	78
Figure 3.22. Failed artefacts, left column shows the random Voronoi infill artefacts, whereas; right column represents optimized Voronoi infill models. Local	

deformations are clearly seen in simply supported beam (top) and cantilever beam (middle) at the position of cross-head tip. 45 degree shear failure phenomenon is also found at the neck of compression beam with random Voronoi pattern (below). Dimensions of simply supported beams are 120x30x10 mm, cantilever beam are 80x45x10 and compression beam are 100x50x10 m..... 80

Figure 3.23. Load-displacement curves of the 3-point-bending beam test specimens. 82

Figure 3.24. Load-displacement curves of the cantilever beam test specimens. 82

Figure 3.25. Load-displacement curves of the compression beam test specimens. .. 83

Figure 3.26. Linear region for 3-point-bending beam test specimens. 85

Figure 3.27. Linear region for cantilever beam test specimens. 85

Figure 3.28. Linear region for compression beam test specimens. 86

Figure 3.29. Experimental setup of the compression beam with regular infill (top). Buckled compression beam top and side views (bottom). Buckling is seen at the narrow neck of the beam..... 88

Figure 3.30. Experimental setup of the simply supported beam with regular infill (top). Local deformation and failed view (bottom). Local deformation is seen at the middle top of the beam. 89

Figure 3.31. Experimental setup of the cantilever beam with regular infill (top). Local deformation and failed view (bottom). Local deformations are seen at the tip and bolted portions of the beam. 90

Figure 3.32. First experimental fixture of the cantilever beam and tight fitting boundary condition (top), shear deformation between printed artefact and test fixture (middle), revised fixture, plastic deformation and rotation around first bolt joint (bottom). 93

Figure 4.1. Bunny-Back compression model, Bunny model is loaded from the back of it (blue lines) and supported from the bottom (red dots). After TO, principal stress distribution (top left), Von-Misses distribution (top right) and deflection visualization (bottom left) is obtained. Critical mesh nodes are captured in bottom right. 97

Figure 4.2. Manufacturing modification process of the Bunny-Head model. a) the resultant 3D Voronoi Bunny model, b) 1st degree spongy Bunny model, c) 3rd degree Catmull-Clark Subdivided Bunny model, d) 0.8 mm constant wall thickness Bunny model and e) the final experimental Bunny-Head model.100

Figure 4.3. Bunny-Head model is supported at bottom (red dots) and loaded at head portion (blue lines). Principal stress, Von-Misses stress and deflection visualizations are given. Middle right represents the critical mesh nodes. Bottom row illustrates the distributions of random and optimized Voronoi seeds.102

Figure 4.4. Bunny-Back model is supported at bottom (red dots) and loaded at back portion (blue lines). Principal stress, Von-Misses stress and deflection visualizations are given. Middle right represents the critical mesh nodes. Bottom row illustrates the distributions of random and optimized Voronoi seeds.103

Figure 4.5. ATLAS model is supported at bottom (red lines) and loaded at top portion (blue lines). Principal stress, Von-Misses stress and deflection visualizations are given. Middle right represents the critical mesh nodes. Bottom row illustrates the distributions of random and optimized Voronoi seeds.105

Figure 4.6. Femur model is supported at bottom (red lines) and loaded at top portion (blue lines). Principal stress, Von-Misses stress and deflection visualizations are given. Bottom row represents the critical mesh nodes and Voronoi distributions for random and optimized mdoels.106

Figure 4.7. Manufacturing modifications of the Bunny-Back model. a) close-shell Voronoi model, b) 1st degree spongy model, c) 3rd degree spongy model, d) thickened model and e) experimental model.108

Figure 4.8. Manufacturing modifications of the ATLAS model. a) close-shell Voronoi model, b) 1st degree spongy model, c) 3rd degree spongy model, d) thickened model and e) experimental model.109

Figure 4.9. Manufacturing modifications of the Femur model. a) close-shell Voronoi model, b) 1st degree spongy model, c) 3rd degree spongy model, d) thickened model and e) experimental model.110

Figure 4.10. FEM of spongy models. Red lines represent loaded nodes and green dots represent supported nodes..... 112

Figure 4.11. End model of the Femur. First row shows the mesh openings and problematic meshes. Second row illustrates the same region after repairing operations. 114

Figure 4.12. Printed Femur models. First image shows the printing process of random Femur model. Second image illustrates the printed artefacts. Left Femur has random Voronoi infill and has crack around narrow neck that is marked by green. Right Femur has optimized Voronoi infill. Behind the left one, a failed Femur model is shown due to thin wall which is constant 0.4 mm. 117

LIST OF ABBREVIATIONS

ABBREVIATIONS

ABS	Acrylonitrille Butadiene Styrene
AM	Additive Manufacturing
BCC	Body Centered Cubic
BREPs	Boundary Representations
CAD	Computer Aided Design
CATE	Computer Aided Tissue Engineering
DLP	Direct Light Processing
EBM	Electron Beam Melting
FCC	Face Centered Cubic
FE	Finite Element
FEA	Finite Element Analysis
FEM	Finite Element Model
F2BCC	Combination of one FCC and two BCC
M4	Metric Four Bolt
PC	Polycarbonate
PCL	Polycaprolactone
PLA	Polylactic Acid
SF	Support Free
SIMP	Solid Isotropic Material with Penalization

SLA	Stereolithography
SLM	Selective Laser Melting
SSI	Simple Sequential Inhibition
STL	Standard Tessellation Language
TO	Topology Optimization
2.5D	Two and a Half Dimensional
3D	Three Dimensional
.stp	Standard for the Exchange of Product

LIST OF SYMBOLS

SYMBOLS

C	Compliance
K	Stiffness Matrix
m	Mass
P	Performance
p	Penalization Factor
u	Displacement
v	Volume
ρ	Density

CHAPTER 1

INTRODUCTION

1.1. General Concept

Additive manufacturing (AM) brings the opportunities of a new era which has not been totally discovered yet. The mentioned field changes the way of designing, process steps and even the materials that have been used so far. Due to its layer-by-layer manufacturing style, effective material usage, absence of mid-process steps and simplicity, we are able to deal with the most challenging problems. Among several benefits of AM, following ones are the concerns of this study.

First of them is about the complexity of parts which is often advantageous for special cases. The complexity of the part is not only about the outer shell shape or the geometry of it, which can be producible by using advanced traditional manufacturing techniques. It is also about the interior of it, including macro and micro levels. It has to be noted that overall desired mechanical properties of the model directly depend on macro- and micro-structures within it. Since AM takes no account of dealing with the manufacturing limitations, both outer shape and interior structure of the model is easily designed in task-to-task manner. Also, it gives the opportunity to modify internal structure of a desired part, which is sometimes impossible to achieve by conventional techniques. Although some casting, molding and forming systems are used for these purposes, AM systems are more effective in material, cost and time.

Second advantage is the speed of the manufacturing. General work flow of AM is minimized as follows;

- CAD
- STL Conversion

- Transfer to AM Machine and Manipulation of STL
- Machine Setup
- Build
- Removal
- Post Process
- Application [1]

It is realized that, the mid-processes like tool replacements, part orientations, detailed process planning steps and shifting the part from one machine to other one are not involved in the given process chain. Whereas, they are all required for the conventional subtractive methods. This single chain process has great importance on this study and will be covered in later chapters in great detail.

Third but not the last advantage is the compatibility of AM with the most effective designs. Compared to twenty years ago, we have created such mathematical models and computer aided software that enable us optimize our designs and get more realistic analysis results which are compatible with the real task scenarios. For instance, one may easily decrease the material amount of the part while keeping the mechanical behavior of it in a desired range; by simply using topology optimization algorithms. Another example is intentionally making the overall behavior of a model anisotropic to gain freedom of center of gravity location that is suitable for aerospace and aeronautics applications. The number of examples can be increased, but the main point is that in every situation, conventional manufacturing systems are somehow incapable in producing these kinds of parts. In addition, they consume large amounts of material, time and labor cost. On the contrary, AM, due to its nature, uses right amount of material and energy, and also it is compatible with recent technologies like reverse engineering and topology optimization.

Advances in AM draw attention to low density porous structures. Nowadays, low density parts with heterogeneous interior are frequently used to improve the efficiency of the parts. Since AM overcomes the problems related with geometric complexity,

use of AM becomes popular among other manufacturing techniques. Compared to other manufacturing techniques, there are several cons and pros of AM, however the subjects covered above are the most related AM advantages on heterogeneous interiors and their requests. Honeycomb panels, composite parts, and lattice structures are the most common low-density porous structures used in engineering applications. Their proved excellent mechanical behaviors and their light weight make them great candidates against solid counterparts that are produced by conventional manufacturing techniques. This is the reason that low density porous structures are used extensively in civil, biomedical, aerospace and mechanical engineering applications.

As it is introduced here, this study focuses on the advantages of AM and porous structures. Following sections narrow down the subject of manner and give detailed information about the study.

1.2. State of the art

In recent years, design optimization and efficient manufacturing have been paid great attention. AM, Finite Element Analysis (FEA) and Topology Optimization (TO) methods enable us to design and fabricate reliable, material wise efficient and low-cost products. With the combination of TO and AM, low density porous structures with superior mechanical properties can be manufactured by consuming less material within short time periods. In accordance with this motivation, naturally inspired cellular structures have been studied and systems having high strength-to-weight ratio are developed in literature [2]. For instance, regular lattice structures and honeycomb panels are used extensively due to their excellent mechanical behaviours [3]. Popularity of porous structures has been increasing lately due to the fact that their apparent attractiveness regarding mechanical performance outcomes solid counterparts produced by the conventional manufacturing techniques. Regarding the intricate porous structures, AM is becoming a better option for both designing and manufacturing of these artefacts compared to the traditional approaches [4].

It is clear that the interior structure of mechanical parts has great influence on the physical properties and the overall behavior of the model. That is why manufacturing software of AM and 3D printing devices offer several options considering the infill pattern of the parts to be fabricated. Among them, users select the optimum ones while keeping in mind that the greater volume fractions result in more resistant structures to the external loads while increasing the material consumption and the printing time [5]. Even if slicing algorithms propose regular infill patterns such as rectangular, triangular, wave, concentric, and honeycomb, users look for the specialized infill patterns other than the regular ones. This motivation enhances the number of studies related with irregular infill patterns. For instance, different than the traditional slicing algorithms, utilizing force flow lines can improve the load carrying capacities of tensile test specimens up to 50 % by constructing heterogeneous infill structures [6]. Integrating the irregular infill patterns into the capabilities of AM also brings the opportunity of getting additional benefits from the most commonly used artefacts. For example, the external shape of the systems can be kept persistent with the design requirements while the irregular infill porous pattern provides superior structural integrity and outstanding functionality [7,8]. Another perspective is that heterogeneous interior structure has the potential of eliminating some of the limitations of AM to reach effective manufacturing whilst it creates higher quality structures. Studies show that irregular infill patterns may overcome inborn constraints of AM, such as minimum feature size and supports needed for overhang angles. In addition to support free manufacturing, these patterns come up with improved mechanical stiffness and additionally bring static stability to the system [9,10]. By inspiration of Voronoi cells, aperiodic microstructures may alter the overall physical performance of the system, making it spatially graded, more flexible and stiffer in the intended regions of the part [11,12].

As it is stated, FEA and TO processes are perfect candidates for improving the strength-to-weight ratio of the designs. Combination of FEA and AM techniques intensifies the relation between manufacturing parameters and the structural

performance of the system whilst FEA predicts the mechanical performance of it before the fabrication. Furthermore, combination gives the opportunity to use less material since only the parts which get the improvement of the FEA are fabricated during the experimental validation stage [13]. TO methodology employed on AM processes are also efficient combinations since benefits include less material consumption which is followed by less printing time and improved structural performance [14].

As it is mentioned, regular and irregular infill patterns have extensive effect on mechanical properties of the model. Although manufacturing software of 3D printing devices offer several infill patterns to user to modify the interior of the parts to be produced, naturally inspired Voronoi cell patterns are not included. These structures are generally used as aesthetic purpose of art by architectures rather than structural components by engineers. However, Voronoi textures are seen in nature and nature itself uses them to form different creations. Following figure represents some of the Voronoi textures seen in nature.

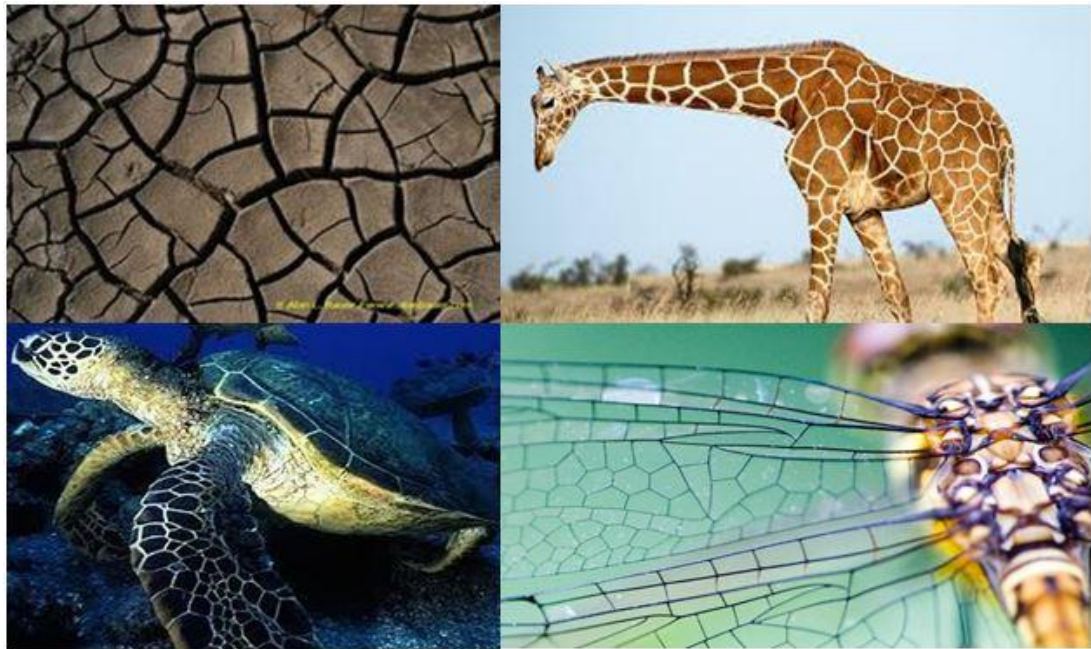


Figure 1.1. Voronoi patterns in nature; thirsty dirt (top left), skin of a giraffe (top right), flippers of a sea turtle (bottom left) and wings of a fly (bottom right).

Common definition of 2D Voronoi diagrams is that a set of points, called seeds, is specified beforehand and for each seed there will be a corresponding region consisting of all points closer to that seed than to any other. For 3D Voronoi diagrams, the term ‘region’ is replaced by the term ‘volume’ in the given definition. Figure 1.2 illustrates 2D and 3D Voronoi formations in a given geometry. In both 2D and 3D models, five Voronoi seeds are populated in the predefined closed region and volume, respectively.

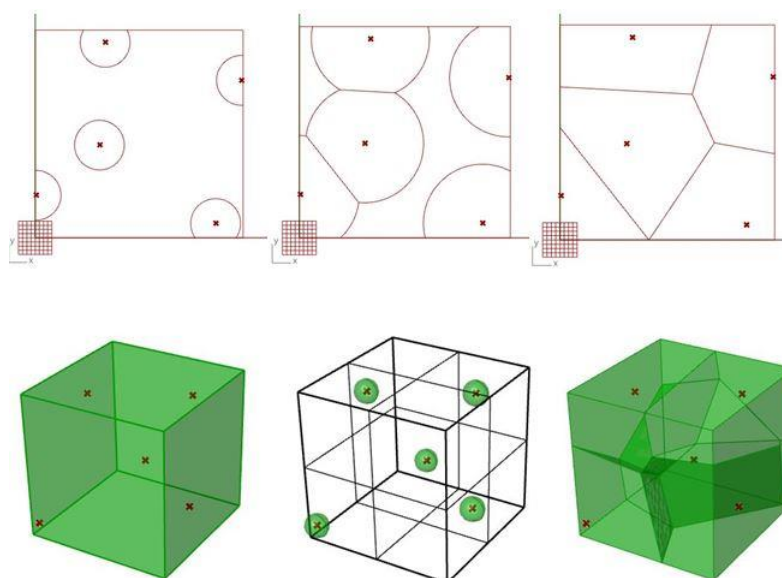


Figure 1.2_ Voronoi formations in 2D (top row) and in 3D (bottom row). Left column: five Voronoi seeds are initially generated. Middle column: Voronoi cells start to grow and intersect with each other. Right column: resultant Voronoi cells.

1.3. Motivation

General design approaches are related with and inspired by natural examples. Since evolution itself pushes beings to their full potentials in the most efficient way, it is important for us to understand, observe and mimic the nature itself. Even today, some of the most commonly used technological features are somehow inspired by nature itself and these features are specified as replicas of the natural examples. Also, core ideas behind these features are the simplest nature laws or natural keys of success. Although simplicity behind current technological developments is not simple, the most effective developments have the simplest ideas among the alternatives.

All living creatures, including human beings; are formed by numbers of cells which are the simplest ingredients of life itself. Science behind the actuality of these cells is rather complex. Since, this single building block of a being is shared among all existing creatures; this phenomenon is proved itself as a natural key of success. In addition, genetic code behind the mechanism allows the cell to form different structural body parts by simply populating itself. For instance, human body consists of approximately a hundred trillion cells that were generated by a single one after population. Additionally, the mentioned genetic code drives the populated cells to form our bones, nerves, internal organs and so on. This journey is shared among all livings in a similar way and continuously used by nature to maintain life.

The motivation of this thesis comes from within this journey. In this work, natural Voronoi cells are used as building blocks to mimic the formation of biological structural creations. These cells are used to construct naturally inspired optimized internal structures which meet the mechanical design requirements of the system.

1.4. Objective

The objective of this study is to imitate the formation of natural porous structures by using Voronoi cells and to generate an algorithm that tries to simulate the formation process from beginning to end. In this study, we propose three different methodologies that generate optimized Voronoi infill patterns within the predefined 2.5D and 3D CAD models according to the boundary conditions and the applied loads. Fixed number of Voronoi sites are distributed throughout the given geometry in the way of minimizing the maximum deflection of the artefacts under the predefined loading scenarios while lowering the overall weight of it. Our approach constructs mechanically efficient interior Voronoi pattern and compares the mechanical performance of it with the performance of the same artefacts which have randomly distributed Voronoi sites. In addition, these algorithms generate the optimized and the random artefact models which are directly exportable to the 3D printer software

without any manufacturing constraints. Lastly, methodologies are tested through experimentation and FEA.

1.5. Content

The thesis organized in five chapters. So far, some aspects of AM and porous structures are briefly discussed and they are correlated with this study. The relation between AM and printing porous structure is explained. The concept of this study is reviewed by narrowing the field of interest and hinted by viewing some of previous works found in literature. The definition of 2D and 3D Voronoi structures, formations and natural examples of them are illustrated and motivation behind this work is explained. The main objective of the thesis is clarified and it is associated with the motivation.

Following chapter is started with the literature review about Voronoi studies and their applications. The general Voronoi applications are illustrated to show the importance of this concept. Then, reviews narrow down the fields to specific structural Voronoi applications. It continues with the automated methodologies and algorithms to show their benefits in AM applications. It is highlighted that one of the novel contributions of this thesis is inspired by the trend of automation. Also, both regular and irregular porous infill patterns are investigated to reveal the outstanding possibilities of heterogeneity. Some of the novel solutions are connected with heterogeneity and traditional solutions are compared with them. Up to the last part of the literature review, it is intended to support the main aspects of this thesis by reviewing the related studies. The last part points out the new ideas and it is reviewed as a base knowledge for future works.

In Chapter 3, proposed methodology is tested on 2.5D parts. The evaluation of the algorithm is demonstrated by two different cases.

Chapter 4 takes one step further to advance the capabilities of the proposed approach. The methodology is numerically tested on 3D parts.

Chapter 5 states the overall conclusions and addresses the possible future works to improve the effectiveness of this thesis study in other applications.

CHAPTER 2

LITERATURE REVIEW

2.1. Introduction

In current chapter, the contribution of surveyed literature on the study is summarized. In order to remind that this work is composed of generating functionally graded porous medium by using hollow Voronoi cells, optimized Voronoi internal structures and comparison between these structures with other infill patterns such as regular lattice structures and random Voronoi infill patterns by using FEA and experiments are elaborated. Also, the work is done by an automated algorithm that assists user and user is always able to modify the mid-steps of the process to alter the output.

In accordance with the objective, following sections are organized as follow. Firstly, advances in Voronoi studies and Voronoi applications in literature are briefly mentioned. Secondly, some of the automated methodologies and algorithms which contribute significant advantages to 3D printing applications are presented. Thirdly, very similar to this work but not the same approaches are illustrated. These approaches mainly use porous medium that is formed by bringing together the concepts of variable density distribution, regular cellular structures and lattices. Then, the same concept is elaborated by using irregular cellular structures. Lastly, multi-material applications that are inspired by porous medium studies are presented.

2.2. Voronoi Studies and Applications

It is desired to comprehend the importance of Voronoi patterns and gain deep insights into Voronoi applications. Du et al. [15] worked on centroidal Voronoi tessellations (CVTs) to review the concepts and basic properties of them. It is illustrated that CVTs are used in geometric modelling, image and data analysis. It is also mentioned that the mathematical and computational concepts of CVTs are used to identify problems

encountered in applied sciences like physics, mathematics, biology and astrophysics. One of the most common meshing applications is Conforming centroidal Voronoi Delaunay triangulation (CfCVDT) for 2D numerical operations. Together with the use of density functions, CfCVDT gives better results than any other triangular mesh generations in the field of surface re-construction and optimization. Figure 2.1 shows CfCVDT meshes for different boundary regions and density fields.

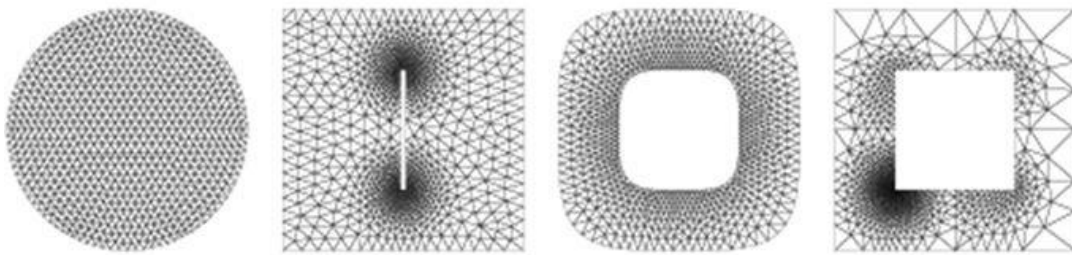


Figure 2.1. 2D CfCVDT mesh examples [15].

Another common application of CVTs is 3D spherical centroidal Voronoi tessellation (SCVT) that is used to construct finite volume pattern and vortex behavior on spherical geometries [15]. An interesting example of this application is modelling ocean and ice formations while reflecting the kinetic energy field in the North Atlantic.

Adaptive centroidal Voronoi Delaunay triangulation (ACVDT) is also regular application for modelling the mathematical problems. The anisotropic meshing methodology of ACVDT seems to be one step ahead of the competition that is between regular isotropic meshing and ACVDT and it is used extensively to generate high quality meshes in the form of triangles on various surfaces by Wang et al. [16]. Also, edge weighted CVT (EWCVT) is a very flexible and effective method for image segmentation. This method is capable of modelling very sophisticated states.

Faber et al. [17] have studies on image compression and territorial behavior of animals using Voronoi tessellation technique. Firstly, a colored picture formed by number of pixels is taken as input. The main objective is compressing memory size of a colored picture by reducing the color characteristics of each pixel and color range in the domain set of red, green and blue while keeping the number of pixels constant. The

same procedure is performed by using Monte Carlo algorithm and results are compared. Given 8-bit monochrome picture is compressed to 3-bit size accordingly by using two methodologies given above. Since, original picture has continuous color flow over the pixels, centroidal Voronoi algorithm suffers from contouring in nature. However, even this result is better in approximation compared to Monte Carlo algorithm. The mentioned contouring error of centroidal Voronoi algorithm is eliminated by dithering method. Another example that is related with the motivation of this work is about territorial behavior of animals that is very common among living creatures in nature. It is stated that in a control volume, if the number of animals of the same kind are settled synchronously, eventually all of them claim on their own space. An experiment of fish nature is an accurate example. Number of fishes was placed in a pool that has smooth uniform sandy bottom. Firstly, male ones start to excavate the sand to build a place for breeding. Each one acts exactly in this manner and this act results in territorial boundaries that are approximated by a Voronoi pattern, seen in Figure 2.2.

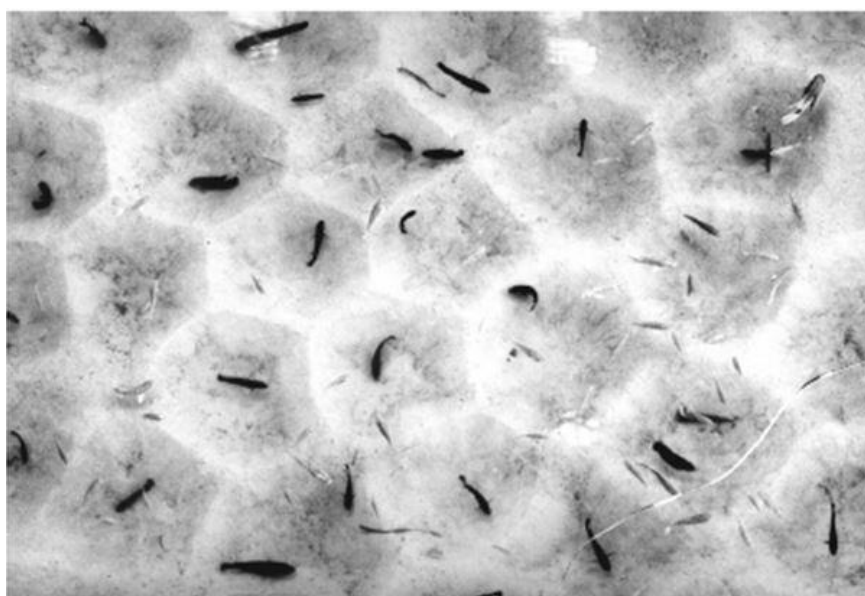


Figure 2.2. Territorial behavior of fish and resultant Voronoi pattern [17].

Similar to image processing part of the previous study, Brackett et al. [18] used error diffusion method to convert continuous color tone image into binary form by using

2D Voronoi tessellation and compare the resultant cellular structure with the Delaunay triangulation scheme. The comparison is related with the resolution that directly depends on cell size. The resulting sizing evaluation indicates that, Voronoi connection scheme has slightly lower mean cell size, which is favorable.

Differently, Kou et al. [19] offer an approach that uses Voronoi diagrams together with the B-spline representation in functionally graded microstructures in 2D. Integration of B-spline representation to Voronoi tessellation results in naturally inspired complex patterns which are also collective and customizable. The porosity level in specific regions of interest is controlled by merging operations while direction dependent scale factors effects the graded pore sizes. In other words, topologies of functionally graded cells are adjustable horizontally or vertically just like the positions of cells. Furthermore, an example model is functionally graded by applying topology modifications. The left side of the porous example model is fixed and right side is subjected to the distributed load. This FEA model is than compared with a new model that is geometrically the same and has the same loading/supporting conditions. The only difference between them is the second model regards the voids as another constituent material. In other words, the void material is replaced with another material in the second model. As a result, FGM model is compared with two phase FGM model. FEA results show that FGM is stiffer and able to resist more deformations while two phase FGM is mechanically weaker.

The same approach is employed on a porous media to investigate the laminar flow characteristics of water by Tan et al. [4]. The porous model is generated by proposed constructive method and analyzed by using Navier-Stokes analysis. The fluid flow velocity field is proved to be consistent with other related studies in literature. Also, the constructed model is applied on 3D models to show the simple 3D porous solids.

Gostick [20] has studied the effect of Voronoi tessellation on PEMFC gas diffusion media. Opposite to common PEMFC gas diffusion models based on repetitive cubic lattices, 3D stochastic Voronoi diagram is used to construct fibrous media model.

Mercury, water and gas diffusivities are modeled and effect of Voronoi pore network size on phase diffusions is observed. Overall, it is concluded that proposed model has great potential for multi-phase flow analysis.

Fantini et al. [7] studied with 3D Voronoi tessellation to construct naturally inspired porous 3D bone tissue model that has controllable porosity level and pore size. The main objective is creating 3D bone implant by taking bounding box of the controlled volume which is damaged bone part. Then Voronoi cells are automatically created in this volume where porosity and pore size are the controlled parameters. The modelling stage is illustrated in Figure 2.3.

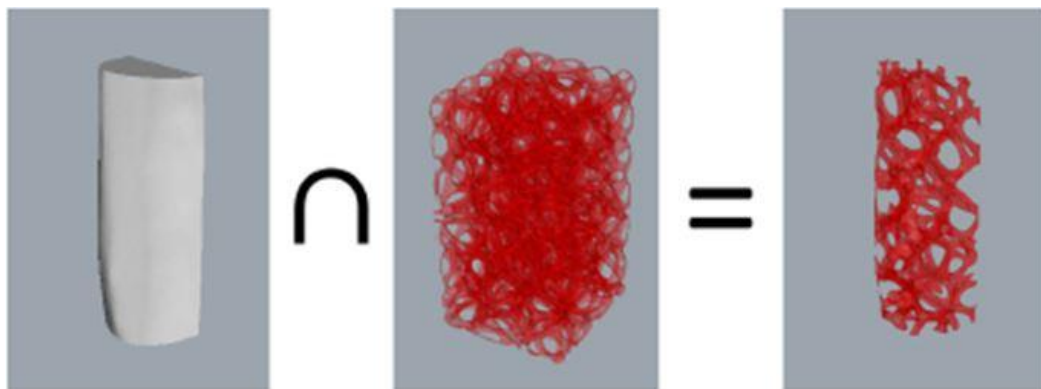


Figure 2.3. 3D Voronoi bone tissue model [7].

In order to control pore size and porosity level of the model, some sample scaffolds are modeled to measure the effect of seed number and pore size on porosity level. It is observed that as the number of seeds increases, the target pore size decreases. It is assumed that the ratio between volume of the model and the bounding box determines the number of seeds in the model. Therefore, it is concluded that number of pores can be found since pores depend on seeds and seed number is the initial input. Another important parameter that serves the objective of the study is the pore connectivity with surrounding pores since cell growth and population in scaffold are affected by the connectivity. It is proven that mean number of faces of Voronoi cells give the information about interconnectivity and the mean area of faces of Voronoi cells give the mean size of the connective channels. The work is applicable for bio-models since

the actual bone shape is represented with realistic details and the generation speed of bio-mimic porous inner structure is quite fast. By simply setting porosity and pore size requirements, an accurate naturally inspire model is constructed.

2.3. Automated Methodologies and Algorithms in AM

It is known that even the simplest desktop 3D printers have default algorithms that increase the overall efficiency of the manufacturing process. These algorithms include the manner of pre-defined infill patterns, process planning, material amount that will be sufficient for printing, support locations and material amount for them. Not only the layer by layer manufacturing nature of 3D printing but also these user assistive algorithms make the whole process practical for us. One of the novel contributions of this thesis is that proposed algorithm gives directly printable models by taking simple inputs. Similar to this sense, following studies propose automated methodologies and algorithms to user to fulfill the desired requirements.

Ma et al. [21] proposed an algorithm that gives the solution for soft pneumatic models with preferred deformations. Two phase algorithm is developed to construct interior frame structures of model and to compute geometric draft output. The 3D model of object at its rest pose and deformed mark models are given as input to the proposed algorithm. As it is stated, the algorithm generates pneumatically deformable chambers inside the 3D geometry. The pneumatic input is given by using pressurized air. The algorithm optimizes the material properties, chamber locations and structures so that printed artefact can deform to given deformed mark models. The proposed algorithm is tested on various 3D models to prove the efficacy of the work. Following Figure 2.4 illustrates the process chain for cylinder model.



Figure 2.4. Deformed cylinder models from left to right; deformed models, stationary printed artefacts, pneumatically deformed artefacts and differences between input poses and deformed artefacts [21].

Similar to prior study, Skouras et al. [22] offer an automated method to create deformable models that are digital replicas of well-known characters. Again, 3D model of the character at its rest pose and deformed mark models are given as input to the proposed algorithm. The algorithm has three main stages. Firstly, the proposed algorithm calculates the number of actuators among string, pin or clamp types and determines the placement region or attachment point on surface of the model. Secondly, positions of the actuators are adjusted in such a way that distance of the model to the desired target pose is minimized. Lastly, infill material distribution is defined. Three phase algorithm combines the use of FEA, constrained optimization and sparse regularization. Automatic methodology is tested on 2D and 3D models and physical replica of Palmy2D model and its deformed poses illustrated.

Prevost et al. [23] propose a user interactive automatic algorithm that prints the 3D characters in user defined poses. The proposed algorithm edits the input 3D model to get perfect balance position while interactively communicating with the user towards the printing stage. Firstly, user defines the mode of the end product among two possibilities, suspension and standing modes. Suspension mode creates a model that

can be suspended by a string from any location that user choses on the surface. Standing mode on the other hand, creates feasible standing position and it is related with center of gravity of the model. Then algorithm manipulates the model by carving inside of it or deforming the outer shape by using energy minimization algorithms or stability optimization methodology. End models sustain the surface details. A set of artefacts with different poses were printed for this study. Following ones are particularly important and demonstrated since the precision of center of gravity formulation in algorithm is remarkable. Example artefacts of horse and T-Rex are given in Figure 2.5.



Figure 2.5. Left, horse model that is able to stand alone by the help of tail touch together with two feet and printed artefact that is able to stand alone on its single feet. Right, big head T-Rex is able to stand alone due to precise center of gravity adjustment [23].

Another way of manufacturing the 3D artefacts is suggested by Malomo et al. [24]. In this study reusable flexible molds are automatically designed for various types of geometrically and topologically complex 3D models. These printed models are used for liquid casting manufacturing to copy multiple complex geometries having extensive surface details. Algorithm simulates the motion planning of low viscous resin during casting and places a bigger hole for pouring the resin and smaller holes for appropriate air escape. Greedy bottom up optimization is used to find the best polyline that is suitable for cutting layouts of the model. Also, dynamic simulation is added into algorithm to realize forces generated by extraction movement during removing or detaching and strain estimation is considered. This approach is also tested on number of nontrivial and complex 3D topologies and one of geometrically difficult case is shown in Figure 2.6.

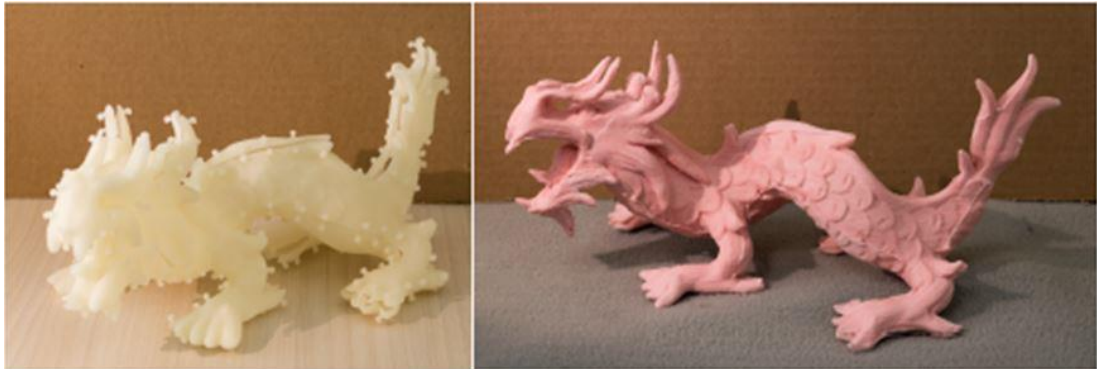


Figure 2.6. Complex 3D mold of dragon and casted artefact [24].

Christiansen et al. [25] presented a novel method for automatic 3D modelling based on topology optimization together with the shape optimization. The algorithm accepts the given 3D model input as triangle mesh representation and gives the optimized final model in the same format. In addition, compared to common fix grid methodologies, the proposed method offers high resolution designs in reasonable time. Also, mechanical requirements and shape constraints can be defined at the beginning. The work is applied on different 3D models and scenarios and results show that the given method satisfies both design requirements in the manner of improved structural stiffness and self-balance and functional requirements. As an example, three chair and table models are generated. The initial constraints are fixed layer at the top of the table, distributed load on it, fixed seating layer and back support layer on the chair and again distributed load on the seating layer. Table and chair support locations are distributed differently at the bottom.

Another automatic approach is proposed by Sa et al. [2]. The proposed automatic approach generates adaptive voids to solve given problem in a specified boundary volume in order to reduce the required infill material for printing. Similar to other studies, algorithm takes the input as mesh. Then, it tessellates the boundary volume by populating both primal and dual 3D cellular structures in open or closed forms. Last step is completing the borders of the cells by using struts. User defines only the

boundary volume and the diameter of the struts which directly affects the density field of the model and total weight of it. Although intended purpose includes establishment of maximum strength while keeping the required material amount minimum, no work done to inspect mechanical behavior of modeled structures. However, proposed infill pattern is compared in the manner of printing time by using two common infill patterns namely; linear and hexagonal. Stanford bunny is chosen as an example model that weights 84 g with primal and dual cellular structures and printing time is 7 h. The bunny with hexagonal infill pattern took 3.5 h and the linear one took 11 h.

Wang et al. [26] have studied on an automated algorithm that designs skin frame 3D structures with struts for the desire of reducing material amount for printing. In addition, output model is guaranteed to be physically stable and printable. Multi-objective formulation of the algorithm uses both size optimization and topology optimization methodologies to build stiffer, self-balanced and low material models. Specific models are generated by using naïve hollowing method and proposed one. They are loaded externally and FEA result of deformation map on the models shows that deflection displacements of vertices have lowered. Additionally, various models are modified by the algorithm to reduce the material amount in the range of 70-90 % in comparison with the solid counter models.

To improve service life of the printed artefacts, Stava et al. [8] propose an automated algorithm that works on 3D models. Algorithm predicts possible problems that may cause fail of the artefact during the service live and corrects these challenging cases. First stage of the algorithm determines the loads and classifies them into permanent load category or imposed load category. Permanent loads represent the gravity force due to weight of the artefact and imposed loads represent both gravity and the grip forces caused by two fingers during holding the artefact. Then FEA, printability modifications, medial geometry analysis, local thickening, strut adding, strut thickness correction, hollowing and shape optimization methodologies performed simultaneously. The mentioned detection stage and correction methods are repeated

until the case is closed. Eventually, light weight artefacts perform great structural integrity during their service lives.

Al et al. [6] offer an automated method that increases the tensile load carrying capacity of 2.5D parts up to 50 %. The algorithm is composed of FEA and heterogeneous infill generator. FEA defines the Von Mises stress field on the part under predefined tensile loading and resultant field is transformed to boundary regions to generate infill pattern by using colored mesh operations. The mentioned stress field and modified infill pattern after transformation is shown in Figure 2.7.



Figure 2.7. Stress field of the model (left) and generated infill pattern (right) [6].

The printing material is deployed in accordance with infill structure of modified model. In order to validate the approach, tensile test specimens are printed by FFF type 3D printer. Additionally, two more tensile test specimens are printed by using linear and diagonal infill patterns. All test specimens have infill percentage of 58. Experiments concluded that proposed approach increases the load carrying capacities of 2.5D parts up to 50 % and load to weight ratio of modified part up to 70 % in comparison with regular infill patterns.

Zhao et al. [27] studied on a new kind of infill strategy that is applicable on 2D and 2.5D parts. Proposed automatic algorithm creates continuous Fermat spiral curves which are long and low curved curves in comparison with common infill paths in a given closed 2D region. The algorithm decomposes the input closed region into sub-regions and each of them is filled with mentioned continuous curves by applying curve optimization, rerouting and path generation to that sub-region. Also, it is proven that start and end point of a Fermat spiral curve can be located at the same point which is outside of the subject sub-region. Thus, each subsection can be merged to obtain single Fermat spiral curve that is filled the input boundary region. In comparison with the

conventional filing pattern applications, proposed method leads to effective fabrication. A complex kitten example is filled with a single long Fermat spiral to show the effectiveness of the algorithm.

The last automated methodology is studied by Garcia-Dominguez et al. [28]. In this study, both the infill structure and the external shape of a model are topologically optimized simultaneously. The algorithm allows using single or multi objective topology optimization in a single process. The main objective of the study is about constructing a continuous work flow without affecting the flexibility of the design. So, the problem case is divided into several sub-problems and multi objective topology optimization deals with the cases. The continuous work flow is constructed in Rhinoceros by using grasshopper, Karamba3D and Octopus plug-ins.

2.4. Porous Regular Infills

In engineering applications, nonhomogeneous porous structures are commonly used due to their excellent mechanical properties. Additionally, expansion of usage and efficiency of these structures have furthered by the appearance of AM techniques. To construct the internal structure of a model, micro and macro level repetitive lattice structures are proposed and they are used in functionally graded manner. In this section, functionally graded porous infill patterns which are constructed by the use of repetitive cells are studied. Outcomes are discussed and beneficial methodologies are highlighted.

Provaggi et al. [13] combine the concepts of AM and FEA to predict the overall performance of a lumbar fusion cage design before actually printing the part. Manufacturing parameters like material in use, infill pattern and density are evaluated in terms of the effects on mechanical performance of a lumbar cage. Three different materials (PC, ABS and PLA) are selected to develop the model. In order to feed the FEA part with realistic values, each material mechanically tested by standard mechanical applications and compressive modulus and yield strength findings are noted. Then, rectangular and honeycomb infill patterns with varying infill densities

are embedded into FEA models. It is noted that infill density and pattern have significant effect on mechanical behavior of lumbar fusion cage model under static loading. FEA results conclude that PC and ABS can be used for modelling a lumbar cage with 50 % infill honeycomb inner structure.

Another AM oriented optimized porous interior structure is proposed by Zhao et al. [9]. In this work, it is proposed that a novel method uses adaptive voids and TO with multi-interval density filters to fulfil the objective of SF manufacturing while satisfying the constraint about minimum feature size. The proposed method is applied to the cantilever beam problem given in Figure 2.8. In order to validate the performance of the proposed method, the homogenization, optimization and construction (HOC method) is applied on same cantilever beam. 2.5D beam models of proposed and HOC method are printed in same direction with the base plate. Printed artefacts are also shown in Figure 2.8.

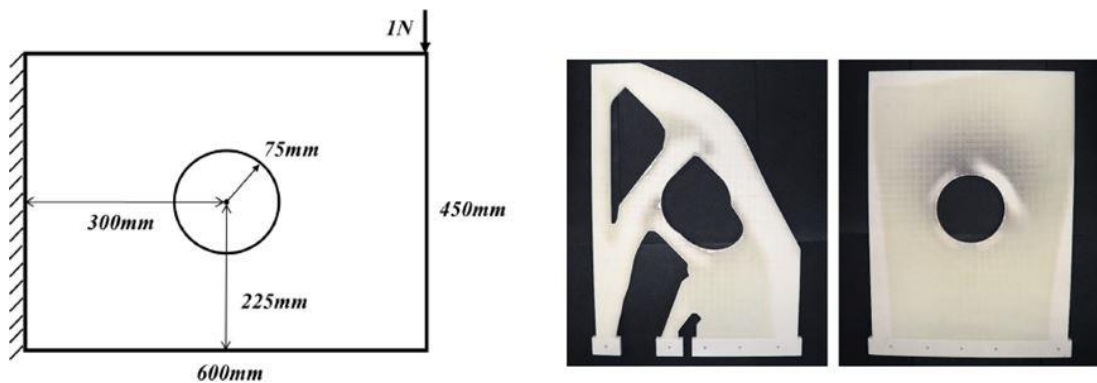


Figure 2.8. A cantilever beam problem with boundary and load conditions (left), printed beam models by proposed and HOC method (right) [9].

The beam model of proposed method (left) is printed without support structures while HOC model needs those structures around the central hole. Both numerical and experimental results show that exceptional mechanical stiffness is achieved via proposed method and it validates adaptability to AM constraints.

In order to compare the stiffness of porous open cellular aluminum foams with Ti-6Al-4V foams, Murr et al. [29] modeled these structures by the help of CT scan of

open aluminum foams and embedded them into CAD environment. Two different cellular foam structures are printed by the use of EBM technology, hollow and solid cell structures. Then, resonant frequency damping analysis is used to measure Young's modulus of the models. It is proved that stiffness varies inversely with the level of porosity in both solid and hollow models. Also, it is shown that micro indentation hardness of hollow cell foams is 40 % higher than the fully dense solid counterparts. To conclude, complex thin walled of hollow Ti-6Al-4V cellular structures exhibits higher micro indentation hardness and strength and can be fabricated by EBM technology.

Panetta et al. [30] use repetitive tileable cubic patterns to construct isotropic and anisotropic printable models intentionally. Elastic porous internal structure is composed of parametric cubic tileable elements and Poisson's ratio of it can vary between 0.5 to negative values. Truss like symmetric 3D patterns are grouped by connective shape optimization searches and this group is used to construct isotropic and anisotropic patterns with desired isotropic and orthotropic mechanical response. Also, material optimization algorithm assists user to fit the object into desired deformation under specified loading conditions. Several examples are printed to show the flexibility of the proposed methodology. It is demonstrated that proposed elastic textures handle to accomplish given graded material distribution to approximate varying isotropic properties of a model. It is shown that repetitive cubic elements are tileable and can be printed by a single nozzle 3D printer without need of support structures.

In order to use the contributions of TO, FEA and functionally graded cellular structures together with the capabilities of AM, Li et al. [31] propose a novel optimization approach that generates adaptable density gyroid interior structures and performs graded structural optimization. The penalty function is added to optimize the connectivity and continuity of the gyroid structures and homogenization methodology is used to obtain mechanical properties of them as a function of relative density. Scaling law computes the ideal density distribution within the part and interpolation

of density mapping enables to distribute gyroid structures across the design volume with a uniformly varying density. The efficiency of proposed method is strengthened by numerical and experimental procedures. Figure 2.9 shows the arm model of a quadcopter. Having the same volume fraction with the truss model, the FEA results state that proposed method has 45 % improved stiffness which is also supported by experiment that results in 44 % improvement.

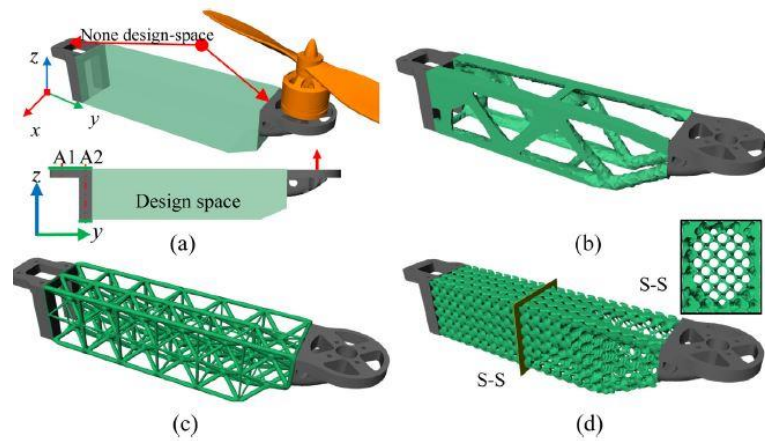


Figure 2.9. Modeled arm model of the quadcopter: (a) Initial model, (b) result of regular TO, (c) truss like design, (d) proposed optimization [31].

An alternative use of repetitive lattice structures is proposed by Pham et al. [32]. In this study, under specific loading conditions, slip behavior of metallic crystal structures are liken to rapid decrease in mechanical strength of repetitive 3D printed lattice structures. Due to identical orientation of lattices, sudden failure of lattice structures is commonly seen beyond the yield point of the base material. It is proposed that texture of crystalline interiors like grain boundaries are mimicked by utilizing the unit lattices to reflect strain hardening mechanism. The relation between lattice orientation and deformation characteristics of designed models is investigated. For this purpose, grain structures are scaled into macro level and single grain structure is compared with eight-grain structure in which shear strain localizations are controlled by altering the orientations of eight meta-grains. It is seen that adaptive boundaries between eight grains increases the overall toughness of the model while ending efficiently the crack propagations between brittle printed lattices. To illustrate the

effect of consumed material on crystal like structures, elastoplastic polymer, stainless steel and brittle resin are used to construct the same artefacts having eight meta-grains. Both the elastoplastic polymer and stainless-steel lattices prevent brittle cracks while resin lattices suffer from it. This gives the idea that toughness behavior of material in use has significant effect on lattice behaviors. On the other hand, similar localized strain which is seen in both polymer and steel lattice expresses that crystal inspired oriented lattices is applicable to different type of 3D printing materials.

A useful study that integrates TO into AM by using repetitive cellular structures is proposed by Cheng et al. [33]. In this study, TO which is based of homogenization of variable density regular cellular structure distribution is embedded within the methodology to obtain lightweight design and improved stiffness behavior. As a first step, homogenization is combined with scaling law to detect relative densities and important mechanical properties of cellular structures. Accordingly with density field, regular repetitive lattice structures are constructed within the model in use. To guarantee the manufacturability of optimized models, optimum density field within the structure is altered for constraints of AM. The proposed methodology is tested experimentally and compared with the structures having uniform density field composed of repetitive regular lattice structures. The printed artefacts accordingly with mentioned interiors and experimental results are shown in Figure 2.10.

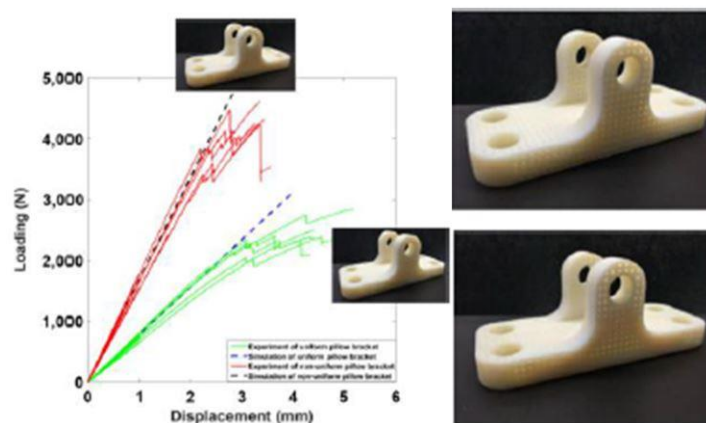


Figure 2.10. Experimental results of uniform and non-uniform density brackets and printed artefacts [33].

Common analytical FE models simplify the complex problem to predict the resultant mechanical behavior. The exclusion of micro structure and matrix material properties in analytical models' results failure in prediction of mechanical behavior of the structure. The following method proposed by Campoli et al. [34] construct a FE model that includes the effects of irregularities resulted by manufacturing nature statistically. In this study, selective laser melting of titanium manufacturing technique is considered and porous models are investigated. The results of proposed FE model and analytical models state that, for slender struts, the predicted mechanical behavior is similar. On the other hand, for the thicker ones, shear and torsion behavior of a strut is not included in regular analytical models due to simple beam model approach. Opposed to common methodologies, proposed approach uses Timoshenko beam model that includes shear characteristics of a strut and results realistic predictions for thicker struts. Thus, guesses of proposed FE model are much closer to experimental data.

Another novel method to design porous cellular structure for efficiency is studied by Han et al. [35]. Compared to other methodologies in literature, this approach considers the functionality and the manufacturability of artefacts for both heat transfer ability and load carrying capacity. Repetitive unit cells with constant wall thicknesses are produced in the manner of variable size in accordance with the TO outcome. Smaller cells are used for high density regions due to high volume fraction and also used for better heat dissipation since their surface to volume ratios are also high. To validate the proposal, two different models are analyzed. Firstly, the SIMP method is applied on cantilever beam design by setting penalization factor as three. The problem demonstration is given in Figure 2.11. Iteration of size gradient of cellular structures results in optimized interior. To validate the method, FEA and tensile test experiment are conducted. Both results states that optimized interior structure has smaller compliance even if it has same volume fraction with the regular one. Size gradient iteration and printed artefacts are also shown in Figure 2.11.

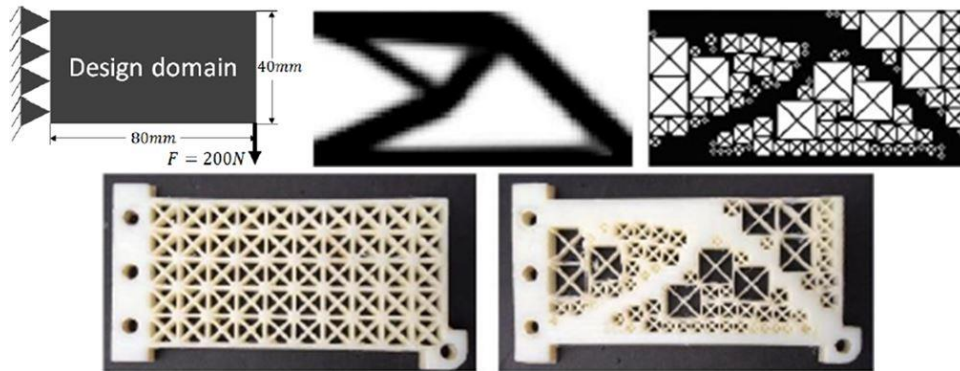


Figure 2.11. Cantilever beam design: geometry and conditions (top left), TO result and cell distribution (top right), printed artefacts (bottom) [35].

Secondly, traditionally grooved, uniform interior and optimized interior models of a heat sink are compared to show the heat dissipation differences of the models. Analyzes are conducted in ABAQUS and the same volume fraction is defined for three geometries. ABAQUS results show that optimized interior absolutely has greater heat dissipation capacity even if it has the same boundary coolant area with the uniform model.

Adaptive Rhombic cells are used by Wu et al. [10] as interior infill pattern to strengthen the 3D parts and to make them self-balanced. The method is composed of infill optimization, FEA, sensitivity analysis and design update. Rhombic cells and their shell thickness are adaptively calibrated to avoid manufacturing constraints of AM such as overhang angle and use of interior support structures. The efficiency of the methodology is demonstrated on various examples to validate the improvements on mechanical stiffness and static stability. Furthermore, following example demonstrates the efficiency of proposed method on mechanical stiffness of structures. The given model, in Figure 2.12, is considered as three-point bending beam that is supported by two ends and loaded from middle. Two different infill patterns are applied to reveal that optimized interior generated by proposed method is mechanically much stiffer in comparison with uniform interior, even if the material (PLA) amount for manufacturing is same for both. In the second row, the behaviors of equally loaded beam models are shown. The optimized version has a displacement

of one half of the displacement on the uniform version. Also in the second column, the load capacities of equally displaced beam models are shown. Results state that the load carrying capacity of optimized beam is increased 55 %. Physical results conclude that proposed method is applicable.

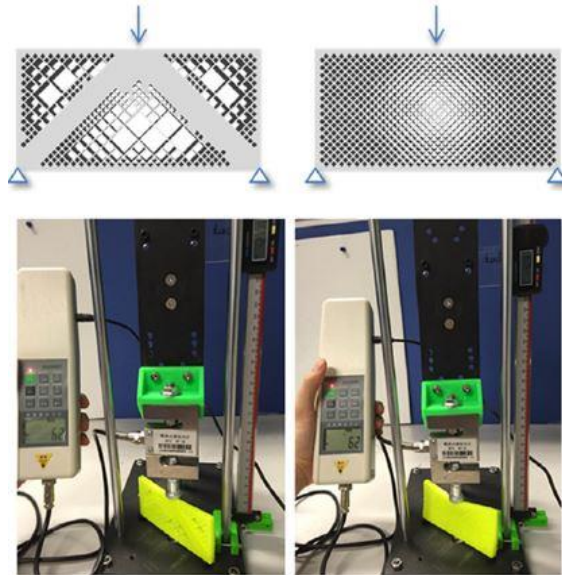


Figure 2.12. Three-point bending beam models with different infills (top) and experimental validation (bottom) [10].

Al-Saedi et al. [36] have studied effects of functionally graded microstructures on energy absorption capacity and mechanical properties. They constructed F2BCC lattice structure by using one FCC and 2 BCCs together. Al-12Si aluminum alloy powders are carried by SLM technology to form functionally graded structure and uniform structure. These printed artefacts undergo microscopic inspection to reveal diameters of solid struts and surface quality. It is seen from the images that SLM technology is applicable to produce functionally graded F2BCC lattice structures by using Al-12Si. Surface analysis reveal that step-stair effect increases the struts diameters in comparison with the CAD model. Also, FEA modelling and compressive experiments are conducted to observe and compare the deformation behaviors of both functionally graded and uniform lattice structures. The FEA and experimental results of functionally graded structure reveal the similar compressive behavior under loading

conditions. The failure begins in the low-density layer and continues to higher density regions layer by layer. On the other hand, deformation characteristics of uniform lattice structure alters in FEA simulation and compression experiment. This is reasoned by 45-degree shear phenomenon and fracture. It is concluded that functionally graded lattice structure is able to absorb higher energy in compression than the uniform one. Furthermore, the data obtained is applicable with Gibson and Ashby analytical model and can be used to approximate the mechanical assets of other SLM printed functionally graded lattice structures.

Rather than micro lattice structures, Feng et al. [37] focused on macro lattice structures in their study. It is proposed that internal topology is optimized by the use of Hourglass truss lattice structures. The compressive behavior of Hourglass structures is compared with the behavior of regular pyramidal lattice structures under same loading conditions both numerically and experimentally. The proposed new lattice geometry exhibits superior resistance to buckling. In comparison with the pyramidal geometry the truss structures of hourglass have reduced slenderness ratio even if their relative densities are equal. Furthermore, with constant truss thickness, distance between nodes in single layer Hourglass structure is twice of the distance between nodes in single layer regular pyramidal structure. Since theoretical compressive model is more accurate than the theoretical tensile model, pyramidal and Hourglass sandwich structures are exposed to compression study. Predictions of analytical model are in agreement with the experimental results. Experimental results indicate that the same structural dimensions, compressive load carrying capacity of the proposed model is 3.5 times higher than the load carrying capacity of regular pyramidal sandwich lattices. The proposed Hourglass lattice structures are considered as favorable alternative interior structures for lightweight and high-stiffness designs

Ullah et al. [38] proposed another superior class of three-dimensional truss lattice structures that are composed of Ti-6Al-4V and can be directly manufacturable by SLM technology. So called Kagome truss lattice is inspired by internal structure of cancellous bone. It is previously proven that Kagome truss structures exhibits better

than standard aluminum foams and tetragonal lattices in compression strength and capacity of energy absorption. These bio-inspired Ti-6Al-4V cores can be manufactured by SLM technology for diameter of truss larger than 0.6 mm and internal angles of less than 60 degree without needing internal support structures. FEA results predict the mechanical performance of the Kagome structures and experiments validate that these titanium structures are applicable in aerospace applications, can be used instead of aluminum honeycombs which have equal stiffness response while having less shear and compression strength.

Amendola et al. [39] studied different truss-like structures called tensegrity structures which are axially loaded and prestressed structures. During manufacturing operations, EBM technology is employed on Ti-6Al-4V powders to create tensegrity prisms attached to flat triangular bases. After this phase, short-term supports are removed and Spectra cross strings are manually added to these structures to generate proper internal pre-stresses. Also, these unit structures are added to top of each other to construct tensegrity columns, which are also axially loaded to inspect the stiffening mechanical response of elastic behavior. It is observed that non-linear mechanical response and elastic hardening phenomena are the results of relatively large axial displacement. These results are in agreement with the previous studies in the literature.

2.5. Porous Irregular Infills

Similar to the previous section, in this part, functionally graded infill patterns are investigated. Rather than use of repetitive regular structures, non-linear irregular infill patterns are in the scope of the main objective. Although repetitive patterns have proved their excellent mechanical behaviors over past decades and extensively used in engineering applications, the recent common trend is about use of irregular infill patterns. One of the freshest applications is processed by FormLabs in cooperation with New Balance [40]. It is stated that traditional manufacturing cannot catch up the modern consumer demands on custom products that can be easily manufactured within short time periods. With this motivation, New Balance cares the potential of

AM and moves the technological background from prototyping into custom made products and also makes investments into material science that is applicable with AM. Resultant SLA material, Rebound resin, is used by FormLabs and New Balance to design new footwear that is constructed by springy, resilient lattice structures that is capable of higher energy return, tear strength and elongation characteristics. Thus, it is validated that AM is able to lead the future of performance products with customized manufacturing. The irregular lattice structure formation in mentioned performance shoes is shown in Figure 2.13.



Figure 2.13. Irregular lattice formation of the structure of New Balance base [40].

Moving back to literature survey, Ying et al. [41] studied anisotropic behaviors of 2.5D porous structures by using interior Voronoi tessellation. In this study, physical directional properties of stress and elastic fields within the structure are adapted into non-uniform porous structure modelling via using results of FEA. The proposed methodology is tested on various input 2D shapes and compared with isotropic tessellation of Voronoi structures by FEA. For each input, boundary and loading conditions are defined, isotropic and proposed anisotropic interior infills are generated and porosity levels are recorded. To validate the FEA results and the efficiency of the proposed methodology, two forms of bridge example are printed by PLA material with the same porosity levels and tested experimentally. The results of compression experiment verify the FEA and it is concluded that anisotropic Voronoi distribution

within the structure outperforms regarding to the strength to weight ratio. Printed models and load displacement curves are shown in Figure 2.14.

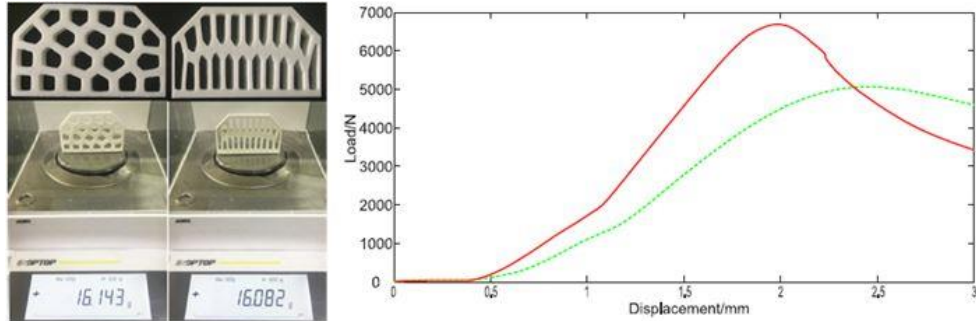


Figure 2.14. Printed artefacts with isotropic (green curve) and anisotropic (red curve) Voronoi infills (left) and load-displacement curves (right) [41].

Open Voronoi foams are used to investigate procedural arbitrary microstructures by Martinez et al. [11]. The geometry of microscale structure has direct effect on macro-scale mechanical response of the object. In accordance with the idea, the open Voronoi foam microstructures are generated within the surface of the object to modify the elastic behavior of it. As opposed to overall optimization process, implicit estimation that is very similar to procedural textures used in computer graphics is used for adaptation of the desired elastic field onto model. Thus, very detailed surfaces and internal structures are generated in big models without representing the whole meshes of the model. The key advantage of this method is significantly reducing the slicing time. The related information is added on the fly beforehand the printing of the slice. In conclusion, geometric properties of each open foam Voronoi microstructure are evaluated to form desired elasticity field while minimizing the slicing time. The proposed model is applied on several artefacts with functionally graded elasticity. One of the elastic complex models is shown in Figure 2.15. The average slicing time is recorded as 28 seconds for the given example.



Figure 2.15. Complex model of elastically deformable finger [11].

Kandemir et al. [14] studied effects of penalization factor of SIMP topology optimization method on the mechanical performance of the topologically optimized variable density 2.5D printed artefacts. For this purpose, penalization factor is set to one to obtain resultant density field within the model without discarding the low-density regions of the model. The thickness value, in the out of plane direction, is assigned to each finite element proportional with the density values. Thus, conformal surface of the model is constructed by utilizing the thickness values to each node. To evaluate the performance of the method, objects are printed by using ABS and ONYX materials and compared with the counterparts that are designed by using traditional SIMP methodology having penalization factor three in terms of FEA and experiments. Experimental results revealed that load-to-weight ratios of the artefacts generated by proposed approach are nearly five times higher than the artefacts produced by classical SIMP having penalization factor three.

In order to represent the density of a porous model with heterogeneous interior, Schroeder et al. [42] offer a new method that represents the porosity level and heterogeneous interior structure of bio-materials. An example of UC Berkeley one is chosen to validate the approach experimentally. Starting from the beginning, the actual porous bone model is taken, in the form of VRML, which is represented by triangular

meshes. The second stage of the method is voxelization that converts the format of the model from triangular meshes to set of voxels. Then proposed method calculates the voxel distributions. After that voxel distributions are reconstructed by processes like union, intersection and inversion. Then material definitions are attained to each voxel randomly to meet the desired density level. Simulated annealing process is applied on the reconstructed model to fit the density with the real one.

Another contribution is done by Rainer et al. [43] on computer aided tissue engineering (CATE). The study proposes a method to design mechanically optimized scaffolds structures based on FEA of the loadings at the implant region. The proposed algorithm supports free form fabrication process. To demonstrate the validity of the proposed method on bio-mimetic structures, a femur bone model is processed. The head portion of the femur model is assumed to be loaded in the direction of shaft axis of the femur. Under defined loading conditions, stress tensor and principal stress directions are calculated for the entire model. A small portion of the interior part of the head is chosen to be manufactured and visualize as a small scaffold. The directions of two principal stresses are projected on coronal plane of the scaffold and deposition trajectory follows these projections while printing it. The projected trajectories and printed PCL scaffold are represented in Figure 2.16.

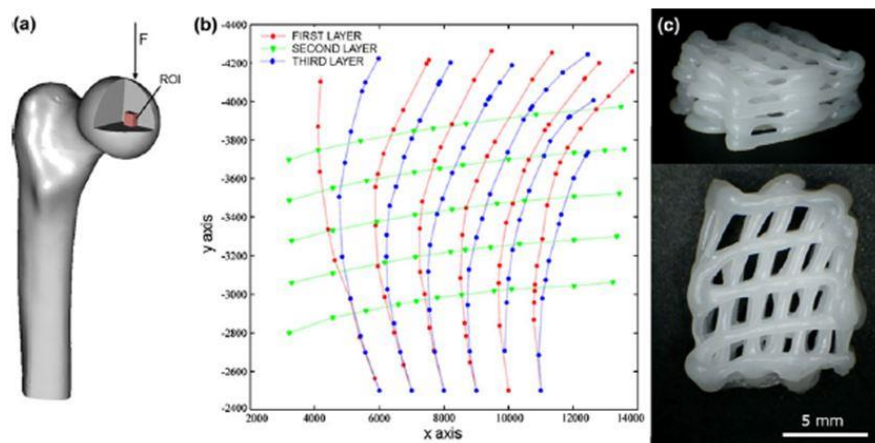


Figure 2.16. (a) Implant region and loading conditions, (b) projection of principal stresses for layer development, (c) printed artefact [44].

To reduce the large memory consumption of complex models while contributing orthotropic elastic properties, Song et al. [44] propose a novel method that procedurally generates stochastic orthotropic foams. The physical properties like density, angle and stretch are mapped behind the parameters of procedural generation of foams. Thus, local frame orientation and Young's modulus along orthogonal directions are freely variable in the design volume and total memory consumption is lowered. The resultant foam structures are analyzed and validated both numerically and experimentally.

Martinez et al. [12] introduce a Voronoi inspired stochastic microstructures that add desired orthotropic elastic behavior to the system and overcome the main aspects of FFF technology such as continuity requirement, overhang angle constraint and SF. The proposed method parametrizes the distance between cones and correlates the geometric properties of Voronoi cells with elastic behaviors of the system. They tested a variety of orthotropic elastic behaviors of printed artefacts. The pipe design transfers applied loads between the inner and outer pipe layers to protect the inner or outer shape of the pipes in different applications. In addition, they modify the density, angle and anisotropy within the shoe sole model to alter the bending characteristics and softness of it. Examples are presented in Figure 2.17.

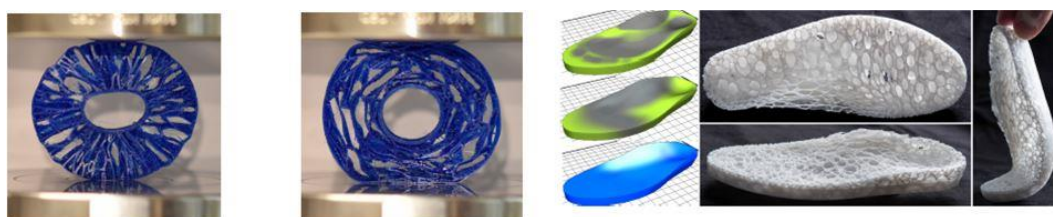


Figure 2.17. Left, orthotropic pipe model that protects the geometry of the inner pipe under same loading condition. Right, printed shoe base according to strength, bending stiffness and density considerations [12].

To strengthen the 3D printed objects, Zhang et al. [45] propose a methodology that modifies the interior of the part with medial axis tree and surface of the model with a hexagonal frame pattern. The application of medial axis tree is the result of an inspiration that is outcome of an observation of human backbone structure. Also,

hexagonal surface pattern results from restricting centroidal Voronoi tessellation. Hexagonal pattern is connected to interior medial axis tree formation by the use of tree-like bars and resultant structure mechanically behaves better and can be printed with less material consumption. Several 3D models are designed by proposed method and tested both numerically and experimentally. Furthermore, proposed method is experimentally compared with existing methodologies which similarly modifies the interior structure by hollowing methodology or producing honeycomb-like patterns. For each scenario, same loading conditions are applied on equally sized models that are printed with same material. Results indicate that proposed method produces structures with higher stiffness using less material. Comparison of mentioned models is presented in Figure 2.18.

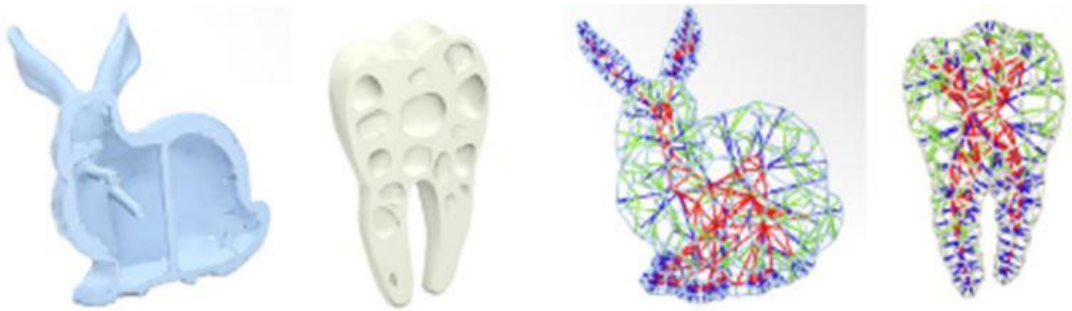


Figure 2.18. Bunny and tooth interior comparison, left; traditional hollowing methodology. Right, proposed medial axis tree formation [46].

Wu et al. [5] are inspired by porous bone structures and generate lightweight infill patterns for both 2D and 3D objects by applying topology optimization with voxel units. Also, in order to distribute material along the major and minor principle directions, anisotropic filters which define local voxel volume fractions are added to simulate the natural porous bone interior. The proposed high-resolution TO gives the opportunity of modeling complex porous structures with excellent mechanical performance. To validate this argument, method is compared with honeycomb-like and optimized Rhombic interiors numerically. The FEA results indicate that proposed infill is 1.5 times stiffer than the honeycomb-like and 1.14 times stiffer than Rhombic interiors. Simulations are given in Figure 2.19.

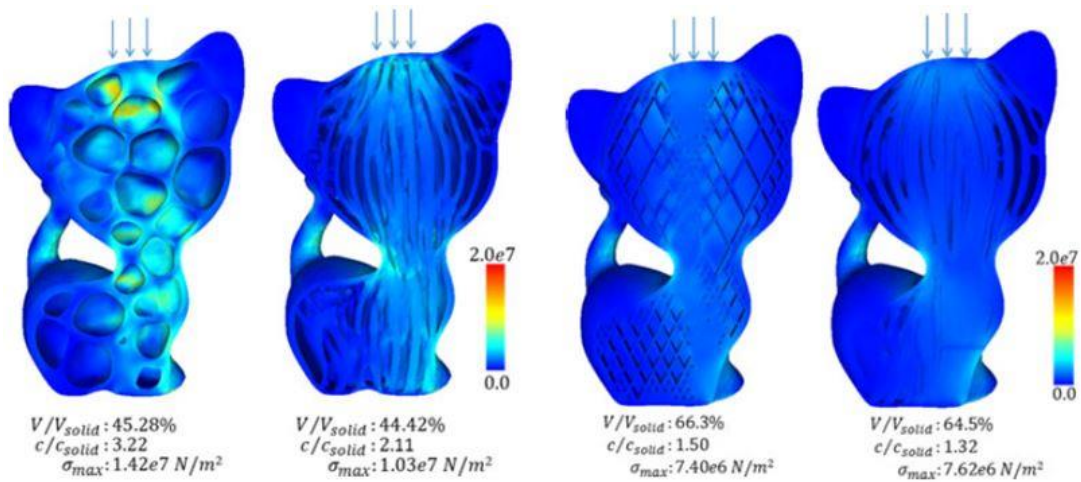


Figure 2.19. Proposed methodology is compared numerically with honeycomb-like interior and rhombic infill while keeping the volume fractions similar. Results state that there is an improved stiffness in both case [5].

Similar to previous study, Gomez et al. [46] are also inspired by natural porous bone structure. With this motivation, they propose a guidance to design functionally graded implants without shape constraint and to modify the interior of the scaffold in such a way that the constructed model satisfies the elastic modulus and permeability requirements. 3D Voronoi tessellation is used to create interconnected channels within the virtual model. The modelling steps are illustrated in Figure 2.20.

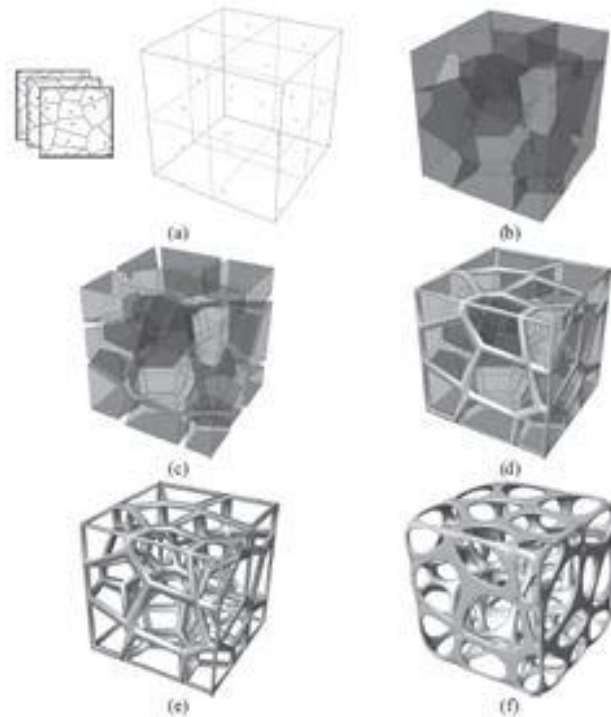


Figure 2.20. Scaffold modelling stages. (a) Closed volume is populated. (b) 3D Voronoi cells are generated. (c) Voronoi cells are hollowed by scaled portions. (d) Voronoi contours are capture. (e) Captured inner and outer contours. (f) Contours are smoothed by mesh operations [47].

The properties of trabecular bone such as thickness, cell amount, cell separation, ratios of bone volume to total volume and bone surface to bone volume; are exactly achievable with the 3D Voronoi tessellation technique. Furthermore, these histomorphometric properties together with the elastic modulus and level of permeability are adjustable during the design stage of Voronoi microstructures. Thus, a natural scaffold model that favors both cell migration and adhesion within it is constructible and model always can be altered to reflect realistic properties of another bone tissue.

Lu et al. [47] use 3D Voronoi tessellation to hollow the 3D models to make them lighter and more resistant to external forces. Study utilizes 3D Voronoi tessellation diagram to construct topologically optimized inner structures and formulates the main objective as maximizing the strength to weight ratio. The proposed algorithm hollows the interior in maximum way by using 3D Voronoi cells to relieve the inner stress

distribution. Furthermore, it creates small channels between the inner Voronoi cells to dissolve the support material after printing. The process chain is demonstrated on a 3D Kitten model, shown in Figure 2.21.

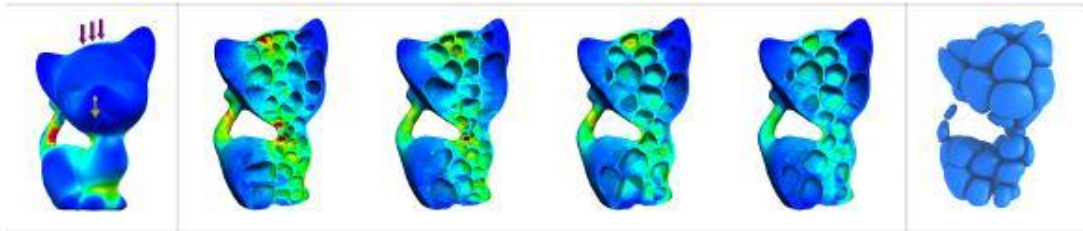


Figure 2.21. Proposed method chain. Left to right load and boundary conditions and optimization iterations are showed for Kitten model [48].

The proposed method is tested on various 3D models and their strength to weight ratios are controlled in a wide range. Also, printed artefacts are experimentally tested to compare the efficiency of the methodology with other interior porous structure methodologies. Results state that methodology proposes better strength to weight ratio in comparison with skin frame and strut type interiors.

Murr et al. [48] focus on functionally graded 3D porous biomedical implant models to replace patient-specific knee and hip bone stems by using EBM technology. The bone models are divided into several density regions and these regions are constructed virtually by using functionally graded biocompatible mesh arrays. Mentioned density optimization process enables bone ingrowth and components of an implant. The models are fabricated by EBM and use of Ti-6Al-4V powder material and mechanical properties, Young's modulus, is determined by damping and resonant frequency analysis. CT scans are embedded into CAD for EBM. Also, the effects of mesh complexity and density grade on hardness behavior of microstructures are observed. It is stated that density field alters the dimensions of cell models and this geometric variation significantly changes the martensitic behavior which is observed by opti-electron metallography. The bone model with an implant, CAD model of femoral bone rod and printed prototype of it are illustrated in Figure 2.22.



Figure 2.22. Left real bone with an implant is shown. Middle represents the CAD model of femur bone rod and right shows the printed model [49].

Ramirez et al. [49] mix Cu powders with additional Cu precipitates to fabricate microstructures in the form of reticulated mesh and open cellular foam with varying density levels. EBM printed artefacts are tested and mechanically compared with the Ti-6Al-4V mesh and foam structures. The addition of Cu precipitates to strengthen the mesh struts and foams and improves the hardness value 75 % in comparison with the regular Cu artefacts. Also, Young' modulus versus density and relative stiffness versus relative density plots and values are in the agreement of Gibson-Ashby cellular model and very close to Ti-6Al-4V values. It is stated that the proposed open cellular foams and mesh structures of Cu are future candidates for engineering applications due to excellent thermal and electrical conductivity behavior of Cu which is opposite for Al counterparts.

An analytical model is developed by Zhu et al. [50] to model the compression behaviors of the irregular 2D Voronoi cellular models. The low density Voronoi textures under constant compressive engineering strain of 0.6 are modeled in ABAQUS. Straight elastic beam model with constant thickness is attained to Voronoi

walls. Also, regularity parameter is defined into the model to inspect the effects of level of geometric irregularity. It is stated that at fixed level of relative density, at low strain values, irregular Voronois have higher tangential modulus and they can handle lower compressive loads at higher strain values, compared to more regular Voronois. In order to model effectively the compression behavior low density Voronoi textures, a combined approach is proposed, which consists of springs in series and parallel configuration methodology. Although the proposed combination predicts the stress strain response better, springs in series analogy is more effective in high strain applications. Furthermore, the maximum bending strain of the cell wall is determined under compressive loads. Thus, the yielding strain is predictable.

Sotomayor et al. [51] took one step further and investigated compression behavior of irregular 3D Voronoi cells in elastic and plastic regions. Similar to previous one, the level of regularity is set by a parameter and controlled with SSI method. In addition, the effects of relative density are studied and compared numerically and empirically with other studies. The irregular 3D Voronoi foam models are generated for different regularities and densities and the elastoplastic behaviors of these models are simulated for a wide range of strain values.

2.6. Multi-Material Porous Infills

Up to now, main aspects of this study are supported by related literature studies. It is shown that Voronoi concept is applicable in various fields of engineering. Also, due to its natural gift structure, it is favorable to study and experimentally usable in AM applications. Furthermore, the concept and benefits of AM is covered with automated algorithms and implemented methodologies to improve the ease of use. Different examples are covered to prove that AM is one of the most suitable methodology that coherently works with single chain or multi-purpose algorithms to assist the user in a simple manner.

Related to this study, examples of regular and irregular interior porous structures having functionally graded density fields are illustrated. Conceptual difference of

mentioned models clearly shows that upcoming engineering trend will be in connection with mentioned concepts and this claim is supported by outstanding performance of presented artefacts in intended applications.

Last part of the literature chapter points out the multi-material concept in AM, helpful solutions against problems and favorable outcomes of it like the advantages of stated aspects. It can be considered that following two literature studies give clue about the upcoming works and enlighten the future purposes.

Yan et al. [52] have studied on multi-material concept and gave an alternative solution to the question of obtaining strong and durable printed artefacts. In this study, the concepts of AM and material injection is combined to produce stronger 3D objects. The utilization of triply periodic minimal surfaces, TPMS, as an interior structure of a model creates internally connected smooth channels that are filled by injected material. Resulting multi-material model is mechanically stronger and withstands larger external forces. The algorithm behind the process starts with FEA and 3D model to visualize the subsequent stress field. Then TPMS channels are generated and optimized geometrically in accordance with the weak regions seen in stress field. Then channels are offset to increase the width. Another FEA is performed to calculate stress field of modified interior structure. Channels are further optimized accordingly the latest FEA result and resulting internal geometry becomes sustainable against the applied forces. The last part is printing the modified interior 3D artefact and injecting material into channels to reinforce the 3D object. The section views of empty and filled artefacts are seen in Figure 2.23.



Figure 2.23. 3D model of Kitten (left), TPMS channels (middle) and injected material (right) [53].

Additionally, printed artefacts are experimentally tested to show that empty version of the model, honeycomb filled model and topologically optimized model are weaker in the manner of load carrying capacity.

As the material variety, multi-material usage and model resolution increases, it is become challenging to compute a model with current 3D software. Vidimce et al. [53] presented a programmable model, OpenFab, to design multi-material 3D models. Presented model supports geometrically complex models with multi-material composition and feeds the 3D printer with a low memory input. OpenFab is guided by continuous material definition, flowing architecture, procedural synthesis and separating material definition from 3D model. Flow chart of OpenFab is given in Figure 2.24.

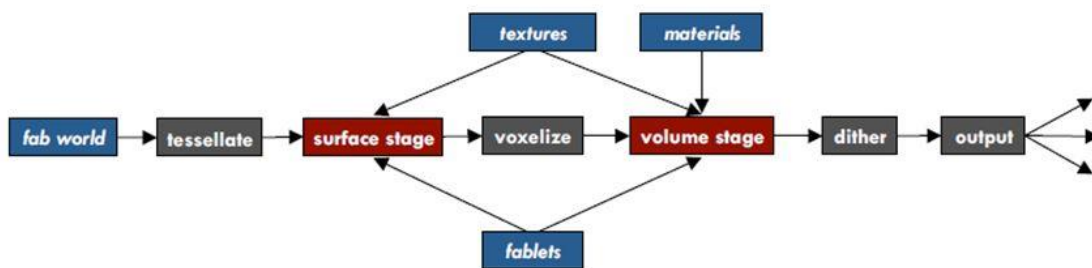


Figure 2.24. The pipeline of OpenFab [54].

Program considers 3D models as boundary representations, BREPs, and takes these BREPs together with printing materials and textures as inputs. By evaluating these inputs, OpenFab creates a separate volumetric printing material definition which is

exactly for the device in use. Grey boxes define characteristics of printer and parameters of it. Red boxes are for user to control design parameters. Several multi-material artefacts are printed by using OpenFab pipeline.

CHAPTER 3

METHODOLOGY 2.5D

3.1. Introduction

In this chapter, 2.5D models are internally modified by Voronoi patterns to demonstrate superior mechanical behaviors under pre-defined loading conditions. A closed design region firstly undergoes TO process to reveal the stress distribution, density field and deformation characteristics under pre-defined loading conditions. Once the high density regions are obtained within the material, it is smoothly separated from other regions. Secondly, Voronoi cells are generated in accordance with the TO results in such a way that material, in this case Voronoi cell walls, is distributed among these regions to simulate the material distribution. Thus, high density region is constructed by populating more Voronoi cells compared to low density regions. In other words, high density regions are filled with closely packed Voronoi cells to increase the material amount.

The current chapter consists of two phases. In the first phase, manual steps are taken to validate the approach and it is tested by only FEA on two different examples. For the second one, a novel algorithm is proposed to verify the same approach is applicable to different geometries, is more efficient and can be carried out automatically. Furthermore, these claims are tested both numerically and experimentally to show the accuracy of the FEA results proposed by the algorithm.

3.2. Manual 2.5D Test

3.2.1. Proposed Approach and Test Cases

The main objective of the approach is to construct a Voronoi pattern that minimizes the maximum deflection of the part while lowering the mass of the object as low as

possible. For this purpose, a solid model is firstly designed in Inspire 2016 environment, a topology optimization solver, to obtain topologically optimized geometry under the defined load-support conditions. The steps of this process in Inspire 2016 are shown as follow;

- Designing a 3D model
- Defining Material Properties
- Defining Load and Support Points-Surfaces-Regions, Conditions
- Defining Penalization Factor and Safety Factor

Inspire 2016 uses Solid Isotropic Material with Penalization (SIMP) Method to discretize the design domain into isotropic solid microstructures, called as finite elements [62]. Each element within the domain has defined material properties like density and Young modulus. Thus, design domain is constructed as density field. By setting penalization factor, SIMP methodology penalizes the contribution of finite elements with intermediate densities and tries to maximize the overall stiffness of the system, which is the objective function behind the work. So, overall stiffness of the model is found iteratively and it is displayed with elements that are either solid material or void. The following formula of SIMP methodology gives the overall stiffness matrix of the system:

$$K_{SIMP} = \sum_{e=1}^N [\rho_{min} + (1 - \rho_{min})\rho_e^p]K_e \quad (1)$$

where ρ_{min} represents the minimum relative density, ρ_e states relative density of an element, p is the penalization factor, N is the number of elements within the system and K_e is the stiffness matrix of these elements. Also, the objective function of the algorithm can be summarized as follows:

$$\min C (\{\rho\}) = \sum_{e=1}^N (\rho_e)^p [u_e]^T [K_e] [u_e] \quad (2)$$

where $\{\rho\}$ is a vector that covers the relative densities of the elements while $[u]_e$ is the displacement vector of them. Each iteration step is carried if the following constraints are satisfied:

$$\sum_{e=1}^N \{v_e\}^T \rho_e \leq Mass_{Target} \quad (3)$$

$$[K\{\rho\}]\{u\} = \{Force\} \quad (4)$$

v_e is volume of the element, K is the global stiffness matrix that is controlled by relative density vector, u is the displacement vector and ‘Force’ is applied external load vector. Thus, each iteration satisfies the objectives of target mass, force-stiffness equilibrium and safety factor if it is defined. Also, during each step, optimization algorithm completes sensitivity analysis that is the derivative of the objective function with respect to element densities to estimate the effect of element density variation on overall stiffness.

$$\frac{dC}{d\rho_e} = -p(\rho_e)^{p-1} [u_e]^T [K_e] [u_e] \quad (5)$$

Throughout the sensitivity analysis, low density elements lose their contributions and they are eliminated. Since, the sensitivity analysis is applied on each element and connectivity between them is considered at the same time, the resultant element distribution is continuous within the design geometry. In the following chapters, another TO solver, Millipede [55], is to be employed. This software also uses the SIMP methodology and does the same work with Inspire 2016.

After several iterations, geometrically complex TO result is smoothed in CATIA V5 environment, CAD software, because of the fact that the complexity of the resultant geometry significantly increases the work load of FEA and also it makes printing process rather difficult. After simplification, the smoothed geometry is imported to Rhinoceros 5 environment, CAD software, and the cross section of the simplified 3D geometry is used for generating 2D Voronoi patterns by use of

Grasshopper3D, a plug-in of Rhinoceros. Once the Voronoi pattern is defined, geometry is extruded in the direction of thickness of the real model and 2.5D optimized Voronoi infill shell geometry is created. The resultant model is taken into the FEA solver and it is analyzed under the same conditions which are used for TO. Hypermesh and ANSYS software, FEA solvers, are used for this purpose. The proposed approach is tested on two different case studies.

For the first case study, wing geometry of F-16 Fighting Falcon is simplified and modeled as simple 3D beam geometry with the dimensions of $500 \times 1000 \times 10000$ ($W \times H \times L$) in meters. Lift force that is created by airfoil geometry and acts over whole surface of it is simulated by applying 1 kN force at each tip and supported at the middle just like wing is attached to aircraft in the middle. For the sake of simplicity, Al 2024 is selected as beam material since different heat treated versions of Al 2024 is commonly used in structural applications of aerospace. The following Figure 3.1 demonstrates the simplified model with load-support conditions and the real aircraft.

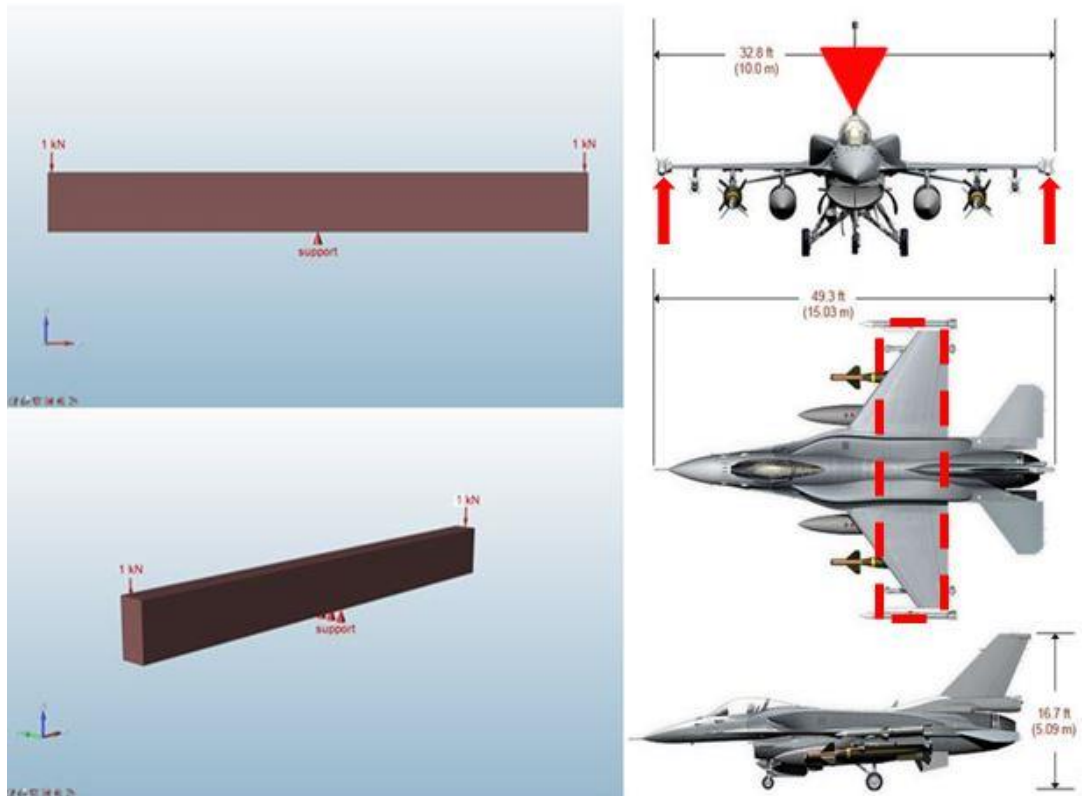


Figure 3.1. Left, 10 meters solid beam model is subjected 1kN force at each tip and simply supported at the middle. It is made of Al 2024 and weight of it is 13350 kg, modeled in Inspire 2016. Right, the dimensions of real F-16 Fighting Falcon with wingspan of 10 meters. Empty weight of the aircraft is 9207 kg and max. take-off weight is 21772 kg. Simplified beam system is shown on F-16 figure, dashed rectangle represents beam, red arrows show 1kN forces and flipped red triangle represents support region.

One of the objectives is trying to get rid of excess material to reduce the total weight and gaining superior mechanical properties at the same time. To do so, the generated CAD model is subjected to TO process. The penalization factor is chosen as 3 in order to get truss-like structure and safety factor is set to 2 for the iterations. They highlight the general look of the system. The evaluation of optimum density distribution for given model is shown in Figure 3.2.

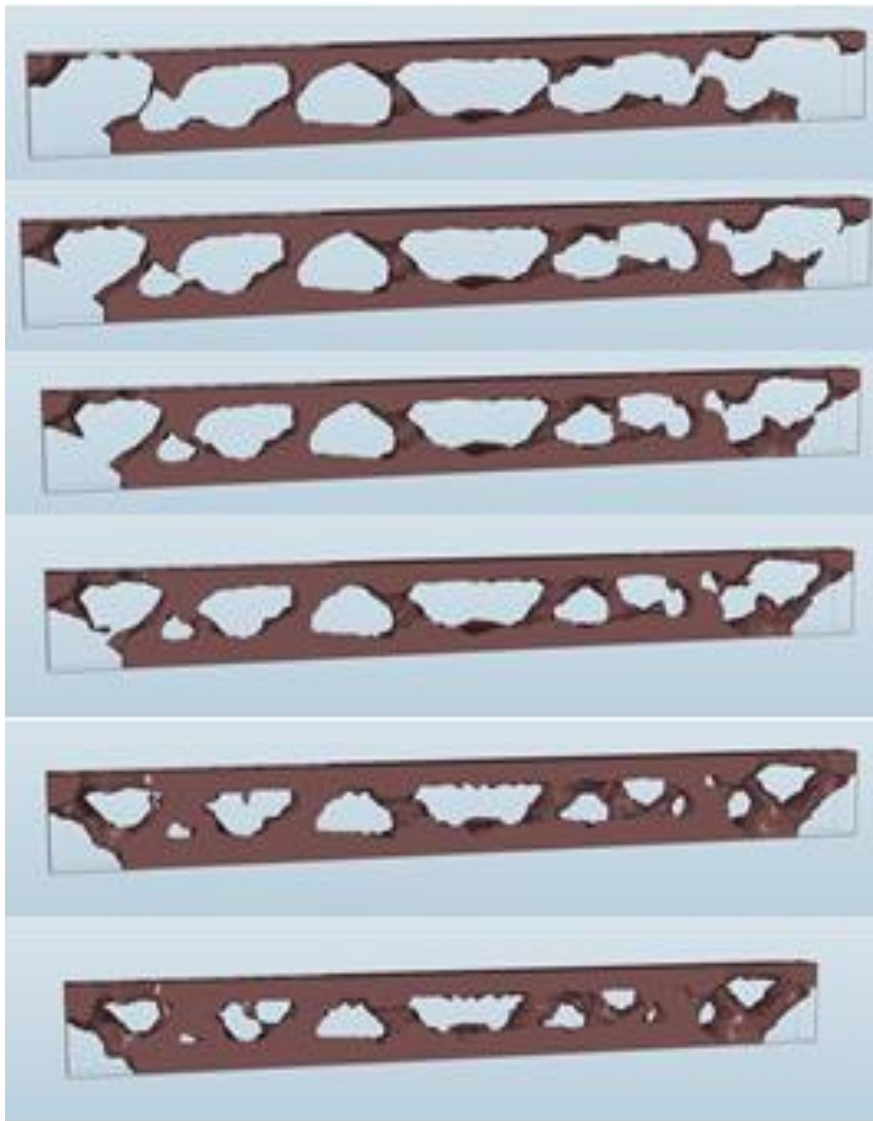


Figure 3.2. The evaluation of optimized truss-like structure.

As it can be seen, optimized topology is insufficient to be used in realistic applications due its geometrical complexity. Also, the complexity of it creates unnecessary work load during FEA and printing stage. Thus, optimized topology is modified manually in CATIA V5 environment by simple smoothing operations. After number of curves smoothing operations, the beam and the system take the final form and it is shown in Figure 3.3.

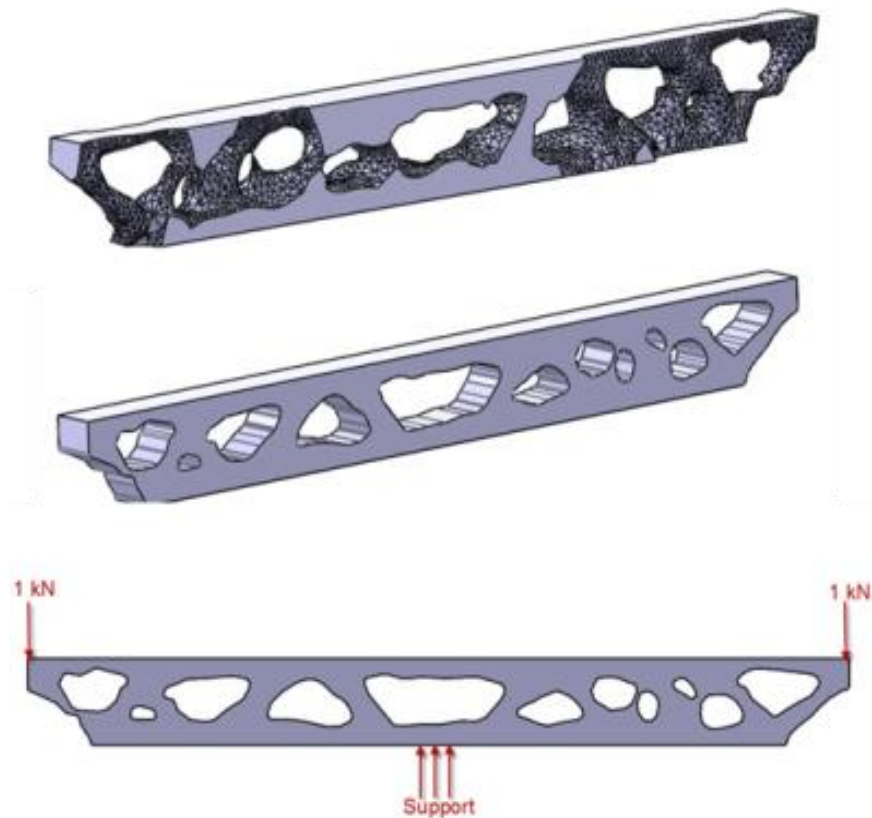


Figure 3.3. Original optimized 3D beam model (above), smoothed model (middle) and current system (below).

Next step is the distribution of 3D Voronoi Cells into the body so the geometry should reflect the similar result with topology optimization. Behind this motivation the key idea is trying to achieve similar mass distribution with TO by adjusting the number of Voronoi seeds and size of them. Rhino 5 and Grasshopper are useful tools for this process. So, Voronoi cells are populated within the cross section of the simplified TO geometry. The main goal is populating more Voronoi cells in denser regions while keeping the overall shape of the design model the same, which is a beam model in this case. The optimized Voronoi cells distribution is compared with actual TO result and smoothed model and also final geometry is shown in Figure 3.4 to validate that result is still applicable with the design requirements.

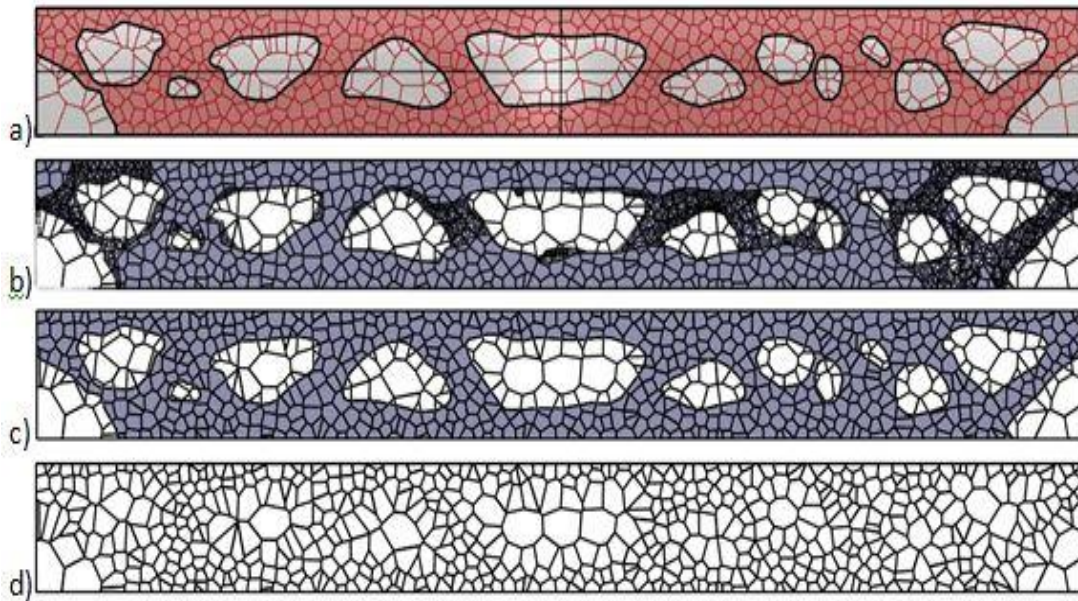


Figure 3.4. Optimized Voronoi distribution with 600 Voronoi cells. Generation (a), comparison with actual TO result (b) and with smoothed TO result (c). Final applicable model (d).

In this case, total number of 600 Voronoi seeds is populated within the boundary region. Ratio of 1/5 is set to decide how many seeds are populated in denser regions. 500 hundred seeds are populated randomly in critical regions so that remaining 100 seeds are placed in low density regions. Then, optimized 2D geometry is extruded in the direction of the thickness and shell model is therefore prepared for FEA.

For the second case study, a simple L beam is modeled and subjected to load-support conditions. Figure 3.5 illustrates the simple system.



Figure 3.5. Simple L beam, short arm is 100 mm, long arm is 150 mm, the sharp inner corner is filleted with the radius of 15 mm and the in-plane thickness is 10 mm. Tip of the longer arm is subjected to 100 N while short one is fixed.

Similar to the previous case study, TO process is performed in Inspire 2016 with the same configuration settings and resultant 3D geometry is smoothed in CATIA V5. By using Rhino 5 and Grasshopper plug-in, 200 Voronoi seeds are populated in accordance with the TO material distribution and this time ratio is set to 1/3. Different than the case study one, another L beam model is constructed by randomly populating same number of seeds without any region restriction within the boundary region. 2D infill patterns are extruded in-plane direction to create shell models for FEA. TO result, optimized Voronoi pattern and random Voronoi pattern models are shown in Figure 3.6.

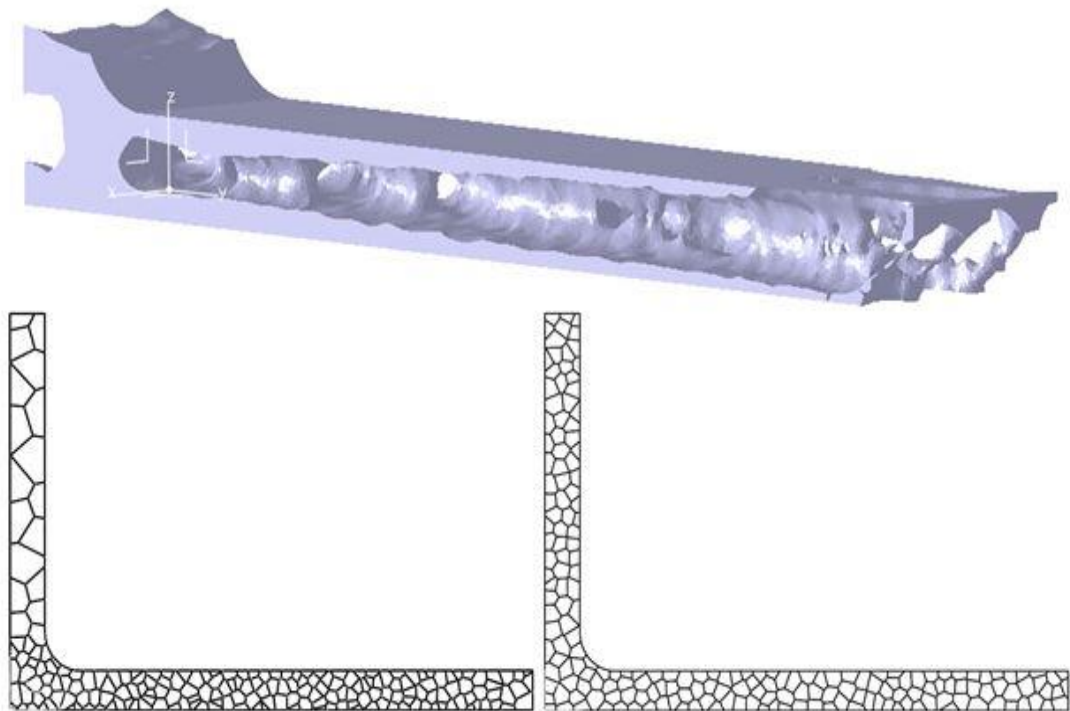


Figure 3.6. Optimized 3D geometry by Inspire 2016 (top), 2D optimized Vorono infill pattern with 150 seeds in critical region, 50 seeds in low density region (bottom-left) and 2D random Voronoi infill pattern with total 200 seeds (bottom-right).

3.2.2. Models

This subsection covers the FEA results of each case and predicts the performance of the proposed approach on different geometric models. In order to investigate the

contribution of optimized Voronoi infill pattern into the mechanical properties of the simple beam, both simple solid beam model and smoothed optimized beam model undergo FEA with the same configurations such as load amount and location, support type and location. In addition, to realize the effectiveness of the proposed approach, random and optimized Voronoi L beam models are compared within each other in terms of mechanical stiffness.

One of the main objectives of the case study one is to modify the interior structure of the simplified wing model by using Voronoi infill to lower the overall weight since the weight of the solid beam is already higher than the whole aircraft. To accomplish this manner, TO methodology is applied to numerically prove that equivalent amount of lift force can be carried by less amount of material. Furthermore, the proposed Voronoi approach shows that overall geometry can be kept persistent with the initial geometry while reflecting the material distribution phenomena. Another objective is that constructing a Voronoi pattern that minimizes the maximum deflection of the part under the given loading conditions. To validate this objective, Small Deformation Theory is assumed during FEA and key objectives are defined as maximum stresses within 3D models and amount of tip deflection. At the first case, only the effects of Voronoi infill pattern and wall thickness are compared with solid and optimized models. FEM of optimized Voronoi, smoothed and solid beams are shown in Figure 3.7 and also, FEA values are tabulated together with the total mass values in Table 3.1.

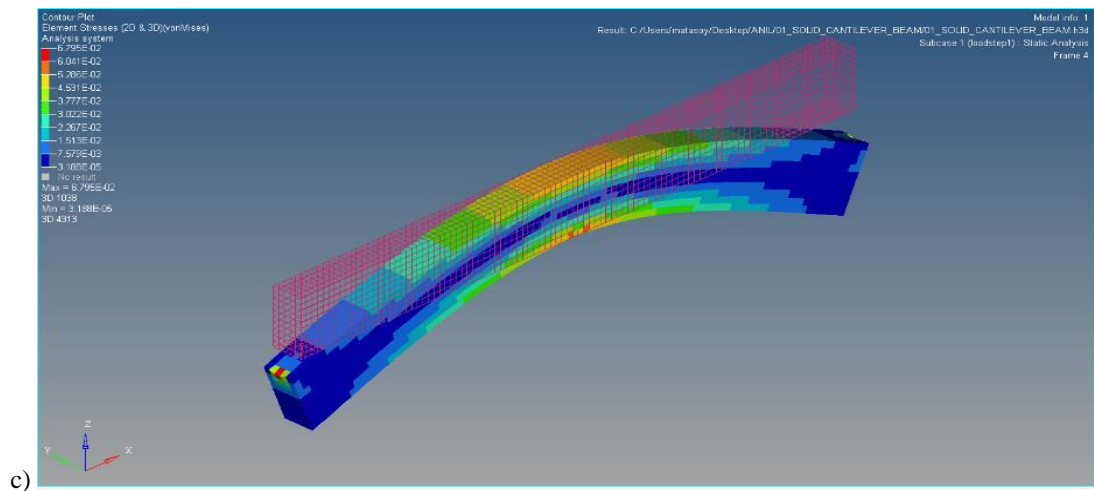
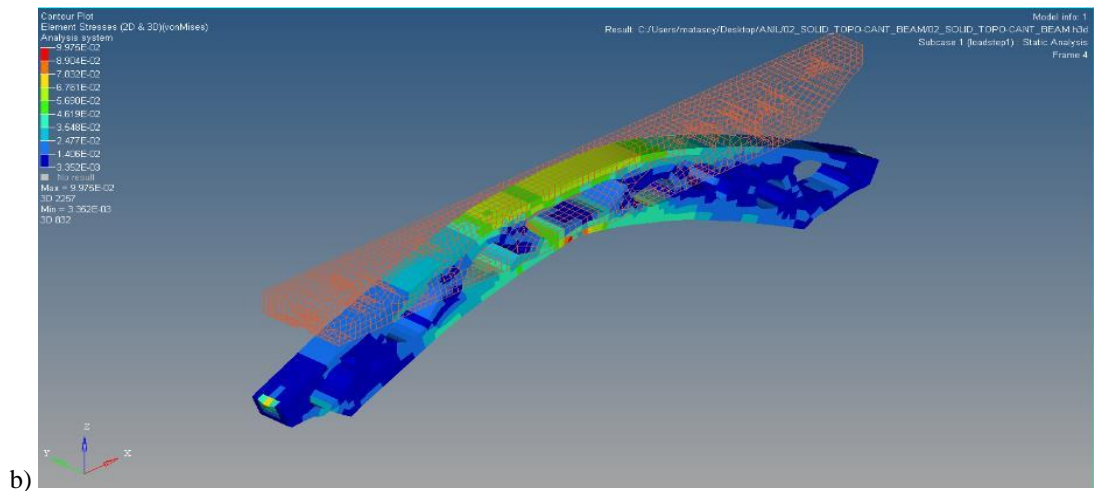
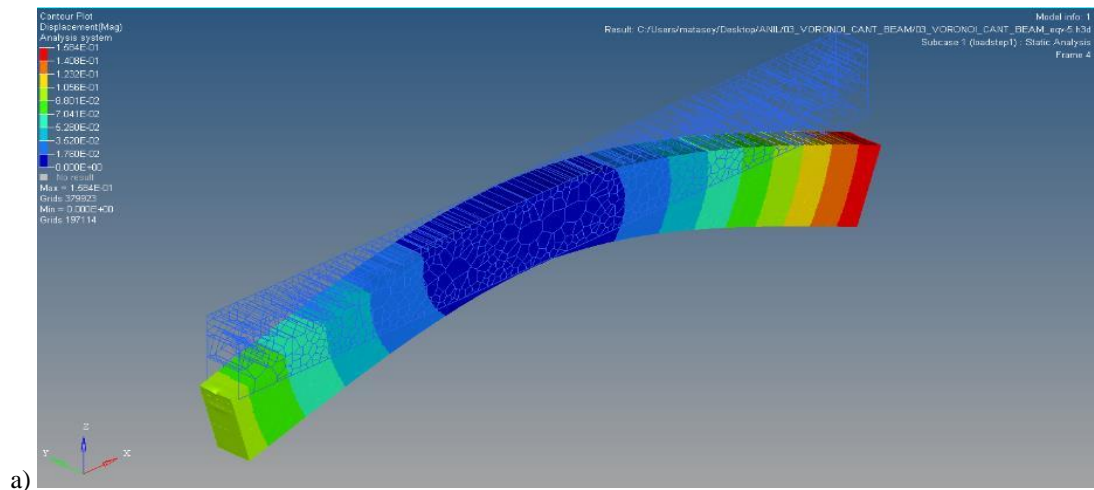


Figure 3.7. FEM of beams in stationary and deflected states, (a) Optimized Voronoi, (b) Smoothened and (c) Solid.

Table 3.1. FEA results of beam models.

Type	Maximum Von-Misses (MPa)	Maximum Displacement (mm)	Mass (kg)
Voronoi (1mm)	35.43	1.852	459
Voronoi (10mm)	2.82	0.158	4590
Smoothened	0.099	0.019	8118
Solid	0.068	0.017	13350

It is evaluated that the overall mass of the Voronoi beam changes linearly with the thickness of the cell walls. Furthermore, mentioned thickness has crucial effect on the mechanical properties of the system and it is simplified that there is a linear relationship between wall thickness and tip deflection. It is concluded that maximum tip displacement of the Voronoi beam is applicable in aerospace applications and optimized Voronoi infill pattern is successful for lowering the total mass by 60-90 %.

As it is stated in the second case, the mechanical characteristics of Voronoi patterns are compared between two different Voronoi patterns, random and optimized Voronoi infills, to simulate the effectiveness of the optimization process. Equivalent number of Voronoi seeds is populated within these structures and they are subjected to the same load-support conditions. To minimize the effect of meshing quality on FEA in ANSYS, similar number of elements and nodes are defined to construct FEMs. Total deflection and equivalent stress results of the L beam models are simulated in Figure 3.8.

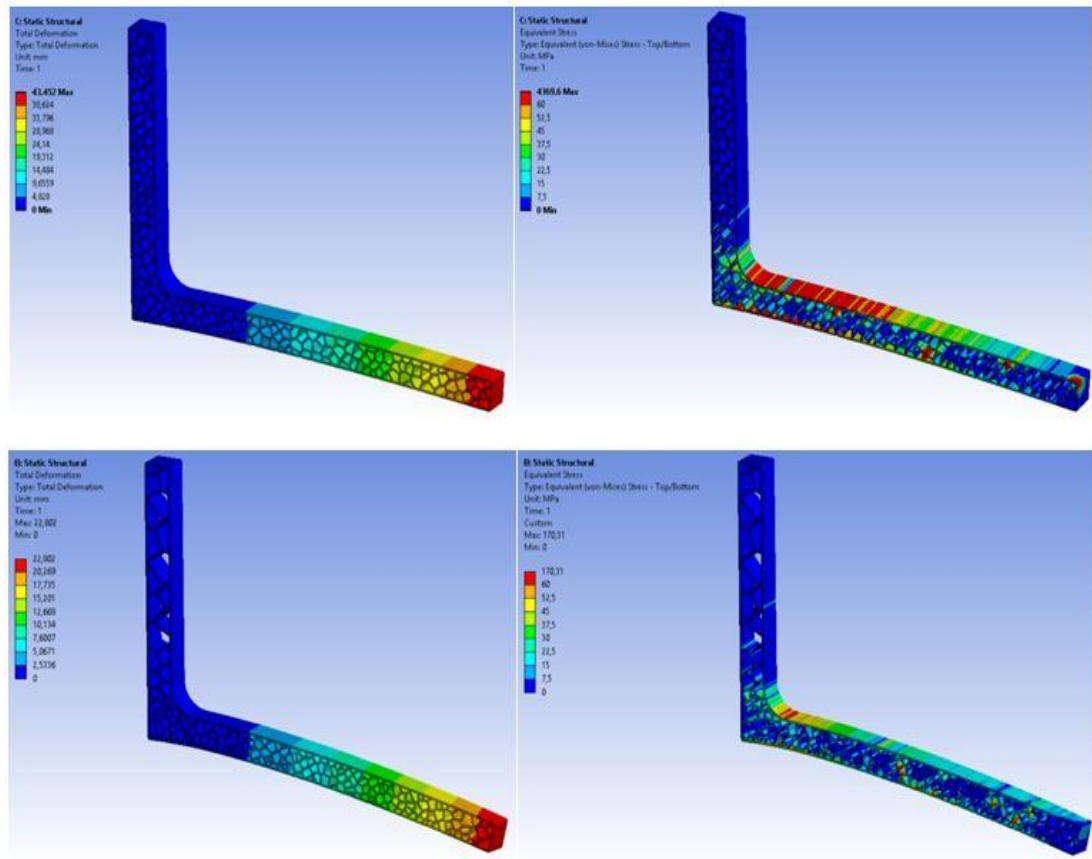


Figure 3.8. Deflection shape and stress distribution of random Voronoi L beam (first row) and optimized Voronoi L beam (second row).

Also, numerical results of FEA are tabulated in Table 3.2 below.

Table 3.2. Results of FEA.

Type	Stress Max. (MPa)	Stress Min. (MPa)	Displacement Max. (mm)	Displacement Min. (mm)
Random Voronoi	4369.6	170.31	43.452	9.9865
Optimized Voronoi	16.583	11.598	22.802	6.3885

To sum up, in this chapter the proposed approach is evaluated by two different case studies. First case study demonstrates that optimized Voronoi infill pattern is valid to reduce the overall mass of the system while keeping the desired mechanical properties

and it is applicable to maintain the design geometry without altering it. In addition, second one numerically proves that integration of TO phenomena into Voronoi infill pattern application is effective for generating stiffer models. Both case studies are evaluated numerically and manually in 2.5D environment.

3.2.3. Limitations of Manual 2.5D Test and Possible Future Directions

This chapter has presented a novel manual method of combining TO and FEA methodologies with AM to construct naturally inspired Voronoi infill patterns. Under specific load and support conditions, TO methodology determines the critical regions within the structure and Voronoi seeds are populated in accordance with the design requirements. FEA works on the generated geometries and it is numerically proved that proposed methodology gives the mechanically optimum result. Overall mechanical performance of the system is enhanced while total mass is minimized.

At this point, each step of the presented work is done manually which gives excessive work load and time to the user. Problem is geometrically defined in Inspire 2016 and further topologically optimized. Resultant optimized 3D geometry is taken into CatiaV5 for smoothing operations. Then, smoothed 2D sketch is transferred to Rhinoceros 5 for cell generations. Constructed infill pattern is extruded in the thickness direction to form final 2.5D part model. 2.5D model is moved into ANSYS to numerically analyze the mechanical performance of the part under pre-defined load-support conditions and also to compare the performance and stiffness of the optimized model. One of the future works is automating the presented process to obtain optimum work period and load. Another one is applying the proposed methodology to more common simple engineering problems such as simply supported beam, compression and cantilever beam systems. Even though wing model and simple L beam numerically prove that optimized Voronoi infills accomplish the design requirements and it is applicable, it is essential to adopt the methodology on more realistic examples and to validate the outcomes with experimental procedures. Thus, experimental validation is another upcoming future work. Lastly, it is also necessary to compare the

proposed 2.5D Voronoi infill pattern with random Voronoi infills and also common infills which are pre-defined in the libraries of regular 3D printers. This way may give better understanding about the Voronoi nature and shows the usefulness of the proposed approach. All these limitations are managed in the upcoming chapter and overall workflow is improved.

3.3. Auto 2.5D Test

3.3.1. Proposed Approach and Test Cases

In this section, it is shown that proposed methodology is improved by designing an algorithm to overcome the limitations of the previous work. The main objective of the algorithm is to construct a Voronoi pattern that minimizes the maximum deflection of the part and to keep the mass of the object as low as possible compared to the randomly distributed Voronoi cells pattern. For this purpose, design volume is firstly constructed in Rhinoceros 6 – Grasshopper environment, subjected to TO and then seeding part of the algorithm constructs the final geometry. At the end, FEA works on these geometries and genetic multi-objective algorithm iterates through the possible solutions to obtain the most efficient geometry. The general flow chart and main aspects of the algorithm are shown below.

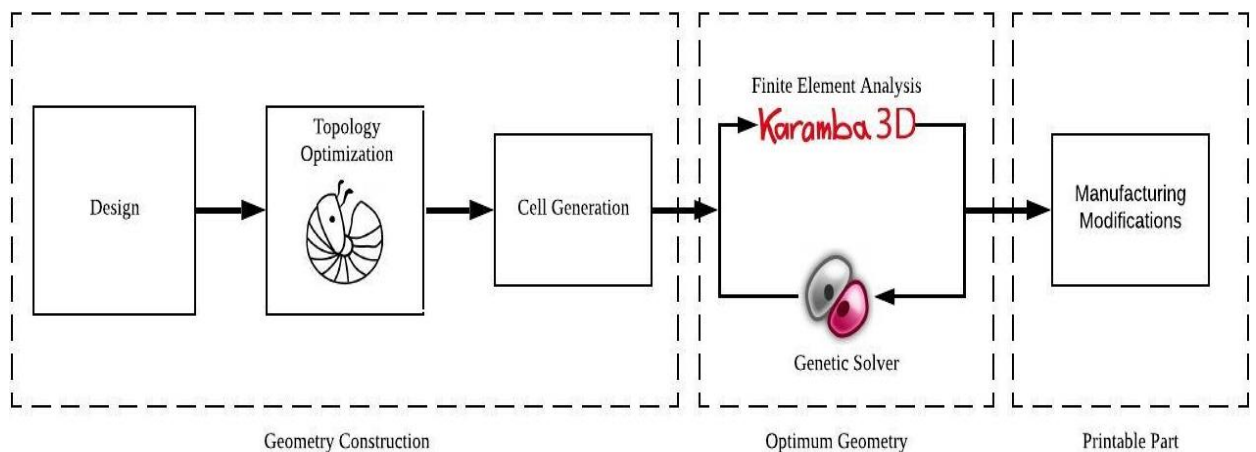


Figure 3.9. General flow chart of the proposed method [61].

Table 3.3. Main aspects of the algorithm [61].

	Geometry	Voronoi Cells	TO Solver	FEA Solver	Genetic Solver
Objectives	Minimum deflection	Minimum deflection			
	Minimum mass	Minimum mass			
Variables	Load / support locations	Number of seeds	Load / support locations	Load / support locations	Number of results per iteration
			Load / support types	Load / support types	
			Boundary region	Boundary region	Carrying over percentage
	Boundary region		Target density	Element type	Number of results in first iteration
			System resolution	Element cross section	
			Number of iterations	Material	Inbreeding percentage

Our algorithm creates three different Voronoi infill patterns which are namely fully random Voronoi distribution, optimized-1 Voronoi distribution and optimized-2 Voronoi distribution. Regarding the first one, the algorithm populates all seeds in restricting boundary region without any further limitation and generates random Voronoi infill pattern. For the second case, the algorithm uses the results of TO to create the additional boundary regions and populates limited amount of seeds in these regions. Optimized-2 Voronoi distribution also creates density regions and populates limited amount of seeds in them. Additionally, the third approach restricts the growth of Voronoi sites in the related regions. A number of stages add complexity to the algorithm. However, the work is led through the autonomous path until the end use models are obtained. Additionally, the application of TO at the very beginning enables the algorithm to produce optimum results. All input variables are the same for these three approaches. Detailed flow chart illustrates these three approaches in Figure 3.10.

For the optimized-1 system boundary regions and geometry are firstly defined in Grasshopper, a Rhino plug-in [54]. Then, the related load-support types and their locations are given by the user. These variables are combined with Millipede inputs that are target density (0.4), system resolution (0.5 mm squares) and number of iterations [55]. Output is topologically optimized mesh geometry which is represented as a density field. Meshes with high density values are captured and enclosed. These

density regions are defined by 2D isocurves. After that, the user inputs the total number of Voronoi sites and the algorithm populates some of these points in higher density regions and the remaining of them in lower density regions. In our test cases, we populate 175 sites randomly, 100 of them called as the effective seeds placed in higher density regions. At this point, we distribute 75 sites according to the areas of the low-density regions. Higher amount of seeds in high density regions result in more closely packed Voronoi cells where there will be more deployed material during the fabrication. This improves the performance of artefacts under the loading conditions. Figure 3.11 illustrates this purpose clearly.

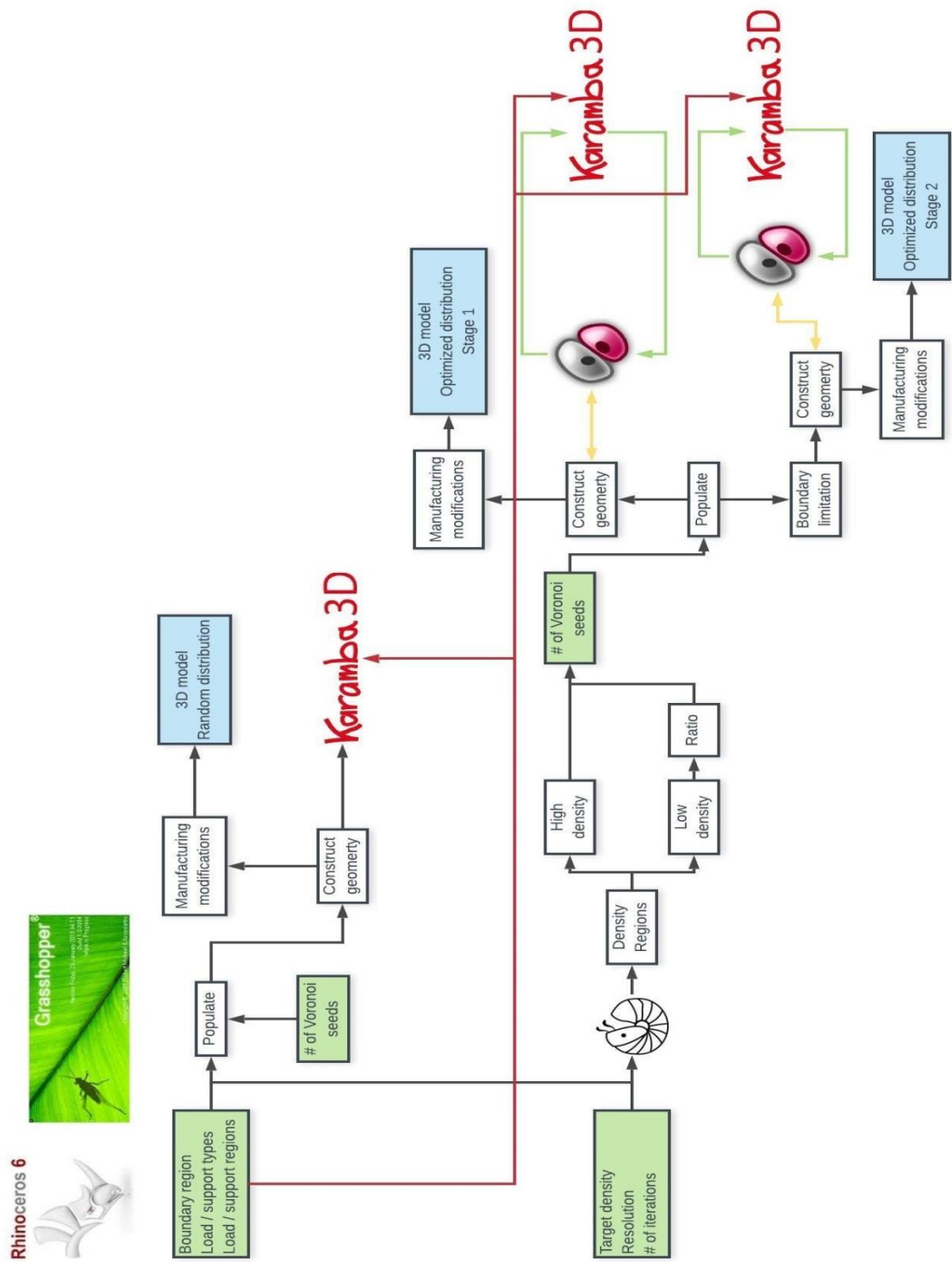


Figure 3.10. Flow chart of the proposed method [61].

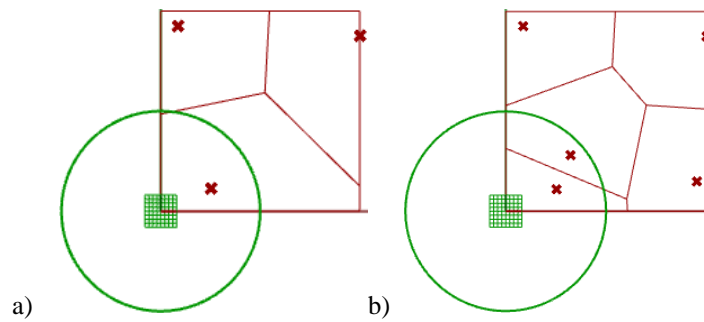


Figure 3.11. Green circle represents objective region in which material (Voronoi site walls) should be maximized. Initial geometry (a) supplies limited amount of material to the corresponding region. Adding sites in the region increases the amount of material (b) [61].

In order to make this purpose more effective, optimized-2 system is constructed in such a way that the growth of effective Voronoi cells are allowed only in the enclosed isocurve of high-density regions. Similarly, growths of remaining Voronoi cells are limited by their birth regions. Figure 3.12 illustrates the mechanism for three-point bending model.

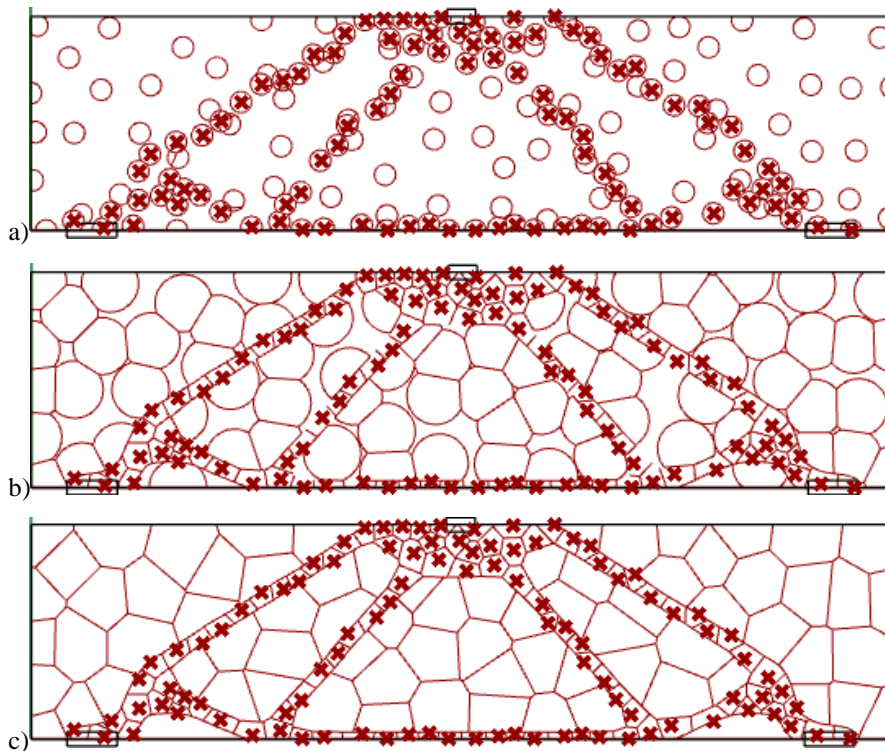


Figure 3.12. Cross points represent effective sites. (a) All Voronoi cells grow at the same rate in the beginning. (b) Effective cell growth is limited by the isocurves of high-density regions. (c) Remaining cells continue to grow until they fully fill the low-density regions [61].

As it is mentioned before, the algorithm creates randomly distributed geometry which has exactly the same boundary region. Finally, three beam models with different infill patterns are obtained with the same amount of sites. Beam models are then defined into the first FEA stage. Karamba3D is also a plug in for Grasshopper, performing FEA in both 2D and 3D environments [56]. Resultant beam models are meshed using linear beam elements, because of the fact that Voronoi site walls are represented by lines in 2D. Support / load locations and types, element cross section and material are defined exactly the same for the random and optimized models. In addition, in order to minimize the errors in FEA results, supporting and loading points are defined in regions which are used in TO stage. Thus, three models of FEA become similar to the models used in TO. It is important to note that the defined material in FEA is not PLA which is used for 3D printing the models. The default material library of Karamba3D does not have mechanical properties of PLA material, aluminum is chosen for simplicity. Another important issue is that our models in Rhino 6, Grasshopper and Millipede environments are represented in millimeter and Newton. Whereas, Karamba3D gets its inputs in the meter and kilo-Newtons. Since we are trying to obtain an automated algorithm, we have to use these four software simultaneously. It is reasonably fine to consider the changes in weight and the maximum deflection results as percentages in order to compare the variations between the beam models. As a consequence, we use a performance equation ($P = (m \cdot u_{max})/1000$) to compare the improvement of the beam models. Average and maximum stress values of beam models guide us for future experimental results. We may also guess the failed geometries since we can visualize the deflected beam models in Karamba3D.

Since site locations are randomly chosen by Grasshopper, we may get thousands of different infill geometries and FEA results. Thus, an efficient tool of Grasshopper, Galapagos, an evolutionary problem solver is included at the end of the algorithm [57]. Among thousands of possible Voronoi infill patterns Galapagos determines the optimum ones for the two algorithms. Genetic algorithm has five interlocking parts;

- Fitness Function

- Selection Mechanism
- Coupling Algorithm
- Coalescence Algorithm
- Mutation Factor

Fitness function defines the objective, obtaining the lowest P value in our case.

$$\min P(m, u_{max}) = \frac{m_n \times (u_{max})_n}{1000} \quad (6)$$

Among isotropic, exclusive and biased mechanisms, we chose exclusive selection mechanism to keep only the top suitable %25 of the total population. Additionally, to produce new generations from the top %25, we defined 0% breeding factor among -100% and 100% for coupling algorithm. Thus, we were able to mate the mid-range P results within each other. Crossover coalescence is applied to produce new models with similar P values. Crossover randomly takes the input values of coupled members of the population and creates a new child from these inputs. At each step, point mutation could be applied to change the topology of the children but mutation is not used in this work. Briefly, Galapagos employs a kind of trial and error method to get the optimum result for the defined design criteria. The inputs (random seed locations) are defined as genes and the results are defined as the genomes which are performance values coming from the FEA. The initial step of Galapagos is about populating these genomes resulted by the combinations of the genes. It is reasonable to assume that genomes having lower performance values are potentially closer to the optimum result. Thus, Galapagos removes the genomes with higher values and moves on with the lower valued genomes and their genes in the next iteration. Although, genetic algorithm is slow and does not guarantee the best solution, it is flexible and applicable for our cases and converges the optimum results. Last part of the algorithm is about obtaining the manifold artefacts. For this purpose, random and iterated geometries undergo manufacturing modifications. It is important to remember that the main objective of the study is to determine the optimum Voronoi infill pattern and compare it with the random one to observe the effects of interior structure on the mechanical

performance. Thus, for Voronoi sites, we choose 0.8 mm constant wall thickness which is exactly the same with the cross sections of the FEA beam elements visually and 0.4 mm constant wall thickness for the outer shell. External geometries of the artefacts are kept consistent with the design requirements while decreasing the material consumption.

Following sub-section presents the random and the optimized-2 beam models for three different test cases; three-point bending beam model, cantilever beam model and compression beam model.

3.3.2. Models

These models are constructed for the three-point bending, cantilever beam and simple compression experiments. The defined systems and the resultant density fields for the mentioned models are shown below in Figure 3.13.

By setting penalization factor as 3 and target density as 0.4, after 30 TO iterations, 175 Voronoi sites are populated and infill patterns are constructed for both optimized-1 and optimized-2 geometries. In addition, the algorithm applies iterations of FEA and Galapagos in combination on these geometries to find the optimum distributions. Finally, three beam models are constructed and the mechanical performances of these geometries are compared. Imported values are tabulated below.

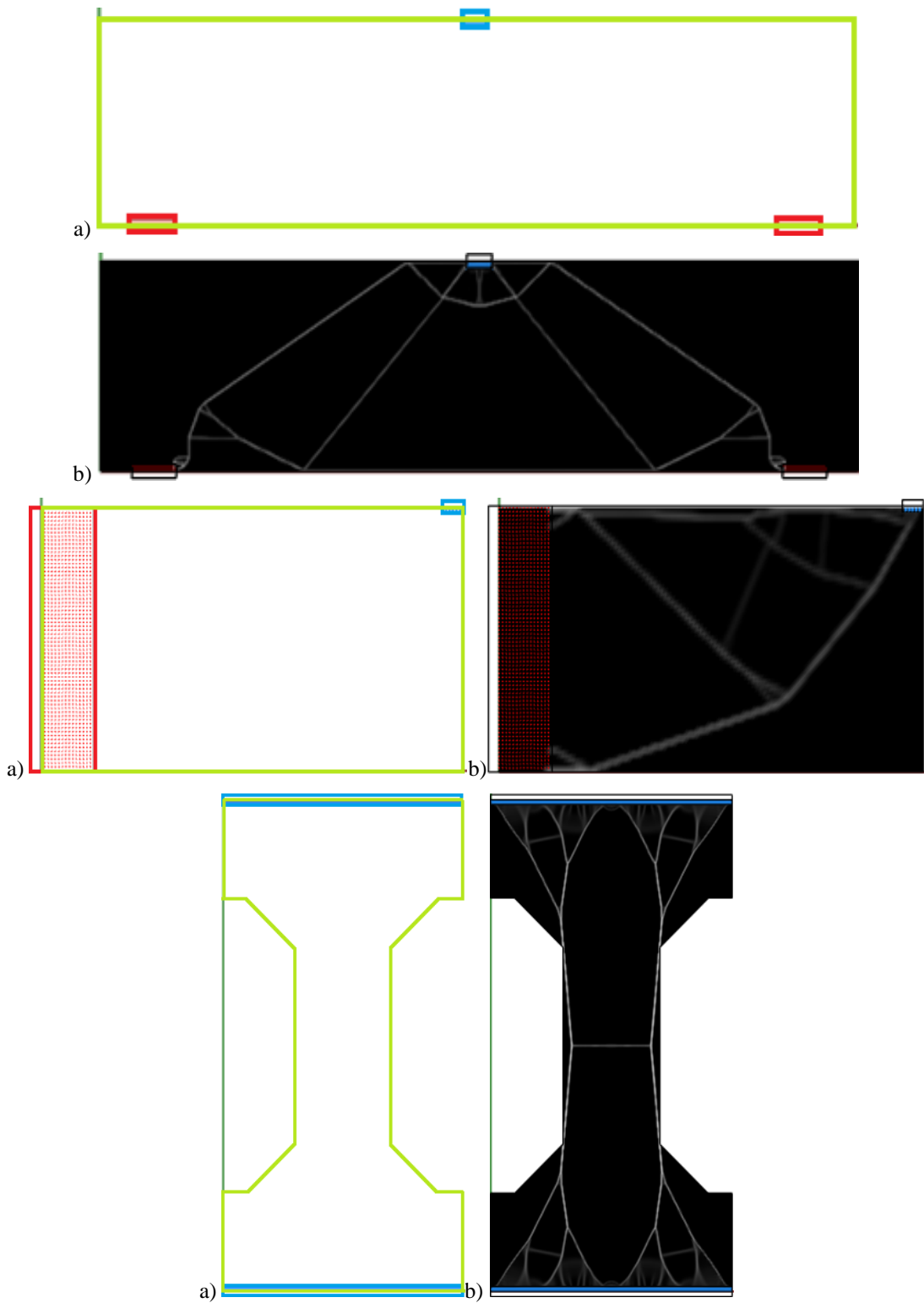


Figure 3.13. System review: (a) Support region (red), load region (blue) and boundary region (green), (b) TO result (black and white) [61].

Table 3.4. *Three-point bending beam system, dimensions of 120x30x10 mm [61].*

Stage 1			
System type	# of Voronoi seeds	Performance	Improvement (%)
Random	175	159.749	9.2
Optimized	175	145.002	
Stage 2			
System type	# of Voronoi seeds	Performance	Improvement (%)
Optimized	175	116.020	27.4

Table 3.5. *Cantilever beam system, dimensions of 80x45x10 mm [61].*

Stage 1			
System type	# of Voronoi seeds	Performance	Improvement (%)
Random	175	171.519	-27.5
Optimized	175	218.739	
Stage 2			
System type	# of Voronoi seeds	Performance	Improvement (%)
Optimized	175	139.505	18.7

Table 3.6. *Compression beam system, dimensions of 100x50x10 mm [61].*

Stage 1			
System type	# of Voronoi seeds	Performance	Improvement (%)
Random	175	189.559	13.3
Optimized	175	164.292	
Stage 2			
System type	# of Voronoi seeds	Performance	Improvement (%)
Optimized	175	122.838	35.2

Next, applying manufacturing modifications on the random and the optimized-2 geometries enables us to compare the FEA model and the cross section of the actual printable artefacts visually. It brings us to opportunity of visualizing and inspecting

the printable objects before manufacturing. Stress variations on the beam model and the cross sections of the final random and the optimized-2 geometries are shown in Figure 3.14.

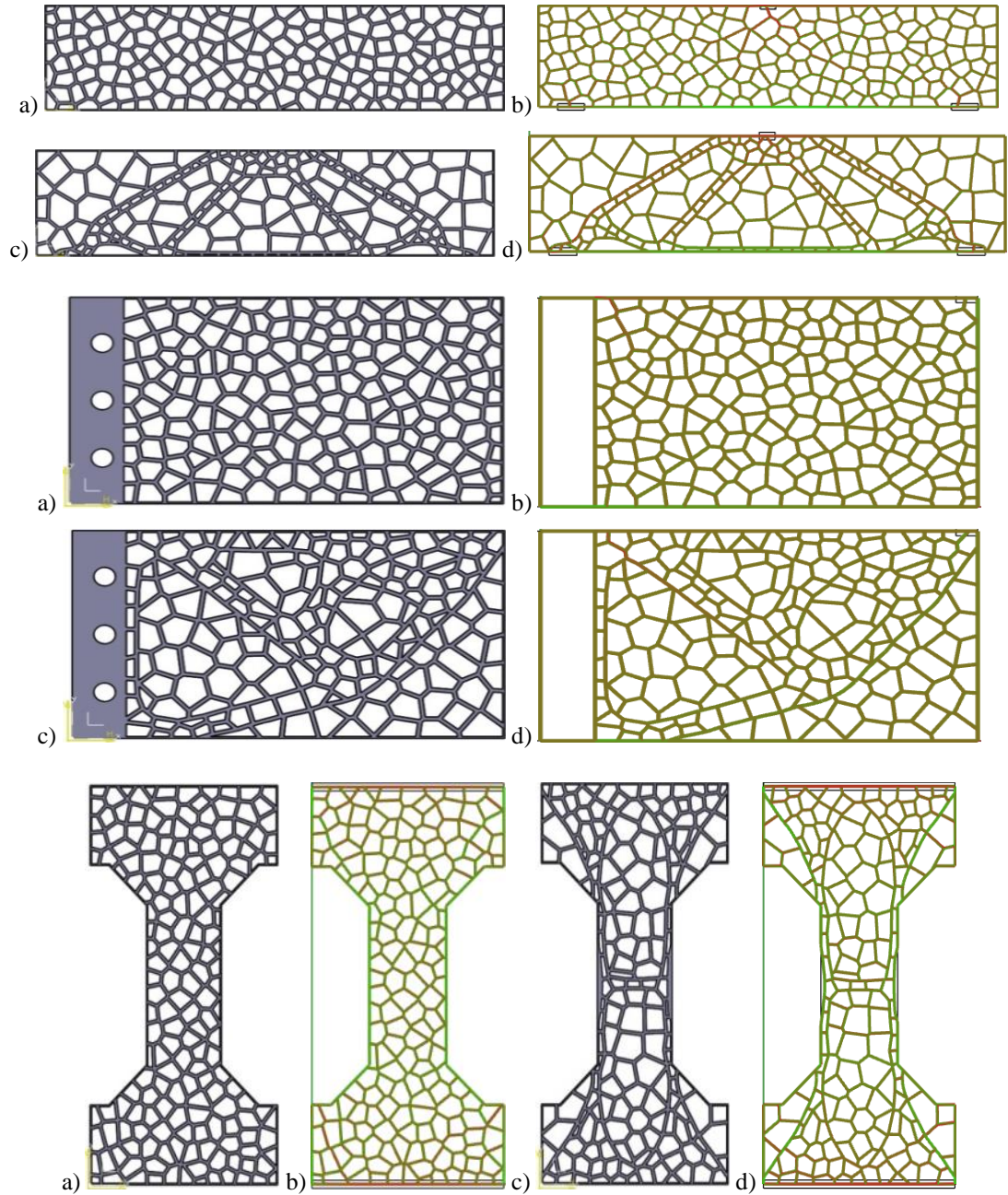


Figure 3.14. Cross sections and the beam models of the two models are given. Randomly distributed Voronoi cells are shown in (a). Ratio between axial stress in the beam elements and yield stress of the material is visualized in (b). Optimized distributions of Voronoi cells are shown in (c). Ratio between axial stress in the beam elements and yield stress of the material is visualized in (d) [61].

As it is mentioned, FEA gives the opportunity to inspect and visualize the expected deformation regimes in elastic range under loading conditions. For each case, before printing and testing the part experimentally, the deformation characteristics of beam models are considered and illustrated in figure. It is expected that random Voronoi cantilever and three-point bending beams are unable to sustain loads at the loading point and locally fails. In addition, for the random Voronoi compression beam, it is predicted that deformation behaviour of the beam is asymmetrical and 45-degree shear phenomena is the most probable failure for total collapse.

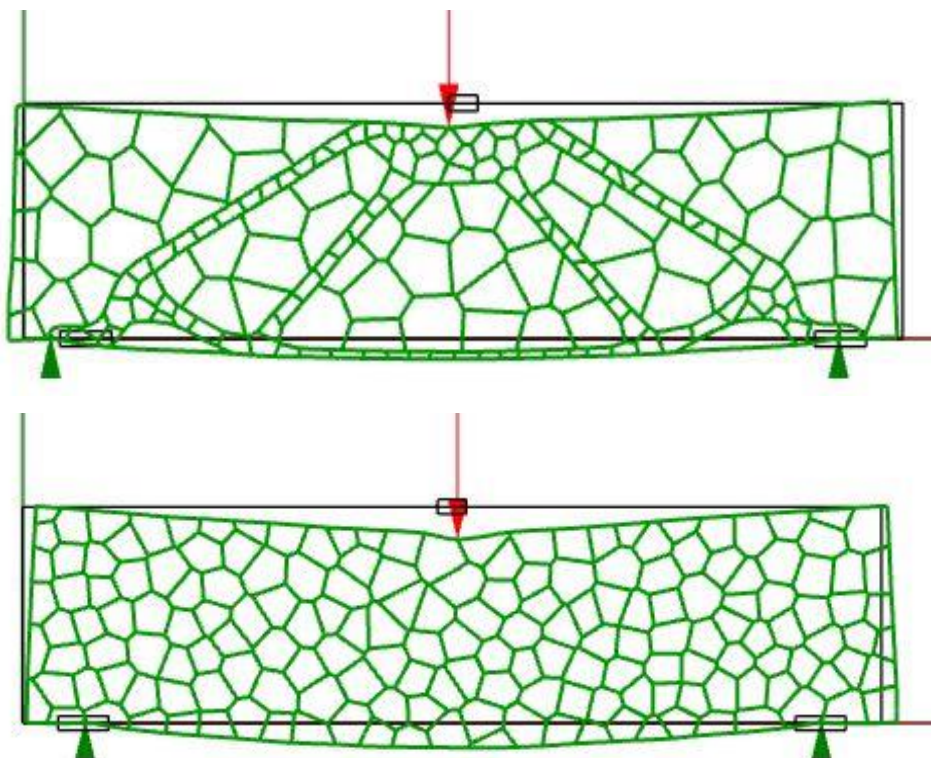


Figure 3.15. Un-deformed geometries are represented with black lines and deformed shapes of the three-point bending beam models are given, top for optimized Voronoi infills and bottom for random Voronoi infills. Local failure of three-point bending beam with random infill at the loading tip is seen.

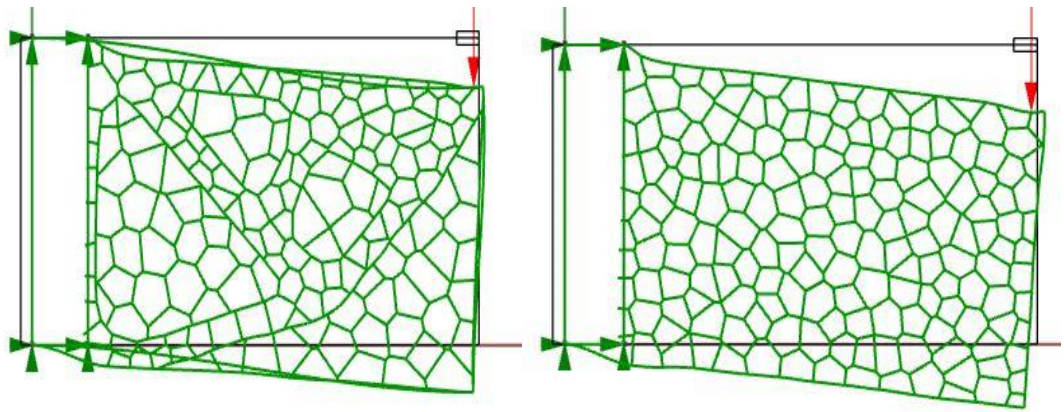


Figure 3.16. Un-deformed geometries are represented with black lines and deformed shapes of the cantilever beam models are given, left for optimized Voronoi infills and right for random Voronoi infills. Local failure of cantilever beam with random infill at the loading tip is seen.

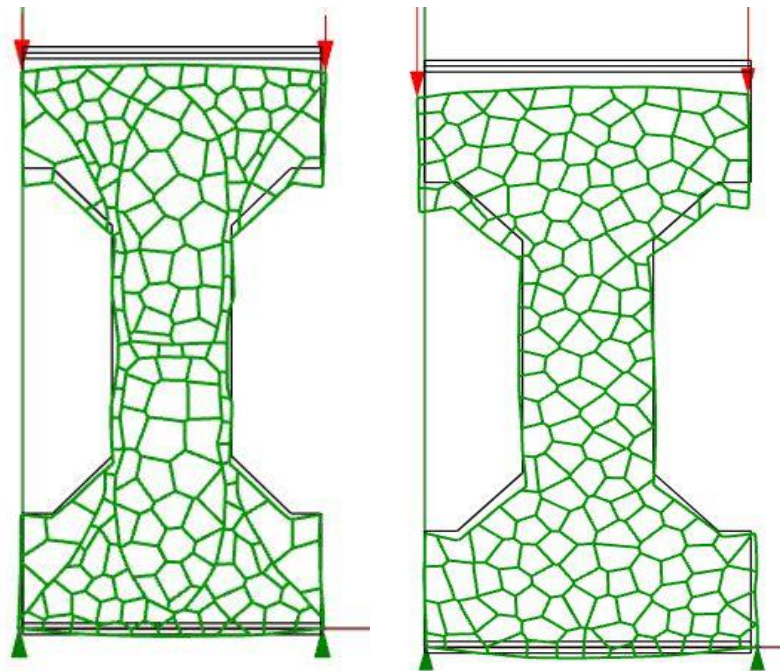


Figure 3.17. Un-deformed geometries are represented with black lines and deformed shapes of the compression beam models are given, left for optimized Voronoi infills and right for random Voronoi infills. Random compression beam model deflects more in the left side, which causes asymmetric compression.

3.3.3. Experiments

We investigated the theoretical response and the mechanical performances of the artefacts under predefined loading conditions by FEA stage of the proposed algorithm in the previous section. The random and the optimized beam models generated by the proposed algorithm for three different cases were fabricated using Fused Filament Fabrication (FFF) via an Ultimaker 3 Extended 3D printer. The dimensions of the printed artefacts are exactly same with the end models of the algorithm. The layer thickness of the artefacts is chosen as 0.2 mm and Polylactic Acid (PLA) is used as the material. The experiments were conducted on a Zwick/Roell Z020 material testing machine as shown in Figure 3.18, Figure 3.19 and Figure 3.20. All the test specimens were loaded at a cross head speed of 4mm/min, which can be considered as a quasi-static condition. For the cantilever beam and the simply supported beam, 10 mm diameter cross head tip was chosen. Each test specimen was loaded until they lost their physical integrity. Load-displacement measurements were recorded simultaneously and these curves are shown on Figure 3.21.

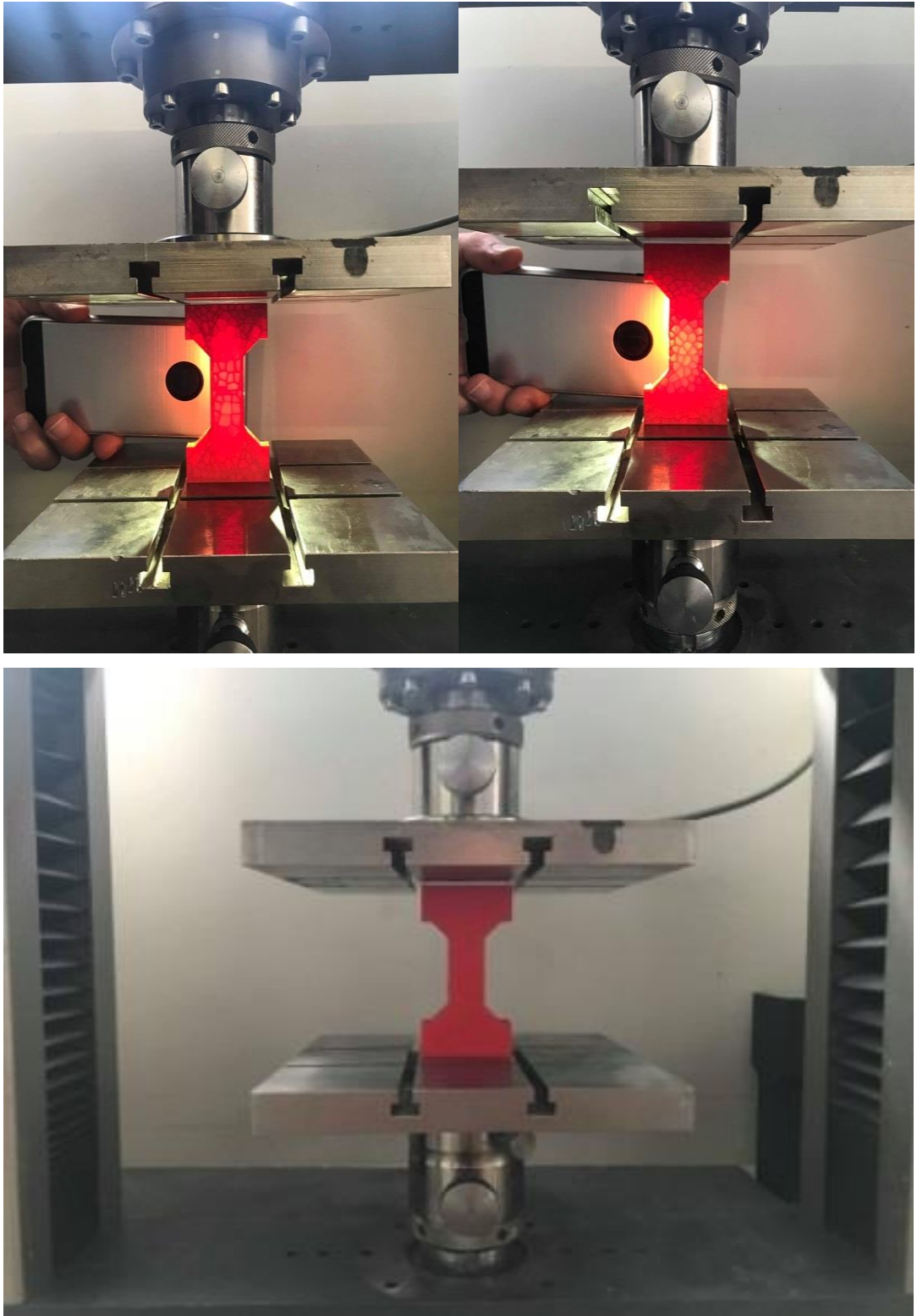


Figure 3.18. Experimental setup, random and optimized compression Voronoi beams.

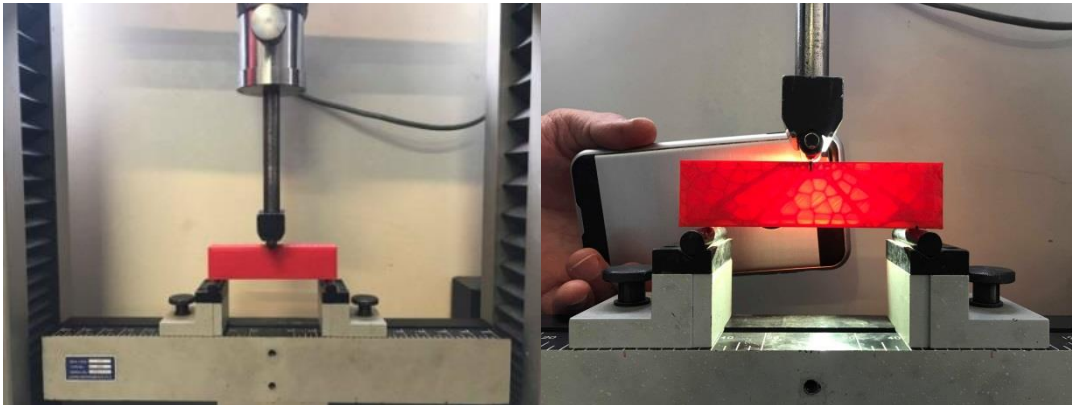


Figure 3.19. Experimental setup, optimized three point bending Voronoi beam.

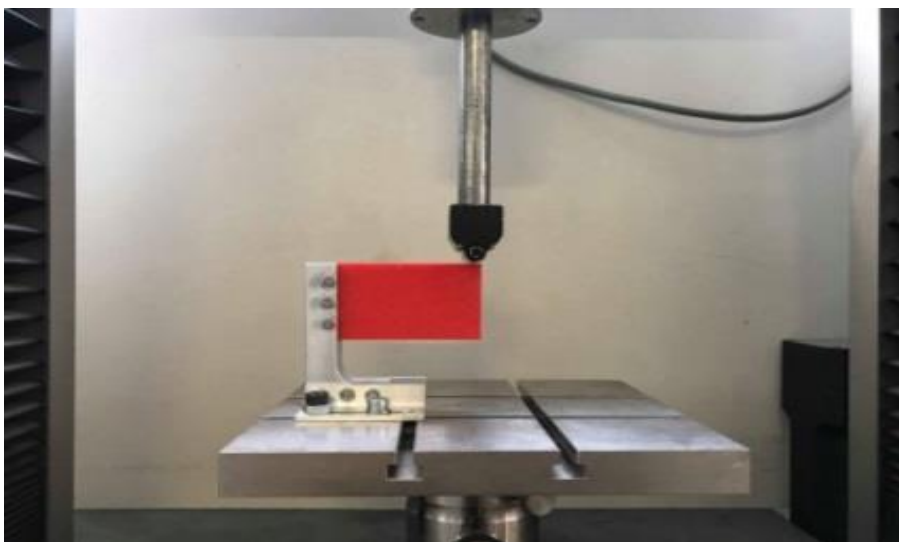
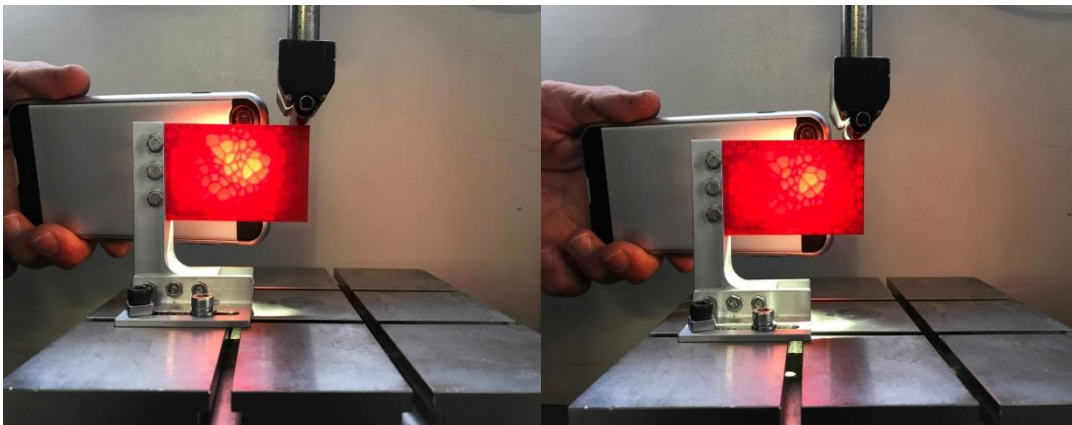


Figure 3.20. Experimental setup, random and optimized cantilever Voronoi beams.

The weights of the fabricated artefacts were measured and the plates of the testing machine were inspected and cleaned before the experiments. In addition, a fully dense three-point bending beam is printed to visualize the weight reduction, which is one of the purposes of our approach. All weight measurements are given in TABLE. The printed compression artefacts were placed separately between the flat compression plates of the testing machine with exactly in the same orientation used in TO and FEA models. For the simply supported beam case, flexural bend fixture with a diameter of 10 mm was mounted on the testing machine. The fixture was adjusted in a direction parallel to the length of the beams. Thus, the angle between cross head and the upper surface of the test specimens is set to 90°. Support and loading locations were adjusted in accordance with the 2D model measurements. Considering the cantilever case, its fixture was mounted on lower plate of the testing machine. The fixture was oriented in such a way that the cross head of the testing machine coincided with the tip of the test specimens. An additional of 10 mm fully filled regions of the test specimens were used for M4 bolt connections to achieve the fixed boundary condition.

Table 3.7. *Weight measurements of the printed beams.*

Beam Type	Model Type	Mass (gr)
Compression	Random	17.5095
	Optimized	17.5155
Cantilever	Random	21.5518
	Optimized	22.1101
Simply Supported	Random	18.3901
	Optimized	17.6106
	Fully Dense	43.5364

Figure 3.21 shows the load displacement curves of the random and the optimized models under the downward crosshead movement. The measured weights, the maximum loads and the displacement values of the test specimens are summarized in the following table.

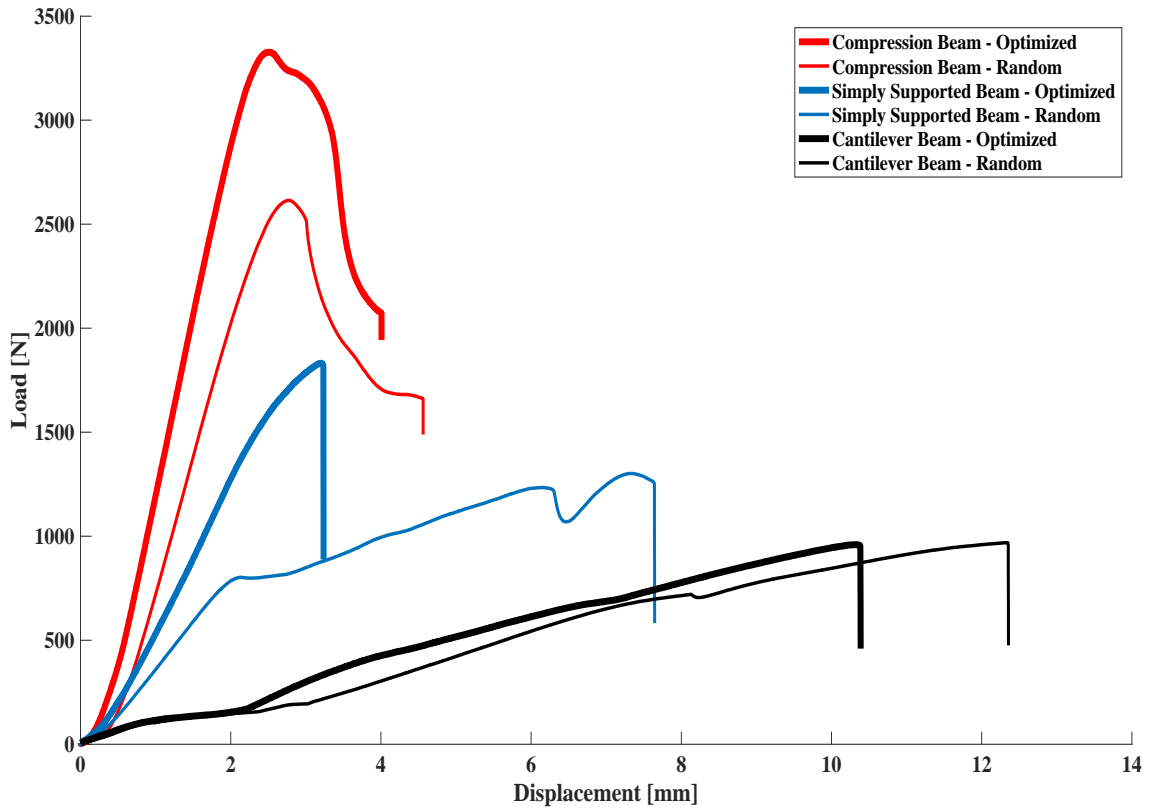


Figure 3.21. Load-displacement curves of the test specimens. Red lines represent compression beams, blues are for simply supported beams and blacks are for cantilever beams while thinner ones for random Voronoi and thicker ones are for optimized Voronoi infills [61].

Table 3.8. Results of the tests [61].

Beam Type	Model Type	Mass (gr)	Max. Load (N)	Max. Displacement (mm)
Compression	Random	17.5095	2614.15	2.7687
	Optimized	17.5155	3326.46	2.5140
Simply Supported	Random	18.3901	1301.45	7.3332
	Optimized	17.6106	1831.24	3.2041
Cantilever	Random	21.5518	968.98	12.3440
	Optimized	22.1101	959.21	10.3186

In the proposed algorithm, each Voronoi beam model is subjected to the same amount of loading, which enables us compare the performance of the parts. In order to correlate the results of the experiments with the FEA results we chose limit loads for both models from the experimental results and used these values in our performance equation. Thus, for the compression and the simply supported beam cases, the maximum load capacities of the random beam models are set as a limit load. For the cantilever beam case, the maximum load capacity of the optimized beam model is set as a limit load. Deflections values are recorded at these limit loads. Performance comparisons of the algorithm and the experiment are presented in the following table.

Table 3.9. *Properties of the models at the limit loads [61].*

Beam Type	Limit Load (N)	Model Type	Displacement at Limit Load (mm)	Performance Improved w.r.t. Experiments (%)	Performance Improved w.r.t. Analysis (%)
Compression	2614	Random	2.7687	33.9	35.2
		Optimized	1.8303		
Simply Supported	1301	Random	7.3332	73.4	27.4
		Optimized	2.0361		
Cantilever	959	Random	12.005	11.8	18.7
		Optimized	10.319		

Similar to analytical correlation, visual failures of tested beams are compared with estimated FEA deformation regimes for further correlation. Although FEA deformations are simulated in the elastic range for each beam, experimental collapses are found in accordance with the expected formations. Figure 3.22 represents the failed artefacts.

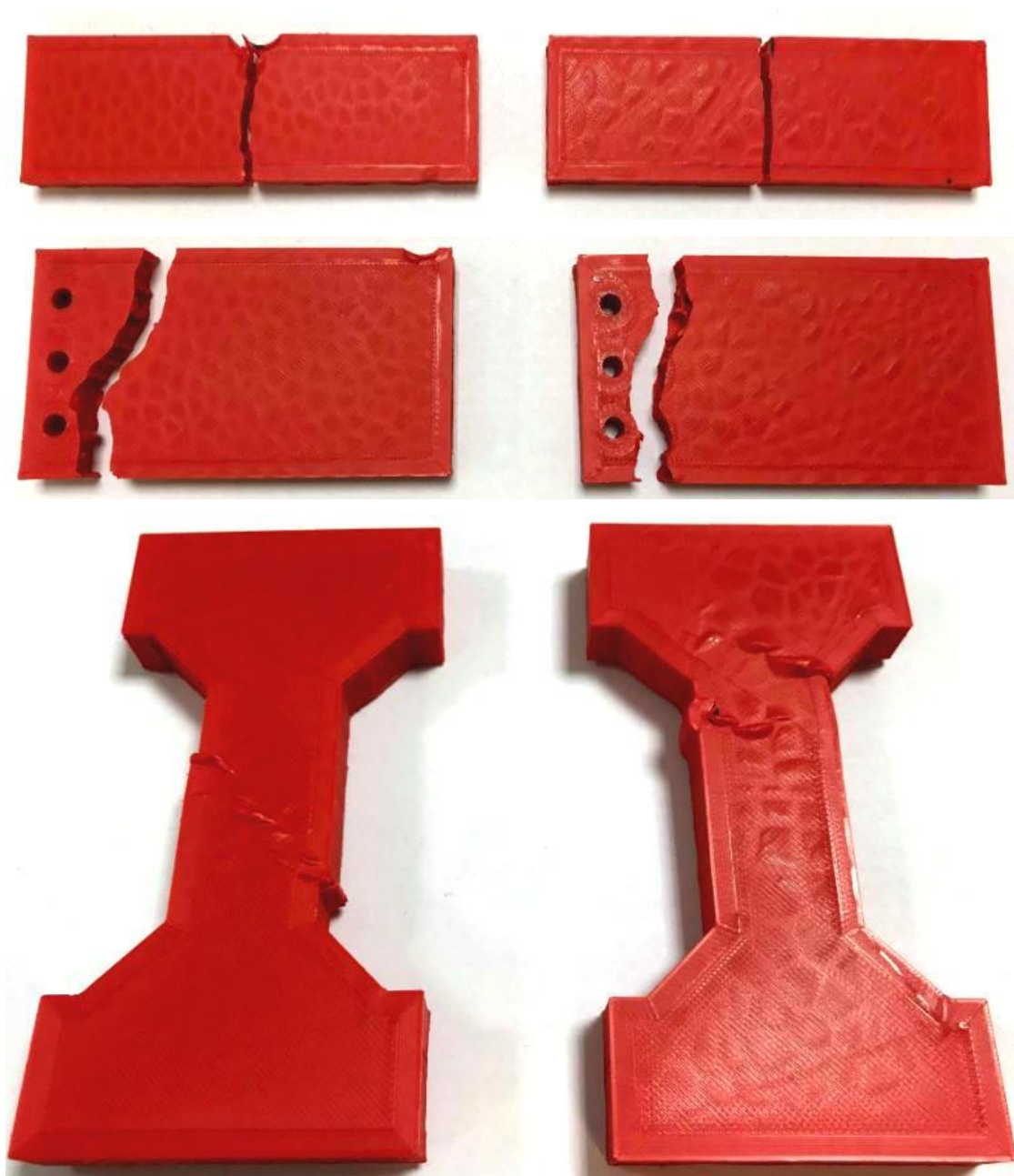


Figure 3.22. Failed artefacts, left column shows the random Voronoi infill artefacts, whereas; right column represents optimized Voronoi infill models. Local deformations are clearly seen in simply supported beam (top) and cantilever beam (middle) at the position of cross-head tip. 45-degree shear failure phenomenon is also found at the neck of compression beam with random Voronoi pattern (below). Dimensions of simply supported beams are 120x30x10 mm, cantilever beam are 80x45x10 and compression beam are 100x50x10 m.

Lastly, random and optimized Voronoi systems are compared experimentally with regular infill systems. For this purpose, each beam models are printed by applying

regular linear infill pattern with the same printing material. In order to make a fair comparison, the geometrical dimensions of compression, 3-point bending and cantilever beams are kept the same with the Voronoi beam models. Furthermore, volume fractions of regular beam models are arranged in such a way that mass of them are kept close to the weights of the Voronoi systems. Thus, a realistic strength-to-weight ratio comparison is achieved. Below, mass of the printed artefacts are tabulated and compared with the Voronoi systems.

Table 3.10. *Weights of the printed artefacts.*

Type of Beam	Type of Infill	Mass (gr)
3-Point Bending	Random Voronoi	18.3901
	Optimized Voronoi	17.6106
	Regular Infill	17.5223
Cantilever Beam	Random Voronoi	21.5518
	Optimized Voronoi	22.1101
	Regular Infill	21.2427
Compression Beam	Random Voronoi	17.5095
	Optimized Voronoi	17.5155
	Regular Infill	17.0585

Experimental setups are adjusted in an identical way and tests are repeated for the regular linear infill models. Figure 3.23, Figure 3.24 and Figure 3.25 show additional load displacement curves of the regular infill models under the downward crosshead movement. The measured maximum loads and the displacement values of the test specimens are summarized in the following tables.

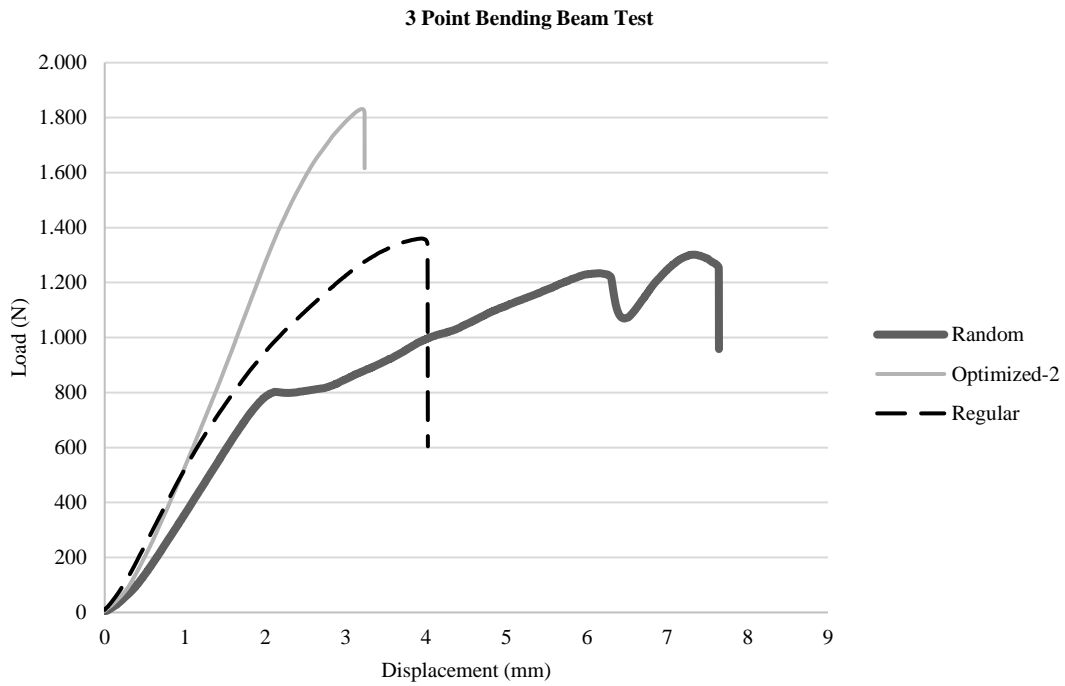


Figure 3.23. Load-displacement curves of the 3-point-bending beam test specimens.

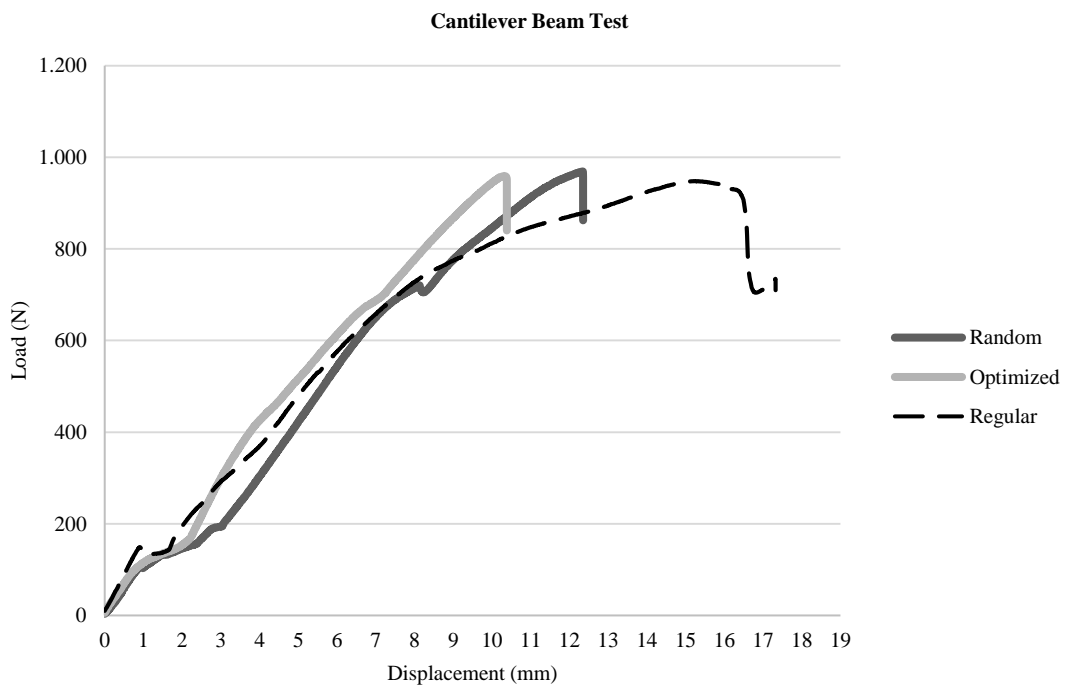


Figure 3.24. Load-displacement curves of the cantilever beam test specimens.

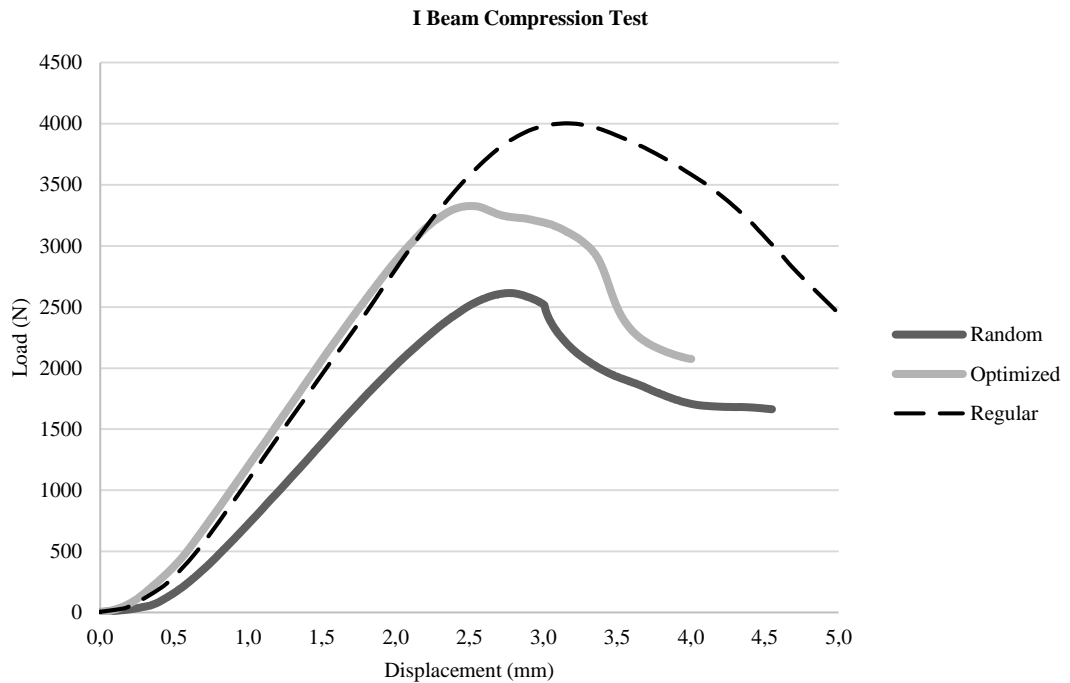


Figure 3.25. Load-displacement curves of the compression beam test specimens.

Table 3.11. Results of the tests.

Beam Type	Model Type	Mass (gr)	Max. Load (N)	Max. Displacement (mm)
Compression	Random	17.5095	2614.15	2.7687
	Optimized	17.5155	3326.46	2.5140
	Regular	17.0585	4003.39	3.1544
Simply Supported	Random	18.3901	1301.45	7.3332
	Optimized	17.6106	1831.24	3.2041
	Regular	17.5223	1360.24	3.9399
Cantilever	Random	21.5518	968.98	12.3440
	Optimized	22.1101	959.21	10.3186
	Regular	21.2427	948.01	15.2347

To compare and evaluate the mechanical stiffness of the printed artefacts, limit load approach is again applied onto experimental results. The limit loads of simply supported and compression beams are kept constant, whereas; limit load of the

cantilever beam is lowered since regular infill exhibits failure in low level of loading. Thus, for the comparison, limit load of the cantilever beam is set to 948 N.

Table 3.12. *Properties of the models at the limit loads.*

Beam Type	Limit Load (N)	Model Type	Displacement at Limit Load (mm)	Performance of Regular w.r.t. Random (%)	Performance of Optimized w.r.t. Regular (%)
Compression	2614	Random	2.7687		
		Optimized	1.8303	31.7	3,20
		Regular	1.8903		
Simply Supported	1301	Random	7.3332		
		Optimized	2.0361	54.0	39,6
		Regular	3.3732		
Cantilever	948	Random	11.692		
		Optimized	10.057	-30,3	33,9
		Regular	15.235		

In order to make the correlation between regular, random and optimized models more standardized, mechanical response of them are inspected in linear region of the stress-displacement curves. To do so, common regions in which each infill type linearly behaves are selected. For each test case, these regions are illustrated in Figure 3.26, Figure 3.27 and Figure 3.28.

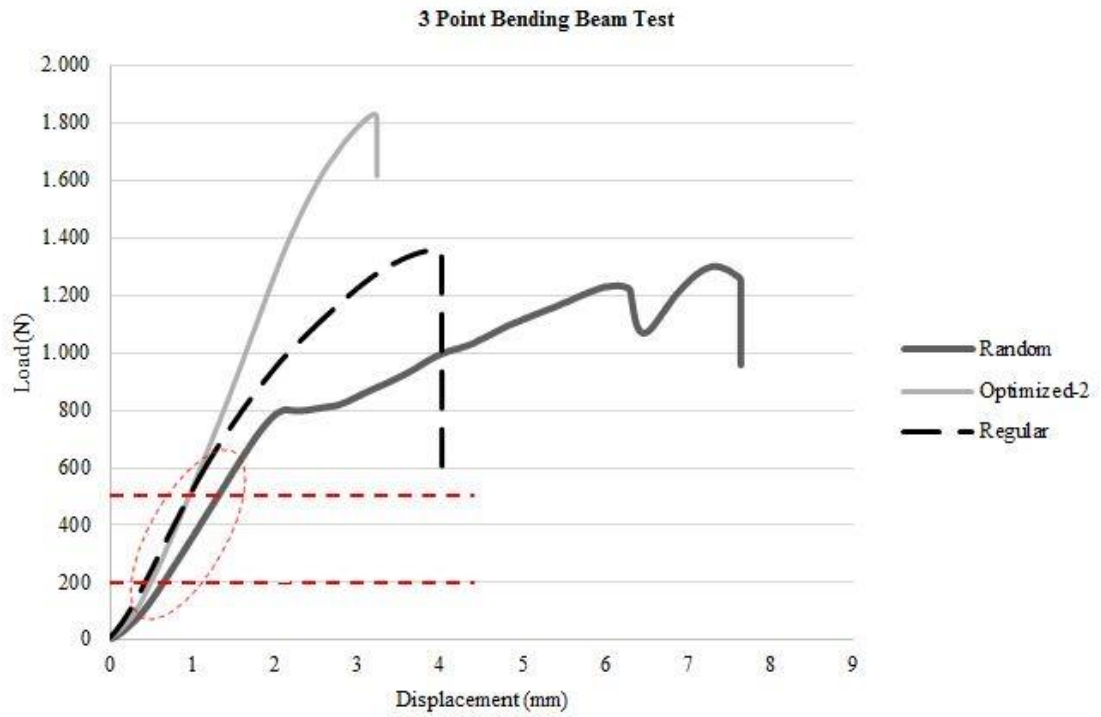


Figure 3.26. Linear region for 3-point-bending beam test specimens.

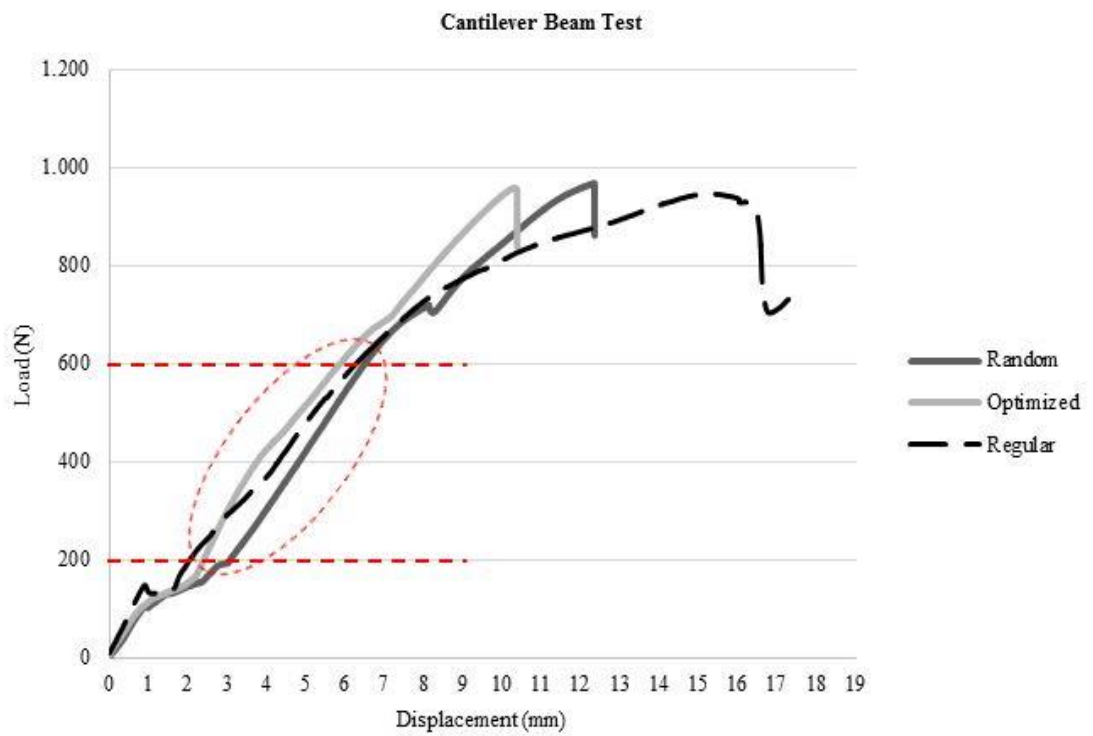


Figure 3.27. Linear region for cantilever beam test specimens.

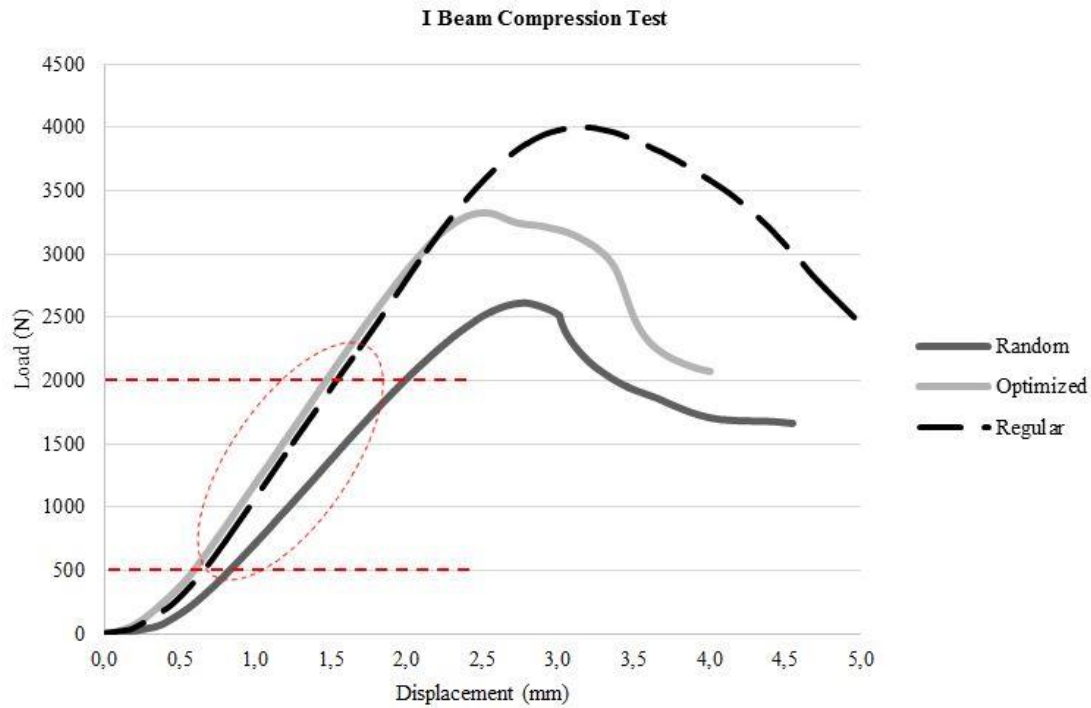


Figure 3.28. Linear region for compression beam test specimens.

Then, for each test case, lower and upper limit loads of the regions are defined and tabulated. Displacement values at these load levels are noted. Slope of linear curves are calculated and tabulated below.

Table 3.13. Properties of the models at the limit loads.

Beam Type	Model Type	Lower Limit Load (N)	Displacement at Lower Limit Load (mm)	Upper Limit Load (N)	Displacement at Upper Limit Load (mm)	Slope (N/mm)
Compression	Random		0.8252		1.9825	1296.1
	Optimized	500	0.5886	2000	1.4635	1714.6
	Regular		0.6555		1.5322	1710.9
Simply Supported	Random		0.6478		1.3072	454.9
	Optimized	200	0.4941	500	0.9555	650.3
	Regular		0.4219		0.9565	561.2
Cantilever	Random		3.0709		6.5001	116.6
	Optimized	200	2.4014	600	5.8667	115.4
	Regular		2.0521		6.2761	94.7

According to numerical results in linear region, each optimized Voronoi system is stiffer than random and regular counterparts. However, compression beam tests show that regular infill pattern significantly carries more weight than the optimized infill does. It is also seen that the mechanical responses of random and optimized Voronoi infills are similar to the cantilever beam case.

Tested regular infill artefacts are inspected. Similar to cantilever and simply supported beams with random Voronoi pattern, regular infills of the same models locally deformed under loading condition at the position of the cross-head tip of the experimental device. Furthermore, I beam with regular infill pattern spontaneously bends from straight to curved at the narrow neck under the compressive loading. Experimental scenes and deformed forms of the regular infill beam models are shown in Figure 3.29, Figure 3.30 and Figure 3.31.

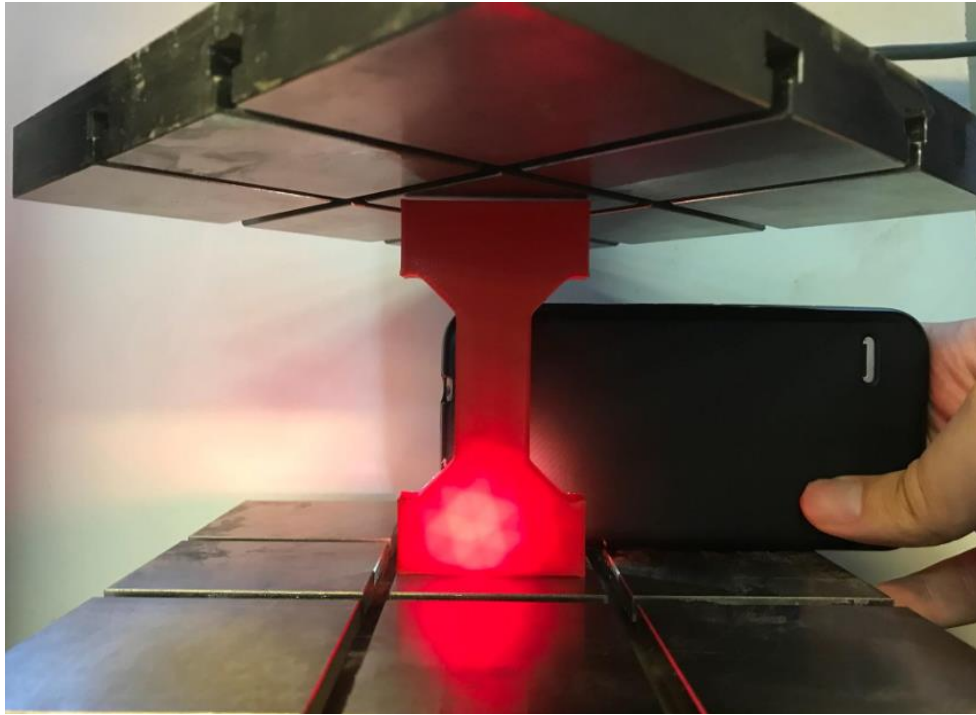


Figure 3.29. Experimental setup of the compression beam with regular infill (top). Buckled compression beam top and side views (bottom). Buckling is seen at the narrow neck of the beam.

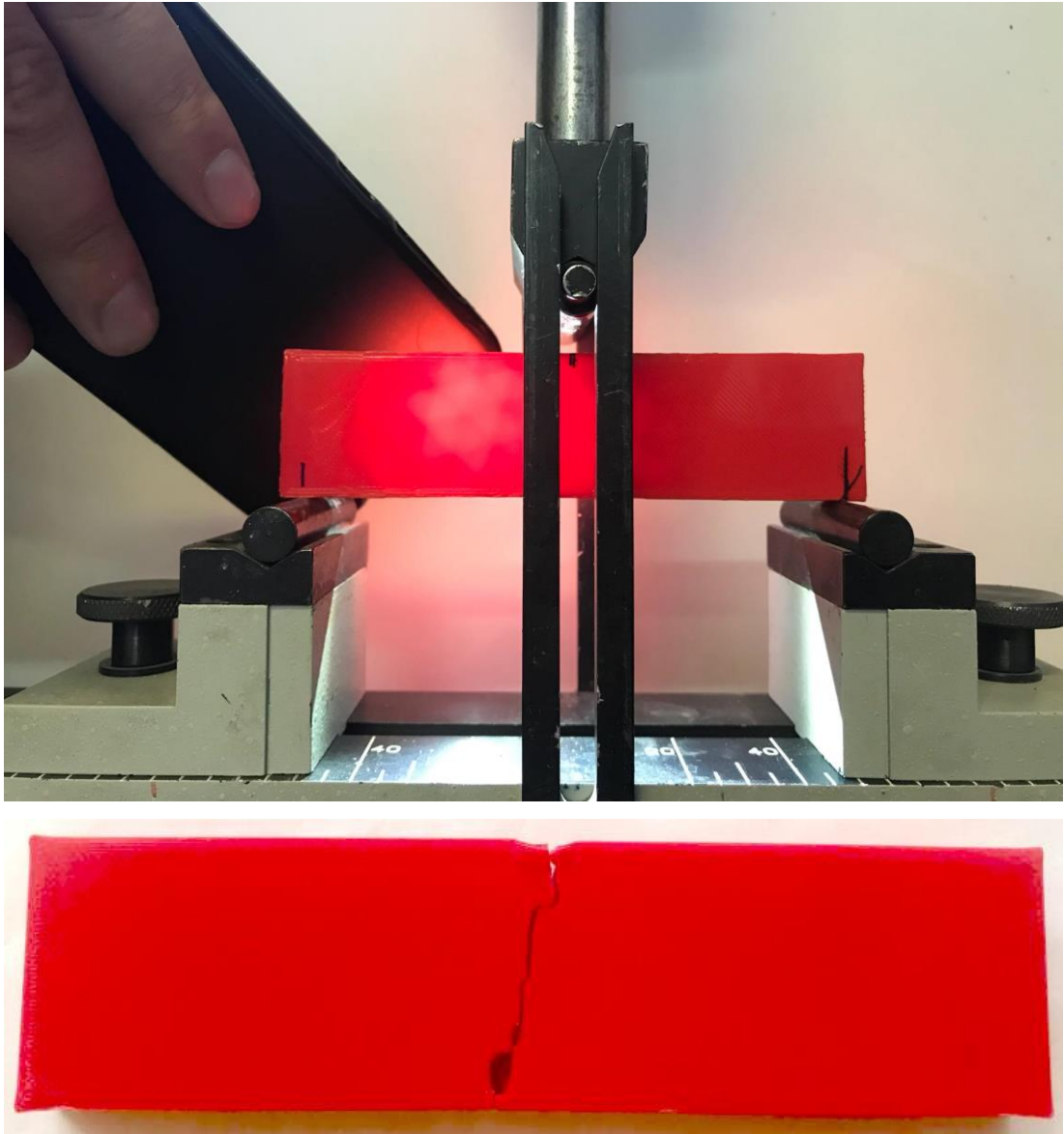


Figure 3.30. Experimental setup of the simply supported beam with regular infill (top). Local deformation and failed view (bottom). Local deformation is seen at the middle top of the beam.

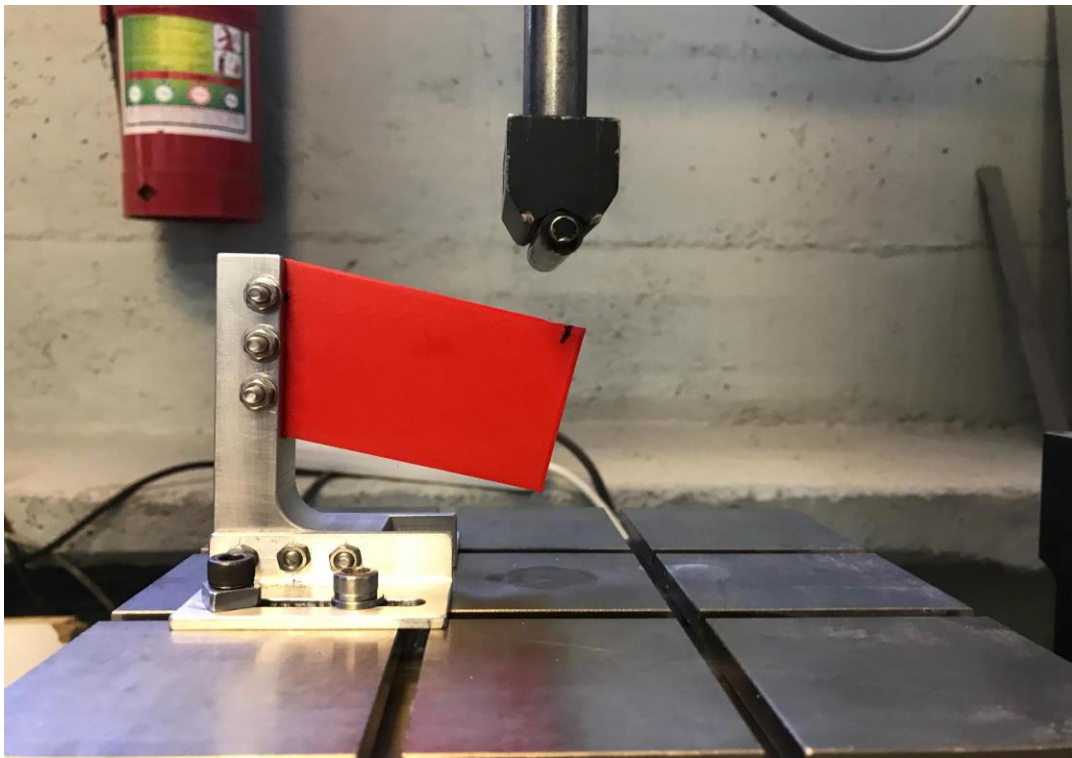
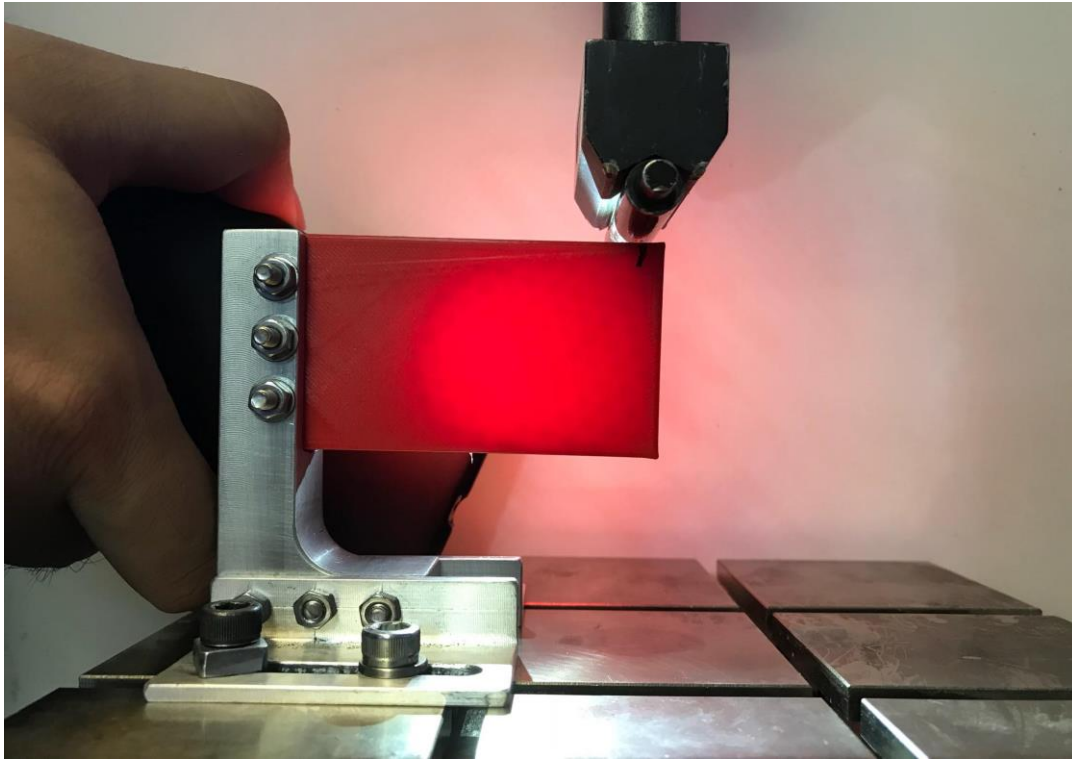


Figure 3.31. Experimental setup of the cantilever beam with regular infill (top). Local deformation and failed view (bottom). Local deformations are seen at the tip and bolted portions of the beam.

3.3.4. Limitations of Auto 2.5D Test and Possible Future Directions

This chapter presented a novel method of combining TO and FEA methodologies with AM to construct naturally inspired Voronoi infill patterns. Under the specific load and support conditions, TO determines the critical regions within the structure and the algorithm populates Voronoi seeds in accordance with the design requirements. Then, FEA is performed on the generated geometries and the genetic algorithm finds the optimum result for better mechanical performances. The method is employed on three different test scenarios to reveal the flexibility of the approach. Performance of the proposed scheme is elaborated through the test results and the analysis. The results indicate that the method is applicable for generating optimized Voronoi infill patterns in a given geometry. Overall, the optimized Voronoi infill pattern exhibited higher mechanical performance than the random Voronoi infill patterns.

Regarding the future works, the same methodology can also be employed on the 3D models to improve their specific properties. In such an approach, instead of using beam elements in the analysis, shell structures should be utilized to decrease the computation times. In addition, PLA which is used as printing material can be defined into material library of Karamba 3D for FEA applications to obtain accurate analytical results and FEA part of the algorithm can be improved in such a way that plastic regime of the PLA material can be simulated. Thus, more accurate correlation can be built between FEA results and experimental results. Furthermore, proposed algorithm can be enhanced to gain full control on the amount of Voronoi seeds in high and low density regions rather than defining 100 of them into effective and 75 of them in low density regions. Therefore, genetic algorithm can work on both the number and the positions of the Voronoi seeds and it can gain full access on optimization to generate optimum Voronoi infill geometries. Also, several random Voronoi infills should be tested numerically to find a domain that reflects the range of mechanical performance in terms of deflection amount. Since, each random distribution significantly affects the mechanical behaviour and amount of deflection and thus, overall stiffness of the system, it is necessary to test several of them and additionally to compare these results

with optimized Voronoi infills. As a result, the maximum expected efficiency of the proposed approach can be simulated more effectively. Additionally, performance formula which is fed into evolutionary algorithm should be enhanced. Since the multiplication of total mass and maximum deflection values is defined as our formula, the contribution of each value to overall performance is not tracked. One of the suitable solutions for this problem might be normalization of our formula. We may also discard the mass value from the formula and only choose the maximum deflection since the change in the positions of Voronoi seeds does not affect the overall mass significantly, as long as their amount is constant.

Lastly, experimental setup is needed to be enhanced in such a way that boundary conditions defined in the proposed systems and analytical procedures should be totally reflected on the experiments. A problematic case is observed within the cantilever beam model. At the first stage of the experiments, cantilever beams are mounted on a test fixture in order to fix the beams at the left-hand side, which is the case in analytical FEA model. First test fixture of the cantilever system holds the beam artefact by creating tight fitting connection and is given in Figure 3.32. However, it is experienced that grip force between the fixture and beam is insufficient to maintain the artefact under high level of tip loads. Furthermore, the intersection between bottom part of the beam and end wall of the test fixture causes line shearing during increased loading. Since, the expected loading condition is not shearing in the mount region; second test fixture is designed to eliminate this incident. Rather than physically gripping the left side of the cantilever beam, a number of bolted joints are added to system. Second test fixture is also seen in Figure 3.32. Still, bolted connections are failed to keep the beams in fixed position. The reason for this is the material properties of the PLA. Compared to resistance of steel screws, PLA exhibits plastic deformation under higher loadings and screws plastically deform the PLA around the bolting regions. Thus, slot type holes are created by screws, local deformations are observed and cantilever beam starts to rotate around the first top screw. Local deformation of cantilever beam around

the first hole is also seen in Figure 3.32. To eliminate this limitation, second row of bolted joints should be implemented into cantilever beam models.

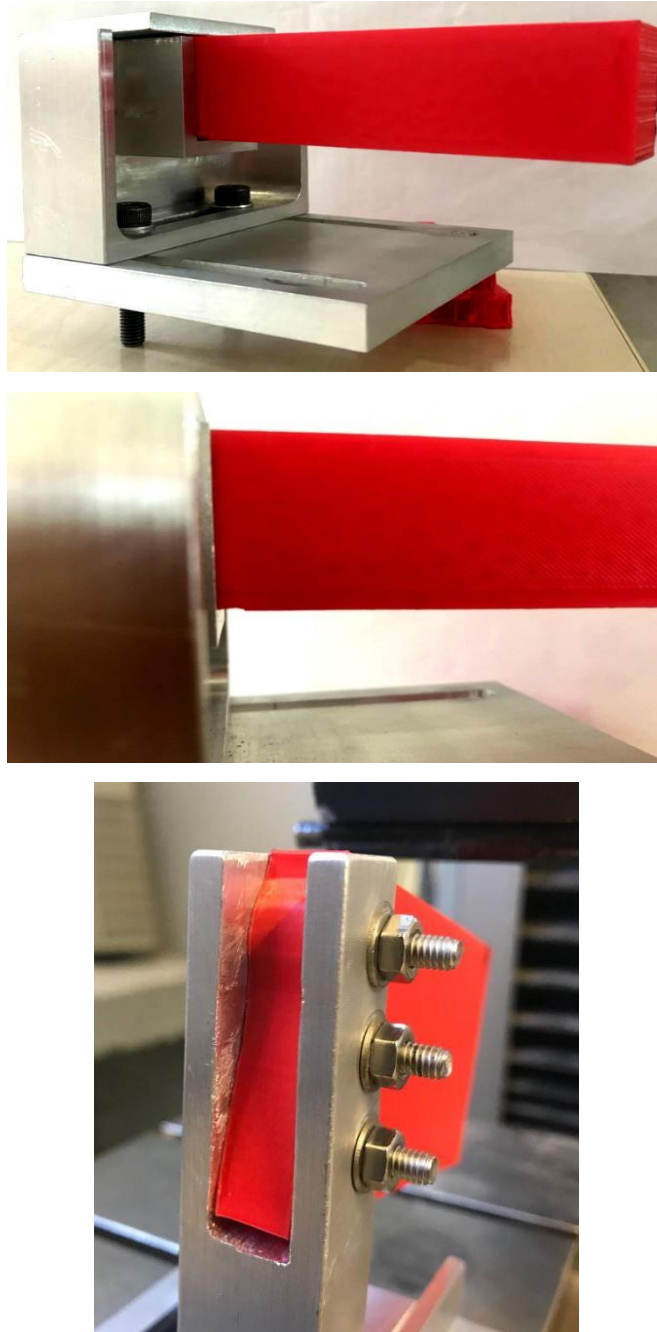


Figure 3.32. First experimental fixture of the cantilever beam and tight-fitting boundary condition (top), shear deformation between printed artefact and test fixture (middle), revised fixture, plastic deformation and rotation around first bolt joint (bottom).

CHAPTER 4

METHODOLOGY 3D

4.1. Introduction

This section focuses on 3D models with the same approach that is presented in the second half of the third section. In this chapter, 3D models are internally modified by Voronoi patterns to demonstrate superior mechanical behaviors under pre-defined loading conditions. Similarly, a closed design volume firstly undergoes TO process to reveal the principal stress, Von-Misses stress and deflection distribution under pre-defined loading conditions. Once these three regions are obtained within the 3D model, it is smoothly separated from the original model. Secondly, Voronoi cells are generated in accordance with the TO results in such a way that material, in this case Voronoi cell walls, is distributed among these regions to simulate the material distribution. Thus, critical regions are constructed by populating more Voronoi cells compared to remaining volume. In other words, critical regions are filled with closely packed Voronoi cells to increase the material amount.

The current chapter is organized as follows. Following this introductory part, the proposed automatic approach and the test cases are introduced. Then, conclusion of the study and possible future works are given.

4.2. Proposed Approach and Test Cases

The main objective of the algorithm is to construct a 3D Voronoi pattern that minimizes the maximum deflection of the part compared to the randomly distributed Voronoi cells pattern. For this purpose, design volume and load-support regions are firstly defined in Rhinoceros 6 – Grasshopper environment in ‘.stp’ format as boundary region, load region and support region respectively, subjected to TO and then seeding part of the algorithm constructs the final geometry. At the FEA works on

these geometries and genetic multi-objective algorithm iterates through the possible solutions to obtain the most efficient geometry. The general flow chart and main aspects of the algorithm are similar to previous work and shown in Figure 3.9.

Our algorithm creates two different Voronoi infill patterns which are namely fully random Voronoi distribution and optimized Voronoi distribution. Regarding the first one, the algorithm populates all seeds on restricting boundary region without any further limitation and generates random Voronoi infill pattern within 25 different seeding possibilities. For the second case, the algorithm uses the results of TO to create the additional boundary regions and populates seeds both on these regions and remaining of the boundary region. A number of stages add complexity to the algorithm. However, the work is led through the autonomous path until the end use models are obtained. Additionally, the application of TO at the very beginning enables the algorithm to produce optimum results. All input variables are the same for these two approaches.

For the optimized system boundary, load and support regions are firstly defined in Grasshopper, a Rhino plug-in [54]. Then, the related load-support types are given by the user. These variables are combined with Millipede inputs that are target density (0.4), system resolution (0.5 mm spaced nodes in x direction) and number of iterations [55]. Output is topologically optimized mesh geometries which are represented as three colour visualizations of principal stress, Von-Mises stress and deflection distributions. For these three different distributions, each node is split into its ARGB channels and user defined value is set for gathering the critical nodes. We chose 0.6 for these operations which can be explained as the most critical nodes are the 40 % of the total nodes. Once the important nodes are captured, meshes that own those nodes are extracted from the boundary region and as a result, mechanically the most important parts of the boundary region are constructed. After that, the user inputs the total number of Voronoi sites which is 50 for this study and the algorithm randomly populates some of these points on critical regions and the remaining of them on boundary region within 10 possible random seeding distributions. This number is later

fed into the genetic algorithm to find optimum locations of the seeds. At this point, we also define a ratio that determines the amount of Voronoi seeds on critical regions or boundary region. The resolution of this ratio is 5 Voronoi seeds. This ratio is also later fed into genetic algorithm for finding optimum amount of Voronoi seeds in related regions. Thus, for 3D part of the study, we get both the number and position freedom of generating Voronoi seeds. Higher amount of seeds on critical regions result in more closely packed Voronoi cells where there will be more deployed material during the fabrication. This improves the performance of artefacts under the loading conditions. Figure 4.1 illustrates the mechanism for the Bunny-Back compression model.

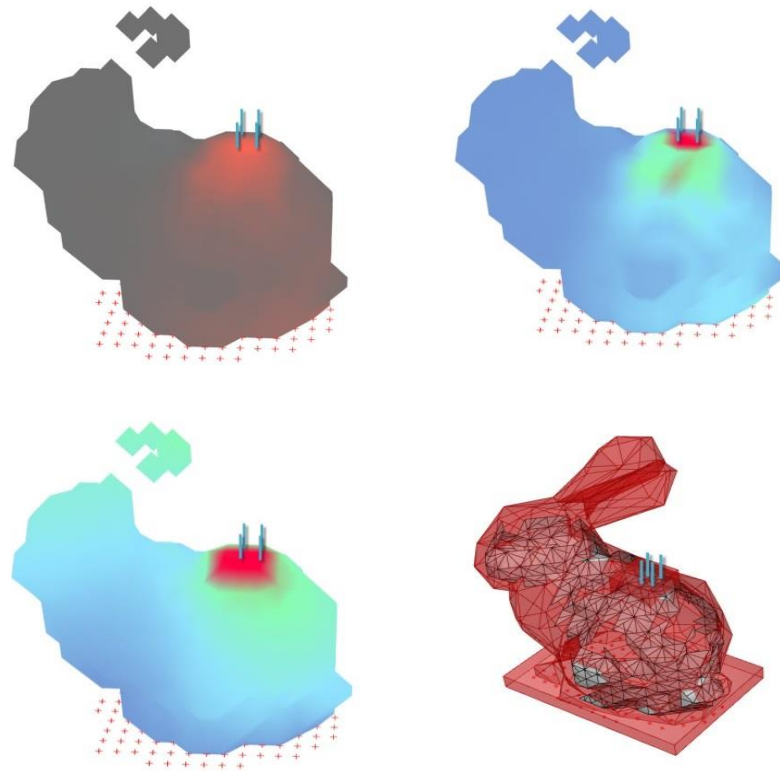


Figure 4.1. Bunny-Back compression model, Bunny model is loaded from the back of it (blue lines) and supported from the bottom (red dots). After TO, principal stress distribution (top left), Von-Misses distribution (top right) and deflection visualization (bottom left) is obtained. Critical mesh nodes are captured in bottom right.

As it is mentioned, the algorithm creates randomly distributed geometry which has exactly the same boundary region. Finally, two 3D models with different infill patterns

are obtained with the same number of sites. These models are then defined into the first FEA stage. Karamba3D is also a plug in for Grasshopper, performing FEA in 3D environment [56]. Resultant 3D models are meshed using planar shell elements with the size of 0.5 mm at most, because of the fact that Voronoi site walls are represented by surface shells in 3D. Support / load locations and types and material are defined exactly the same for the random and optimized models. It is important to note that the defined material in FEA is not PLA which is used for 3D printing the models. The default material library of Karamba3D does not have mechanical properties of PLA material, aluminum is chosen for simplicity. Another important issue is that our models in Rhino 6, Grasshopper and Millipede environments are represented in millimeter and Newton, whereas; Karamba3D gets its inputs in meter and kilo-Newtons. Since we are trying to obtain an automated algorithm, we have to use these four software simultaneously. It is reasonably fine to consider the changes in the maximum deflection results as percentages in order to compare the variations between the 3D models. Average and maximum stress values of 3D models guide us for future experimental results. We may also guess the failed geometries since we can visualize the deflected 3D models in Karamba3D.

Since site locations are randomly chosen by Grasshopper, we may get thousands of different infill geometries and FEA results. Thus, an efficient tool of Grasshopper, Galapagos, an evolutionary problem solver is included at the end of the algorithm [57]. Among thousands of possible Voronoi infill patterns Galapagos determines the optimum ones for the two algorithms. Briefly, Galapagos employs a kind of trial and error method to get the optimum result for the defined design criteria. The inputs (random seed locations and numbers) are defined as genes and the results are defined as the genomes which are performance values coming from the FEA. The initial step of Galapagos is about populating these genomes resulted by the combinations of the genes. It is reasonable to assume that genomes having lower performance values are potentially closer to the optimum result. Thus, Galapagos removes the genomes with higher values and moves on with the lower valued genomes and their genes in the next

iteration. Last part of the algorithm is about obtaining the manifold artefacts. For this purpose, random and iterated geometries undergo manufacturing modifications. It is important to remember that the main objective of the study is to determine the optimum Voronoi infill pattern and compare it with the random one to observe the effects of interior structure on the mechanical performance. Thus, for Voronoi shells, we choose 0.8 mm constant wall thickness. Also, we employed another manufacturing modification that enables us to decompose the support material that is deployed during printing into the interior of the 3D model. For this purpose, close-shell model is subjected to Catmull-Clark subdivision by setting the number of subdividing iterations for each face as 3 [58]. Thus, 3rd degree continuous curvature-type of spongy shell model is obtained. Last manufacturing modification is adding the load and support regions for stability during the experiments. External geometries of the artefacts are kept consistent with the design requirements while decreasing the material consumption. The manufacturing modifications of Bunny-Head model are illustrated in Figure 4.2.

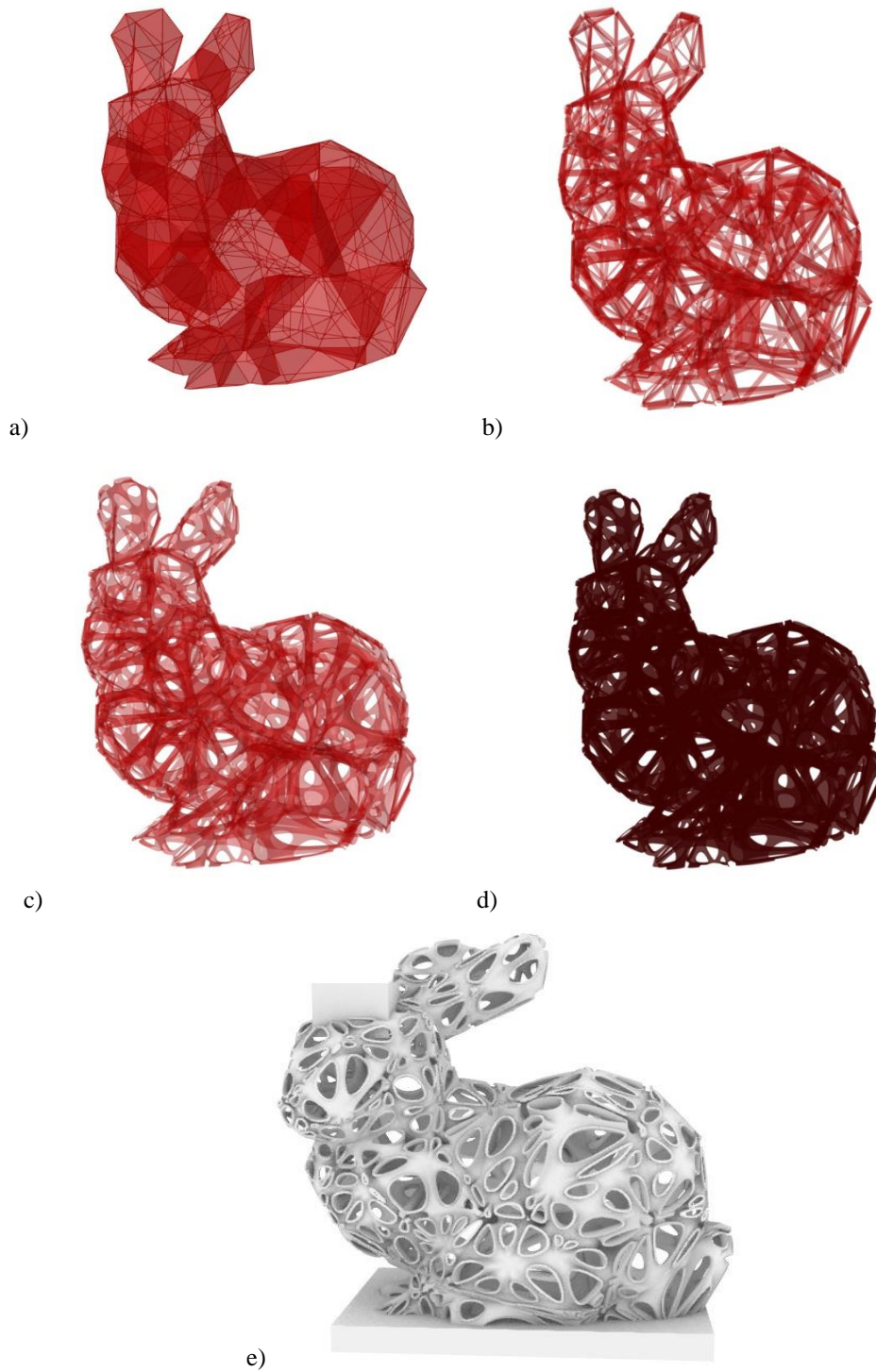


Figure 4.2. Manufacturing modification process of the Bunny-Head model. a) the resultant 3D Voronoi Bunny model, b) 1st degree spongy Bunny model, c) 3rd degree Catmull-Clark Subdivided Bunny model, d) 0.8 mm constant wall thickness Bunny model and e) the final experimental Bunny-Head model.

Following sub-section presents the random and the optimized 3D models for four different test cases; Bunny-Head model, Bunny-Back model, ATLAS model and Femur model.

4.3. Models

These models are constructed for the simple compression experiments. The defined systems, resultant colour fields, critical regions and cell distributions for the mentioned models are shown below in Figure 4.3, Figure 4.4, Figure 4.5 and Figure 4.6. Also, dimensions of the geometries are tabulated in following table. Due to the fact that shape of the models does not allow us to list the exact dimensions of these geometries, the dimensions of the bounding box of each model is tabulated.

Table 4.1. *Bounding box dimensions of the 3D models.*

Name of Model	X (mm)	Y (mm)	Z (mm)
Bunny	150	150	120
Atlas	140	70	70
Femur	150	31	32

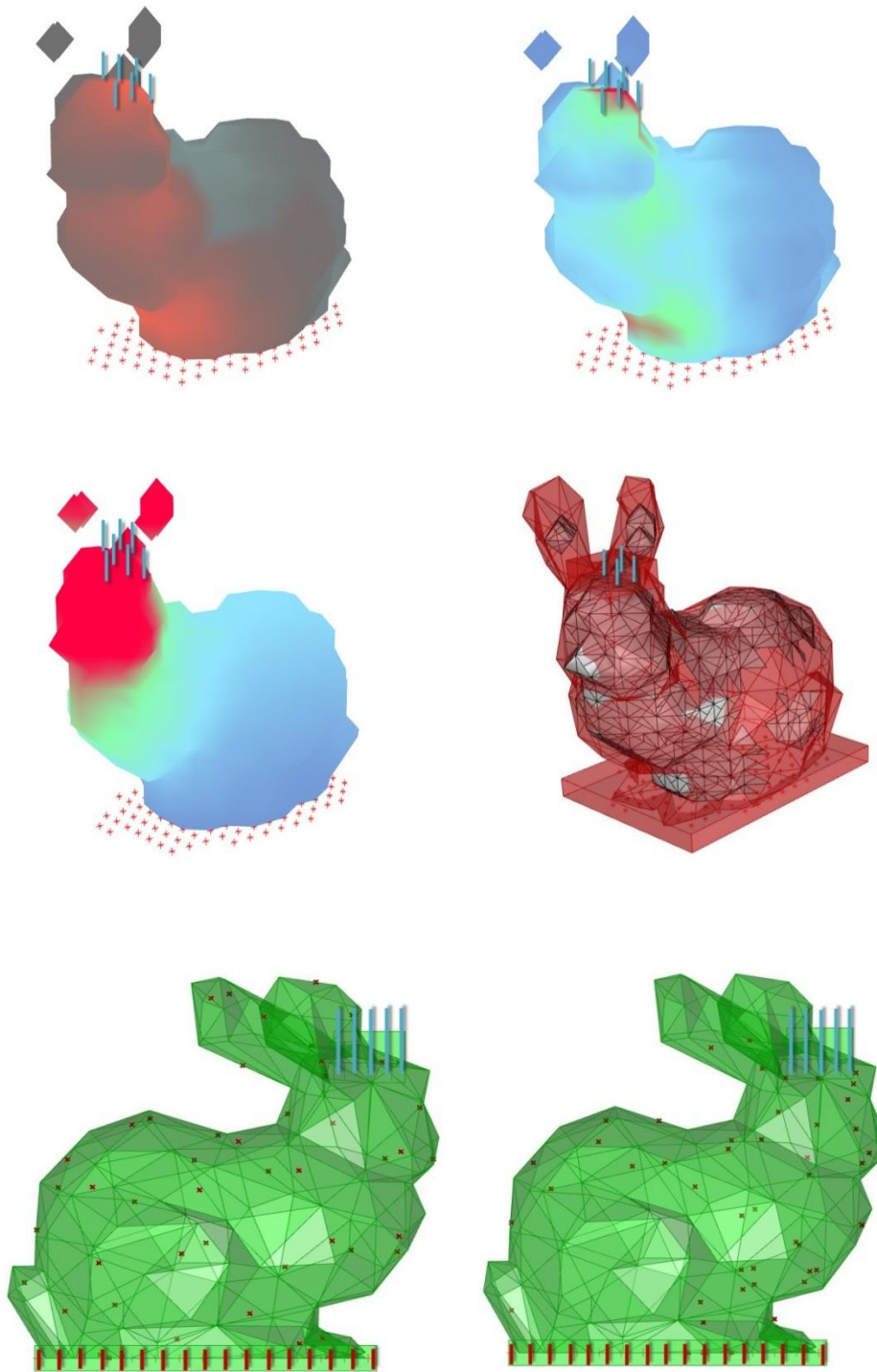


Figure 4.3. Bunny-Head model is supported at bottom (red dots) and loaded at head portion (blue lines). Principal stress, Von-Mises stress and deflection visualizations are given. Middle right represents the critical mesh nodes. Bottom row illustrates the distributions of random and optimized Voronoi seeds.

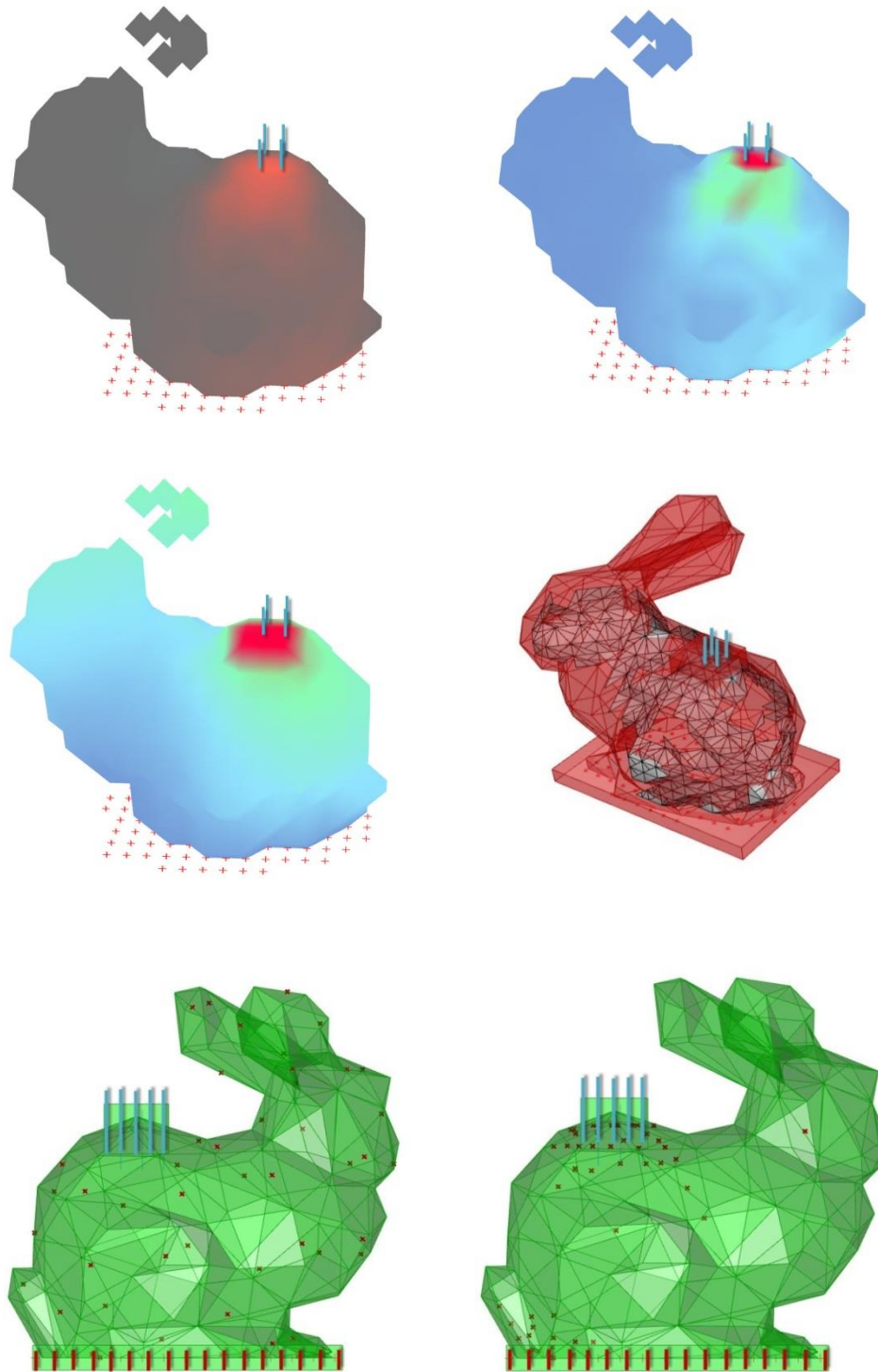
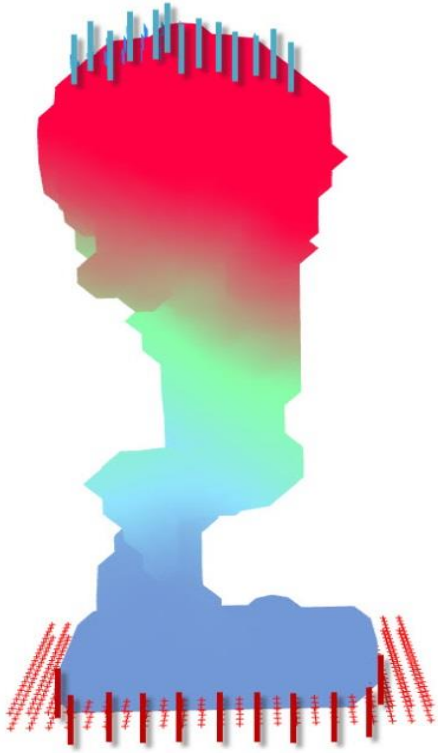
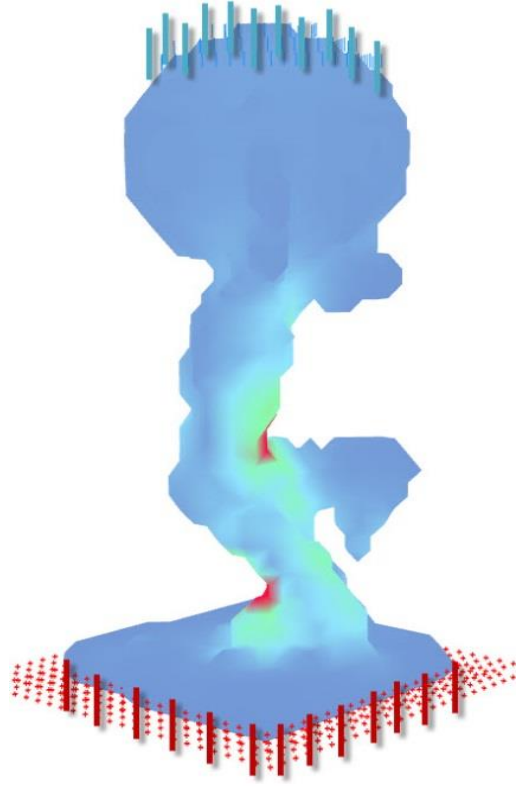
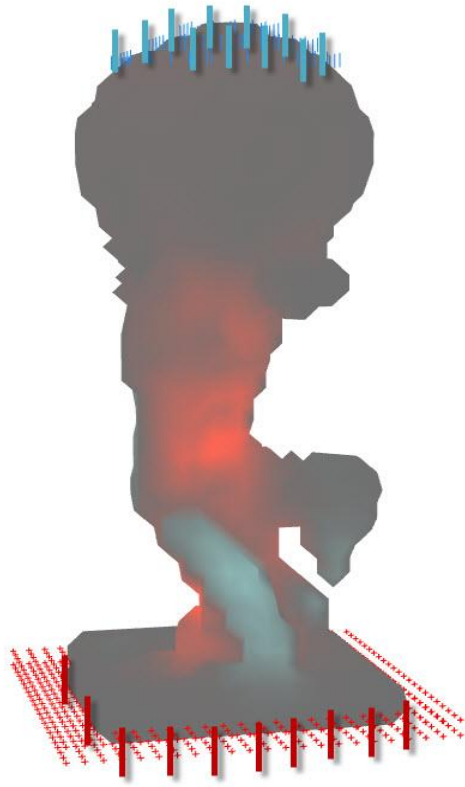


Figure 4.4. Bunny-Back model is supported at bottom (red dots) and loaded at back portion (blue lines). Principal stress, Von-Mises stress and deflection visualizations are given. Middle right represents the critical mesh nodes. Bottom row illustrates the distributions of random and optimized Voronoi seeds.



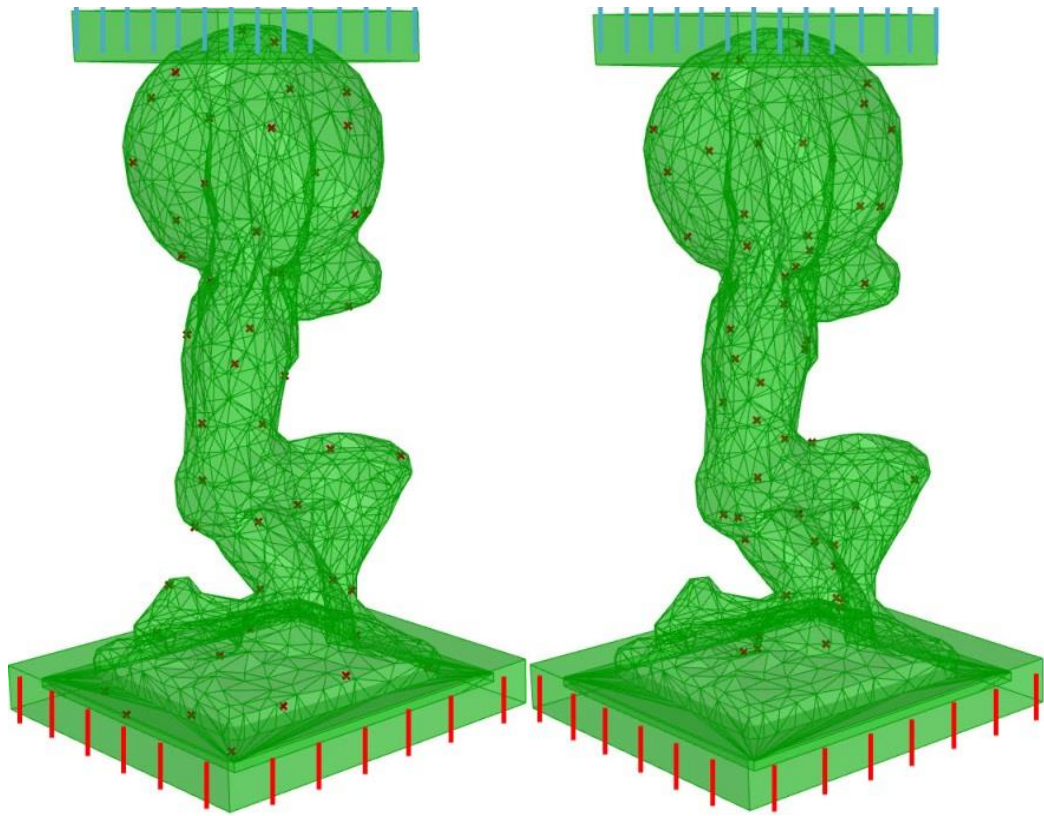


Figure 4.5. ATLAS model is supported at bottom (red lines) and loaded at top portion (blue lines). Principal stress, Von-Mises stress and deflection visualizations are given. Middle right represents the critical mesh nodes. Bottom row illustrates the distributions of random and optimized Voronoi seeds.

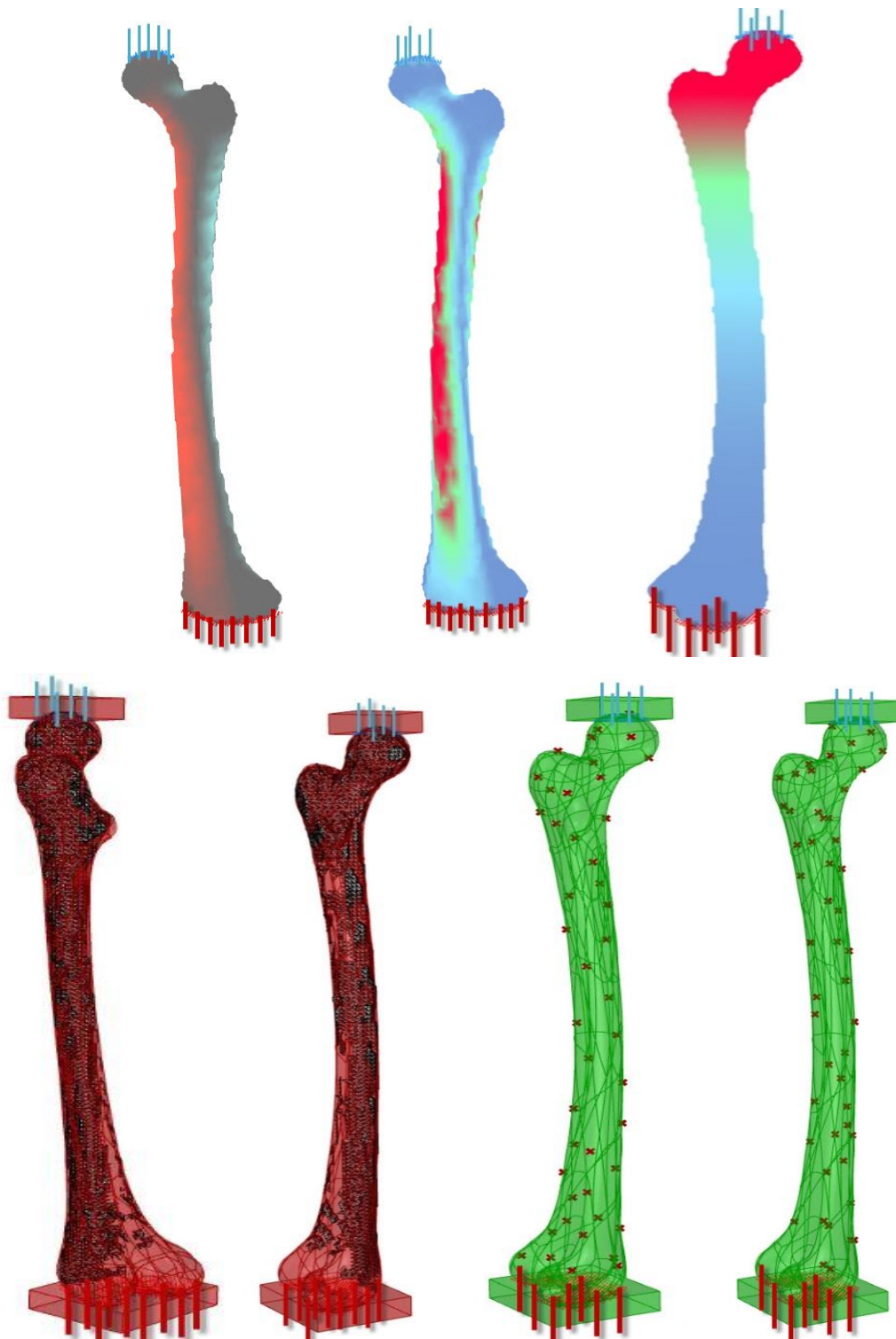


Figure 4.6. Femur model is supported at bottom (red lines) and loaded at top portion (blue lines). Principal stress, Von-Mises stress and deflection visualizations are given. Bottom row represents the critical mesh nodes and Voronoi distributions for random and optimized models.

By setting penalization factor as 2.5, target density as 0.4 and smoothing factor as 0.1, after numbers of TO iterations, 50 Voronoi sites are populated and infill patterns are constructed for optimized geometries. Then, the algorithm applies iterations of FEA and Galapagos in combination on these geometries by changing both numbers and the locations of the Voronoi seeds to find the optimum distributions. As it is mentioned before, the number range is set to 50 and the change resolution is 5 Voronoi seeds. Among 10 possible Voronoi locations for each number iteration genetic algorithm deals with 100 possible scenarios to find the mechanically the stiffest optimized geometry. Also, second genetic algorithm iterates the random distribution to find the weakest geometry among 25 possible locations of Voronoi seeds. Thus, the maximum expected performance is calculated. Finally, eight 3D models are constructed and the mechanical performances together with the maximum deflections of these close shell geometries are compared. Important values are tabulated below.

Table 4.2. *Expected performances of the close shell 3D models.*

Name of Model	Type of Model	Max. Deflection (mm)	Performance Improvement (%)
Bunny-Head	Random	0.423621	30.2
	Optimized	0.295631	
Bunny-Back	Random	0.173330	26.9
	Optimized	0.126636	
Atlas	Random	0.375044	70.7
	Optimized	0.109918	
Femur	Random	2.788676	52.1
	Optimized	1.334650	

Last part of the automated algorithm is manufacturing modifications. FFF type 3D printer needs support structures to print internally complex Voronoi infill. For this reason, 3rd degree Catmull-Clark subdivision is employed on close-shell models to create openings for decomposing the support structures. As a result, spongy shell models are obtained, which also gives natural appearance to naturally inspired 3D

Voronoi models. Then, spongy mesh models are thickened in accordance with the nozzle diameter of the 3D printer in use which is 0.2 mm. Finally, load and support regions are added onto thickened models to make the analytic and experimental models similar. In addition, these additional regions make the models stable during the compression experiments. Manufacturing modifications of rests of the models are illustrated in Figure 4.7, Figure 4.8 and Figure 4.9.

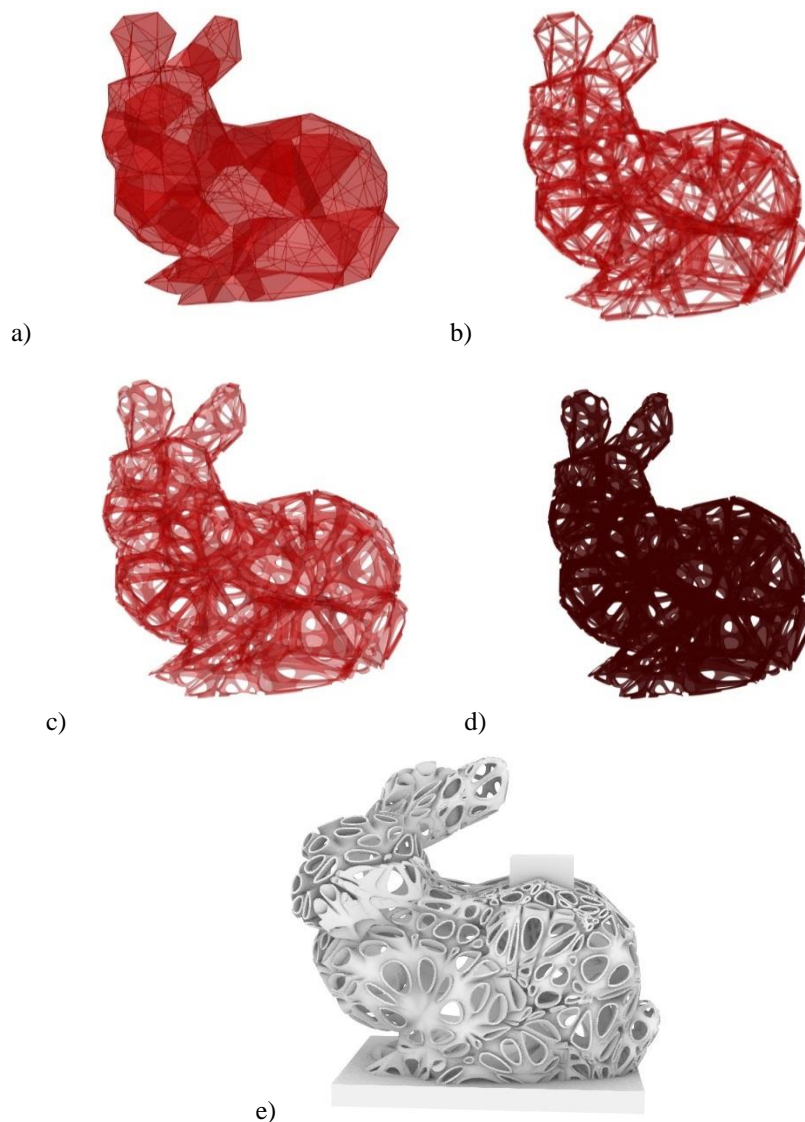


Figure 4.7. Manufacturing modifications of the Bunny-Back model. a) close-shell Voronoi model, b) 1st degree spongy model, c) 3rd degree spongy model, d) thickened model and e) experimental model.

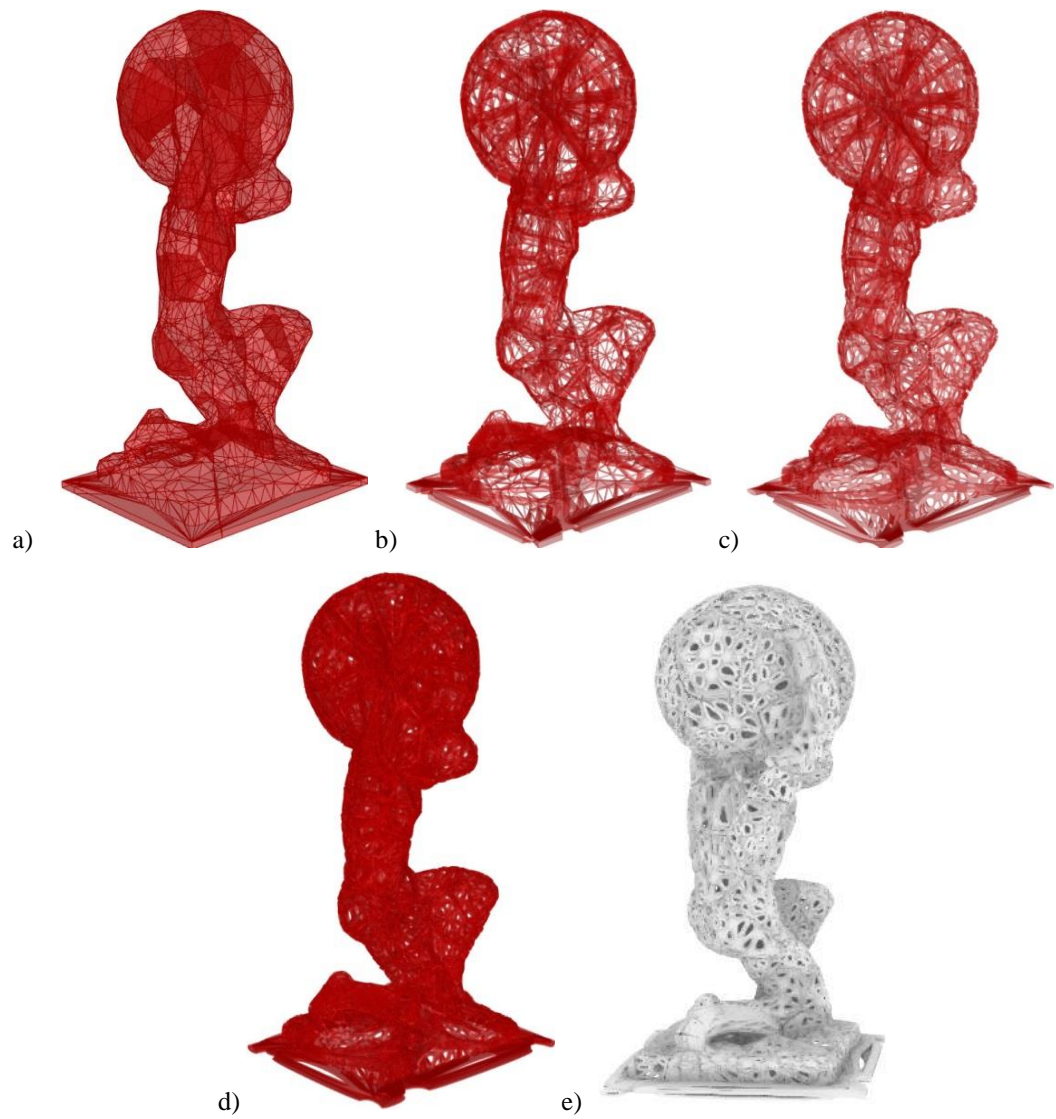


Figure 4.8. Manufacturing modifications of the ATLAS model. a) close-shell Voronoi model, b) 1st degree spongy model, c) 3rd degree spongy model, d) thickened model and e) experimental model.

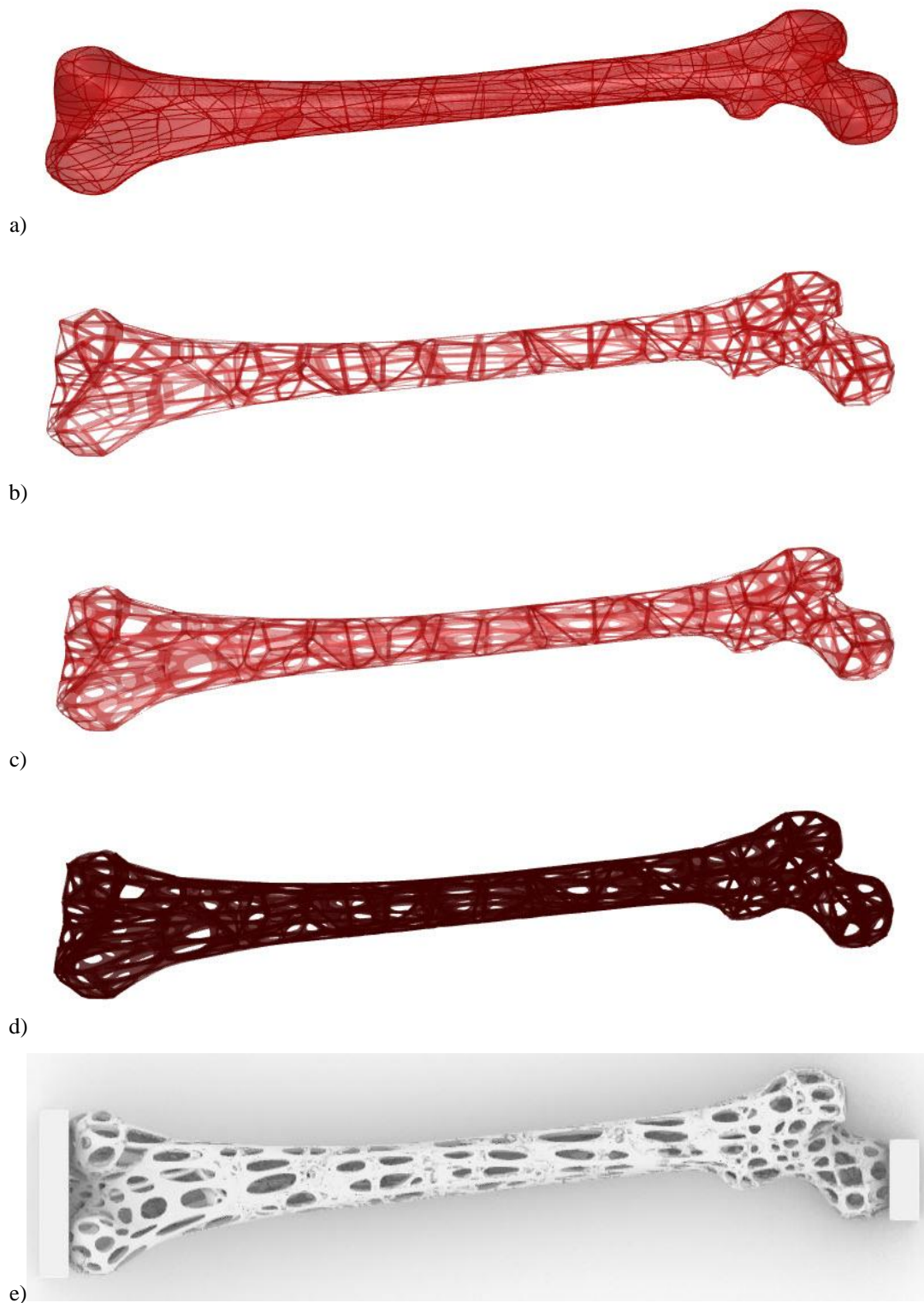


Figure 4.9. Manufacturing modifications of the Femur model. a) close-shell Voronoi model, b) 1st degree spongy model, c) 3rd degree spongy model, d) thickened model and e) experimental model.

To understand the effects of the manufacturing modifications on mechanical performance of the models, our algorithm numerically analyzes the spongy models. FEM of spongy models are shown in Figure 4.10. Compared to close-shell models, spongy models have deficiency in mechanical performance in terms of maximum deflection values due to the fact that manufacturing operations significantly lowers the overall mass values. However, for each case, optimized spongy Voronoi infill patterns exhibits stiffer mechanical response against random spongy Voronoi infills. Each spongy model is meshed using planar shell elements with the size of 0.5 mm at most. Support / load conditions are defined exactly same with FEM of the close-shell models. For spongy models, total amount of force is evenly distributed to each node that is placed within the load region. Similarly, nodes within the support region are defined as support points. Thus, load / support conditions of close-shell models are reflected on spongy FEMs. Under same amount of load, the deflection values of both spongy and close-shell models are tabulated firstly. Then, the weight reduction percentage due to manufacturing modifications and mechanical performances of random and optimized spongy models are given.

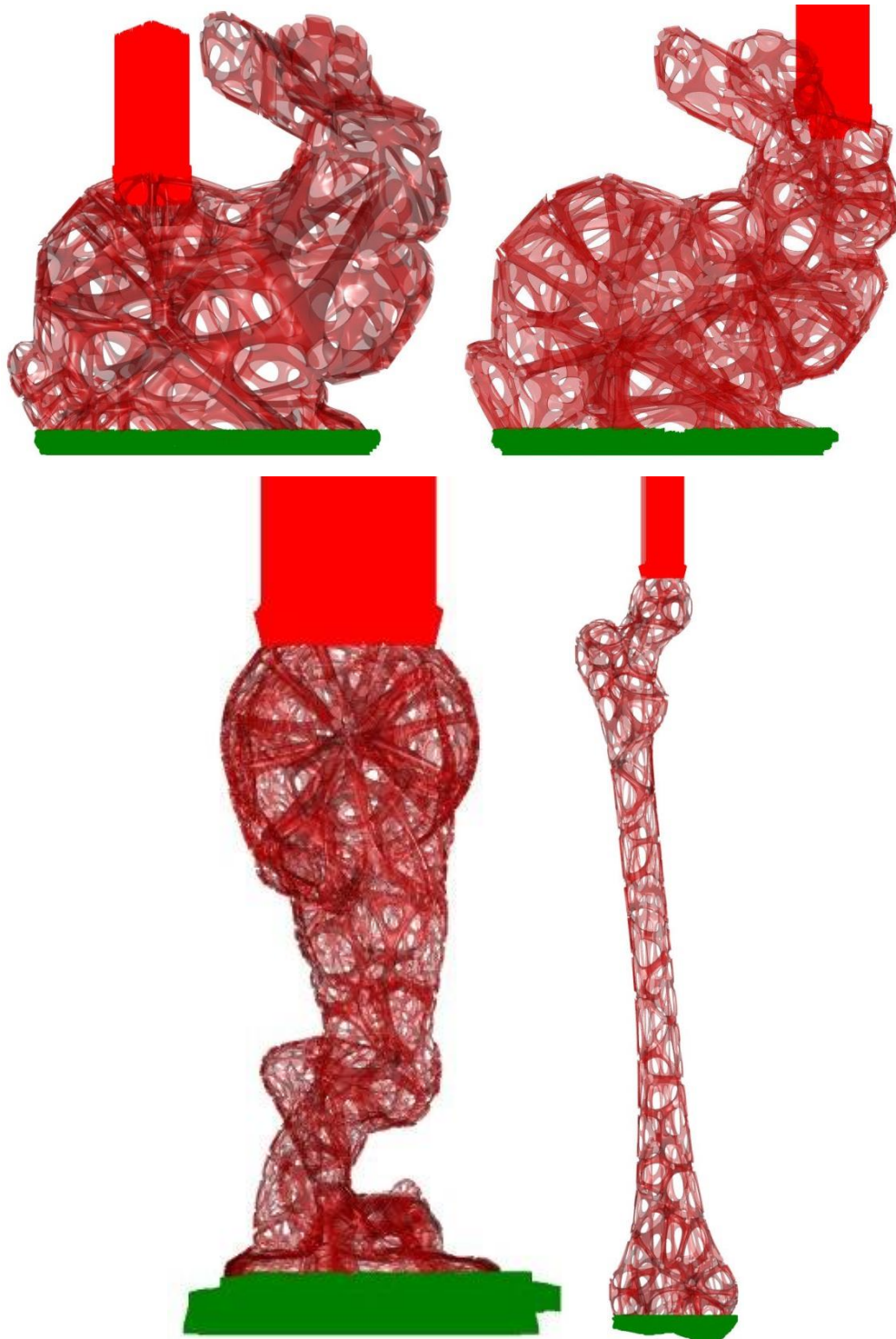


Figure 4.10. FEM of spongy models. Red lines represent loaded nodes and green dots represent supported nodes.

Table 4.3. Deflection comparisons of the 3D close-shell and spongy models.

Name of Model	Type of Model	Max. Deflection of Close Shell Models (mm)	Max. Deflection of Spongy Models (mm)
Bunny-Head	Random	0.423621	0.537366
	Optimized	0.295631	0.461295
Bunny-Back	Random	0.173330	0.336122
	Optimized	0.126636	0.042513
Atlas	Random	0.375044	0.894588
	Optimized	0.109918	0.783204
Femur	Random	2.788676	3.764797
	Optimized	1.334650	1.195775

Table 4.4. Weight reduction and performance comparisons of the 3D close shell and spongy models.

Name of Spongy Model	Weight Reduction of Spongy Models w.r.t. Close-Shell Models (%)	Performance Improvement of Optimized Spongy Models w.r.t. Random Spongy Models (%)
Bunny-Head-Optimized	57.3	14.2
Bunny-Head-Random	57.5	
Bunny-Back-Optimized	49.4	87.4
Bunny-Back-Random	57.4	
Atlas-Optimized	40.2	12.5
Atlas-Random	44.0	
Femur-Optimized	18.1	68.2
Femur-Random	56.2	

Lastly, end products are subjected to mesh repairing operations to become applicable with the slicing algorithm of the 3D printer. It is observed that .stl models of the 3D models are sometimes problematic due to complex internal details. Some openings due to thickening operations are observed between meshes and these openings prevent the slicing operation. For the repairing purposes, ANSA, CFD analyzer and pre-processor v19.0.2 software, is used [59]. Femur .stl models are transferred into software and variable wrapping operation is performed by setting minimum mesh resolution as 0.2 mm in order to close the openings between meshes. Results are checked in Ultimaker Cura v.4.2.1, a slicing algorithm, by slicing under the set of possible slice thicknesses [60]. The mentioned openings and problematic meshes are illustrated for the tip part of Femur model in Figure 4.11. In addition, same region of the reconstructed part is also shown. Finally, constructed Femur models are ready for the printing and experimental procedures.

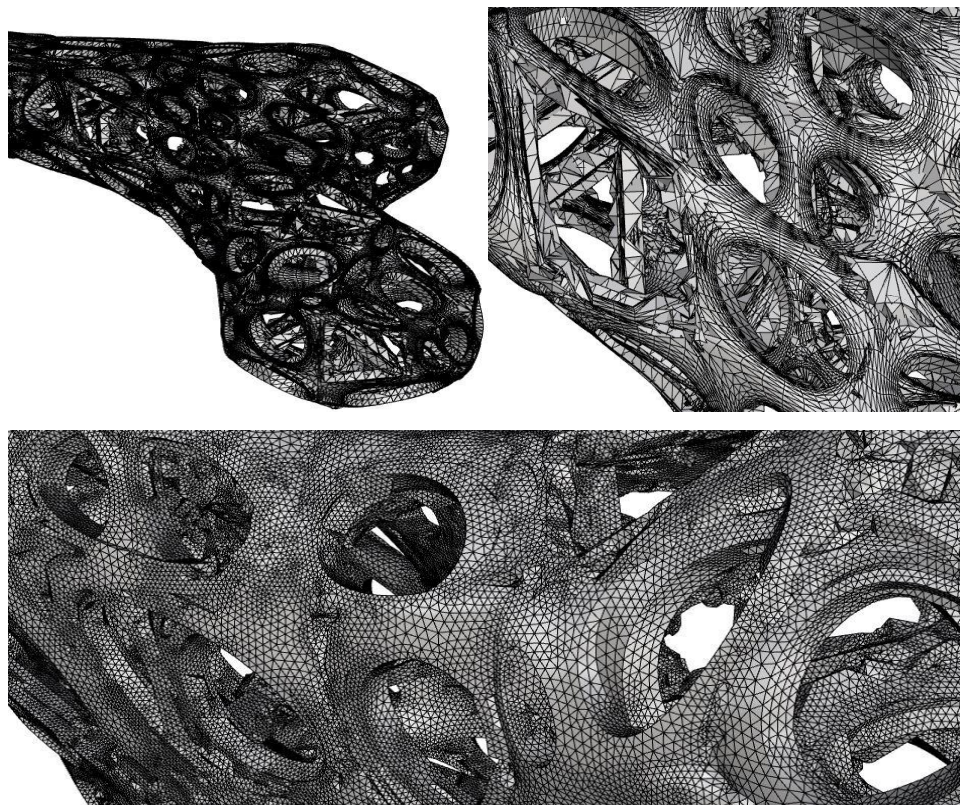


Figure 4.11. End model of the Femur. First row shows the mesh openings and problematic meshes. Second row illustrates the same region after repairing operations.

By setting wall thickness as constant 0.8 mm, both optimized and random Femur models are printed by Ultimaker 3 Extended printing machine. Similar to previous work, PLA material is used for printing and support material is canceled by taking the advantage of slender geometry of the Femur model. It is observed crack propagation during printing at the slender neck of the random Femur model. The reasons of this incident are due to head movement of printer and vibration it creates, lack of support material and structural support it gives during printing and insufficient thickness of the walls.

4.4. Limitations of Methodology 3D and Possible Future Directions

Regarding the future works, similar to previous chapter, the mechanical properties of the printing material should be implemented during FEA stage of the automated algorithm to predict real behaviour of the models under defined load/support conditions. Furthermore, rather than defining the same number of Voronoi seeds into given 3D geometry which is 50 in this work, a study should be performed to obtain an optimal number of Voronoi seeds in given 3D geometry. In other words, a correlation between the overall volume of the design and the number of Voronoi seeds should be investigated. This is because; geometric complexity significantly increases in small 3D models as the number of Voronoi seeds is increased. Thus, an extra operation that modifies the output of the proposed algorithm to make it printable model is required. Specifically, additional work performed for Femur models in ANSA creates conflict with the novel contribution of this work that is maintaining the automation during whole process. Alternatively, it is possible to scale up the geometrically complex models while keeping the total number of Voronoi seeds to maintain the contribution of this work.

It is also necessary to perform experiments on end products of the proposed algorithm to validate the performance of the approach. To do so, firstly wall thicknesses of the models should be increased whether the printing procedure is carried on w/o support material. As it is stated previously, narrow neck of the random Femur model did not

handle the external forces due to vibration that print head creates and additional weights of the top layers. On the other hand, numerically stiffer optimized Femur model could sustain these external forces during printing and it is printed perfectly. Printed end products of Femur models are shown in Figure 4.12. Additionally, by using regular infills, each 3D model should be printed exactly with the same weight of counter Voronoi infills. Furthermore, those specimens should also be tested experimentally. Consequently, the performance of the proposed methodology can be compared with the results of the standard linear infills and effect of irregularity can be investigated.

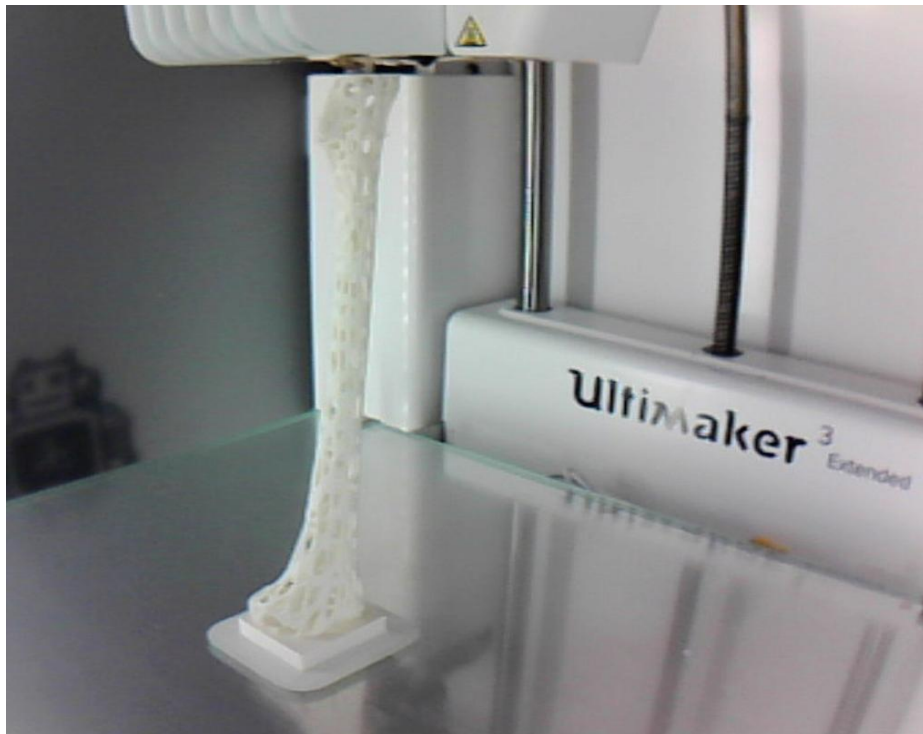


Figure 4.12. Printed Femur models. First image shows the printing process of random Femur model. Second image illustrates the printed artefacts. Left Femur has random Voronoi infill and has crack around narrow neck that is marked by green. Right Femur has optimized Voronoi infill. Behind the left one, a failed Femur model is shown due to thin wall which is constant 0.4 mm.

CHAPTER 5

CONCLUSIONS & FUTURE WORKS

5.1. Conclusions

In this thesis study it is proposed that naturally inspired Voronoi formations are used to construct mechanically improved interior infill patterns for 2.5D and 3D models. Firstly, manual procedure is carried on two different case studies to reveal the advantages of the proposed approach on 2.5D environment. 3D systems are designed by setting load and support conditions and models are subjected to TO to reveal the load carrying regions. Then, critical region is manually exposed to image processing to visualize them as sketch in 2D. Resultant sketch is used to construct 2D Voronoi infill pattern by implementing the fact that material amount must be maximized in critical regions. For this purpose, fixed number of Voronoi seeds is populated in critical regions and remaining regions are constructed by fewer amounts. Thus, overall outer shape is kept consistent with the design geometry while keeping it lightweight and stiff. Meantime, another lightweight-design-geometry is constructed with the same amount of Voronoi seeds without any intervene. Resultant geometries are compared numerically and it is concluded that proposed approach is useful to get lightweight yet stiffer end products. In addition, optimized Voronoi infill exhibits higher stiffness in comparison with the random Voronoi infill.

Secondly, a novel automated algorithm is proposed to carry the previous procedure in 2.5D. The algorithm is constructed in Rhinoceros 6 – Grasshopper environment with Millipede and Karamba 3D plug-ins and it is fed by few inputs. User defines boundary, load and support regions with conditions and algorithm gives the following outputs; ready-to-print random Voronoi infill and optimized Voronoi infill data. Under the specific load and support conditions, TO determines the critical regions within the structure and the algorithm populates Voronoi seeds in accordance with the design requirements. Then, FEA is performed on the generated geometries and the genetic

algorithm finds the optimum result for better mechanical performances. The method is employed on three different test scenarios to reveal the flexibility of the approach. Performance of the proposed scheme is elaborated through the test results and the analysis. The results indicate that the method is applicable for generating optimized Voronoi infill patterns in a given geometry. Additionally, proposed infills are experimentally compared with regular infills. Overall, the optimized Voronoi infill pattern exhibited higher mechanical performance than the random Voronoi infill patterns and regular infill pattern.

Thirdly, another novel automated algorithm is proposed to carry the similar procedure in 3D. Previous steps are taken for 3D models and additionally, manufacturing modifications are improved to sustain complexity of 3D environment. Analytical results indicate that optimized Voronoi infill patterns are exhibited significantly higher mechanical performance than the random Voronoi infill patterns. Different than the second work, experiments were not performed due to manufacturing and time limitations. Although, two Femur models having random and optimized infills are printed, experimental procedure is left to future works.

5.2. Future Works

Regarding the future works, the proposed 2.5D and 3D methodologies can be improved in the manner of FEA predictions, since; material properties of PLA were not implemented in FEA procedures. Thus, iterations of genetic algorithm can converge precisely into optimum interior Voronoic structures for each case. Secondly, experimental validation should be performed on 3D results by scaling-up the models and increasing the wall thickness of the artefacts, which are the current manufacturing limitations. Additionally, 3D models with regular infill patterns should be manufactured and experimentally tested against Voronoi infill models. Furthermore, rather than using PLA for Femur models, Ti6Al4v material can be used for printing and these models can be subjected to experiments. The reason for this future work is that proposed porous Femur model is similar to current bio-implants. It is very

important to validate the mechanical performance of the Femur model with experiments. Hence, it is possible that the idea behind the work and the proposed automated algorithm may enlighten the bio-medical applications.

REFERENCES

- [1] Gibson, D. Rosen and B. Stucker, “Additive Manufacturing Technologies, 3D Printing, Rapid Prototyping and Direct Digital Manufacturing” Second Edition, pp. 4-7.
- [2] S, A. M., Mello, V. M., Rodriguez Echavarria, K., Covill, D. (2015). Adaptive voids: primal and dual adaptive cellular structures for additive manufacturing. *Visual Computer*, 31(6), 799-808.
- [3] Gibson, L. J., Ashby, M. F. (1999). *Cellular solids: structure and properties*. Cambridge University Press.
- [4] Kou, X. Y., Tan, S. T. (2010). A simple and effective geometric representation for irregular porous structure modeling. *Computer-Aided Design*, 42(10), 930-941.
- [5] J. Wu, N. Aage, R. Westermann, O. Sigmund (2018). Infill optimization for additive manufacturing-approaching bone-like porous structures. *ACM Transactions on Graphics (TOG)*, 24(2), 1127.
- [6] Al, C. M., Yaman, U. (2018, May). An automated design and fabrication pipeline for improving the strength of 3Dprinted artifacts under tensile loading. In *AIP Conference Proceedings*(Vol. 1960, No. 1, p. 140001). AIP Publishing.
- [7] Fantini, M., Curto, M., De Crescenzo, F. (2016). A method to design biomimetic scaffolds for bone tissue engineering based on Voronoi lattices. *Virtual and Physical Prototyping*, 11(2), 77-90.
- [8] Stava, O., Vanek, J., Benes, B., Carr, N., Mch, R. (2012). Stress relief: improving structural strength of 3D printable objects. *ACM Transactions on Graphics (TOG)*, 31(4), 48.
- [9] Zhao, J., Zhang, M., Zhu, Y., Li, X., Wang, L., Hu, J.(2019). A novel optimization design method of additive manufacturing oriented porous structures and experimental validation. *Materials Design*, 163, 107550.
- [10] Wu, J., Wang, C. C., Zhang, X., Westermann, R. (2016). Self-supporting rhombic infill structures for additive manufacturing. *Computer-Aided Design*, 80, 32-42.
- [11] Martinez, J., Dumas, J., Lefebvre, S. (2016). Procedural voronoi foams for additive manufacturing. *ACM Transactions on Graphics (TOG)*, 35(4), 44.
- [12] Martinez, J., Hornus, S., Song, H., Lefebvre, S. (2018). Polyhedral Voronoi diagrams for additive manufacturing. *ACM Transactions on Graphics (TOG)*, 37(4), 129.

- [13] Provaggi, E., Capelli, C., Rahmani, B., Burriesci, G., Kalaskar, D. M. (2019). 3D printing assisted finite element analysis for optimising the manufacturing parameters of a lumbar fusion cage. *Materials Design*, 163, 107540.
- [14] Kandemir, V., Dogan, O., Yaman, U. (2018). Topology optimization of 2.5 D parts using the SIMP method with a variable thickness approach. *Procedia Manufacturing*, 17,29-36.
- [15] Qiang Du, Max Gunzburger, Lili Ju (2010). Advances in Studies and Applications of Centroidal Voronoi Tesellations. *Numer. Math. Theor. Meth. Appl.*, 3(2), pp. 119-142.
- [16] Qiang Du, Desheng Wang (2005). Anisotropic Centroidal Voronoi Tesellations and Their Applications. *SIAM J. SCL. COMPUT.*, 26(3), pp. 737-761.
- [17] Qiang Du, Vance Faber, Max Guncburger (1999). Centroidal Voronoi Tesellations: Applications and Algorithms. *SIAM Review*, 41(4), pp. 637-676.
- [18] D.J. Brackett, I.A. Ashcroft, R.D. Wildman, R.J.M. Hague (2014). An error diffusion based method to generate functionally graded cellular structures. *Computers and Structures*, 138, 102-111.
- [19] X.Y Kou, S.T. Tan (2012). Microstructural modelling of functionally graded materials using stochastic Voronoi Diagram and B-Spline representations. *International Journal of Computer Integrated Manufacturing*, 25:2, 177-188.
- [20] Jeff T. Gostick (2013). Random pore Network Modeling of Fibrous PEMFC Gas Diffusion Media Using Voronoi and Delaunay Tesellations. *Journal of the Electrochemical Society*, 160 (8) F731-F743.
- [21] Li-Ke Ma, Yizhong Zhang, Yang Liu, Kun Zhou, and Xin Tong. 2017. Computational Design and Fabrication of Soft Pneumatic Objects with Desired Deformations. *ACM Trans. Graph.* 36, 6, Article 239.
- [22] Skouras, M., Thomaszewski, B., Coros, S., Bickel, B., Gross, M. 2013. Computational Design of Actuated Deformable Characters. *ACM Trans. Graph.* 32, 4, Article 82.
- [23] Prévost, R., Whiting, E., Lefebvre, S., Sorkine-Hornung, O. 2013. Make It Stand: Balancing Shapes for 3D Fabrication. *ACM Trans. Graph.* 32, 4, Article 81.
- [24] Malomo, L., Pietroni, N., Bickel, B., Cignoni, P. 2016. FlexMolds: Automatic Design of Flexible Shells for Molding. *ACM Trans. Graph.* 35, 6, Article 223.
- [25] A.N. Christiansen, J.A. Baerentzen, M. Nobel-Jorgensen, N. Aage, O. Sigmund 2015. Combined shape and topology optimization of 3D structures. *Computers & Graphics* 46, 25-35.

- [26] Wang, W., Wang, T., Yang, Z., Liu, L., Tong, X., Tong, W., Deng, J., Chen, F., Liu, X. 2013. Cost-effective Printing of 3D Objects with Skin-Frame Structures. *ACM Trans. Graph.* 32, 6, Article 177.
- [27] H. Zhao, F. Gu, Qi-Xing Huang, J. Garcia, Y. Chen, C. Tu, B. Benes, H. Zhang, D. Cohen-Or, B. Chen 2016. Connected fermat spirals for layered fabrication. *ACM Trans. Graph.*, Vol. 35, No. 4, Article 100.
- [28] A. Garcia-Dominguez, J. Claver, M. A. Sebastian 2017. Methodology for the optimization of work pieces for additive manufacturing by 3D printing. *Procedia Manufacturing*, 13, 910-915.
- [29] L.E. Murr, S.M. Gaytan, F. Medina, E. Martinez, J.L. Martinez, D.H. Hernandez, B.I. Machado, D.A Ramirez, R.B. Wicker, 2010. Characterization of Ti-6Al-4V open cellular foams fabricated by additive manufacturing using electron beam melting. *Materials Science and Engineering, A* 527, 1861-1868.
- [30] Panetta, J., Zhou, Q., Malomo, L., Pietroni, N., Cignoni, P., Zorin, D. 2015. Elastic Textures for Additive Fabrication. *ACM Trans. Graph.* 34, 4, Article 135.
- [31] D. Li, W. Liao, N. Dai, G. Dong, Y. Tang, Yi Min Xie, 2018. Optimal design and modeling of gyroid-based functionally graded cellular structures for additive manufacturing. *Computer Aided Design*, 104, 87-99.
- [32] M. Pham, C. Liu, I. Todd, J. Lertthanasarn, 2019. Damage tolerant architected materials inspired by crystal microstructure. *Springer Nature*, 565, 305.
- [33] L. Cheng, P. Zhang, E. Biyikli, J. Robbins, 2017. Efficient design optimization of variable-density cellular structures for additive manufacturing: theory and experimental validation. *Rapid Prototyping journal*, 23, 4, 660-677.
- [34] G. Campoli, M.S. Borleffs, S. Amin Yavari, R. Wauthle, H. Weinans, A.A. Zadpoor, 2013. Mechanical properties of open-cell metallic biomaterials manufactured using additive manufacturing. *Materials and Design*, 49, 957-965.
- [35] Y. Han, W.F. lu, 2018. Optimization design of nonuniform cellular structures for additive manufacturing. *Proceedings of the ASME, MSEC2018-6450*.
- [36] D.S.J. Al-Saedi, S.H.Masood, M. Faizan-Ur-Rab, A. Alomarah, P. Ponnusamy, 2018. Mechanical properties and energy absorption capability of functionally graded F2BCC lattice fabricated by SLM. *Materials and Design*, 144, 32-44.
- [37] Li-Jia Feng, Lin-Zhi Wu, Guo-Cai Yu, 2016. An Hourglass truss lattice structure and its mechanical performances. *Materials and Design*, 99, 581-591.
- [38] I. Ullah, J. Elambasseril, M. Brandt, S. Feih, 2014. Performance of bio-inspired Kagome truss core structures under compression and shear loading. *Composite Structures*, 118, 294-302.

- [39] A. Amendola, E. Hernandez-Nava, R. Goodall, L. Todd, R.E. Skelton, F. Fraternali, 2015. On the additive manufacturing, post-tensioning and testing of bi-material tensegrity structures. *Composite Structures*, 131, 66-71.
- [40] New Balance sport good, <https://formlabs.com/customer-stories/newbalance/>, last accessed: August 08, 2019.
- [41] J. Ying, L. Lu, L. Tian, X. Yan, B. Chen, 2018. Anisotropic porous structure modeling for 3D printed objects. *Computers and Graphics*, 70, 157-164.
- [42] C. Schroeder, W.C. Regli, A. Shokoufandeh, W. Sun, 2005. Computer-aided design of porous artifacts. *Computer-Aided Design*, 37, 339-353.
- [43] A. Rainer, S.M. Giannitelli, D. Accoto, S. De Porcellinis, E. Guglielmelli, M. Trombetta, 2011. Load-adaptive scaffold architecturing; a bioinspired approach to the design of porous additively manufactured scaffolds with optimized mechanical properties. *Annals of Biomedical Engineering*, 40, 4, pp. 966-975.
- [44] J. Martinez, H. Song, J. Dumas, S. Lefebvre, 2017. Orthotropic k-nearest foams for additive manufacturing. *ACM Transactions on Graphics*, 36, 4, 121.
- [45] X., Zhang, Y. Xia, J. Wang, Z. Yang, C. Tu, W. Wang, 2015. Medial axis tree-an internal supporting structure for 3D printing. *Computer Aided Geometric Design*, 35-36, 149-162.
- [46] S. Gomez, M.D. Vlad, J. Lopez, E. Fernandez, 2016. Design and properties of 3D scaffolds for bone tissue engineering. *Acta Biomaterialia*, 42, 341-350.
- [47] Lu, L., Sharf, A., Zhao, H., Wei, Y., Fan, Q., Chen, X., Savoye, Y., Tu, C., Cohen-Or, D., Chen, B. 2014. Build-to-Last: Strength to Weight 3D Printed Objects. *ACM Trans. Graph.* 33, 4, Article 97.
- [48] L.E. Murr, S.M. Gaytan, F. Medina, H. Lopez, E. Martinez, B.I. Machado, D.H. Hernandez, L. Martinez, M.I. Lopez, R.B. Wicker, J. Brackie, 2010. Next-generation biomedical implants using additive manufacturing of complex, cellular and functional mesh arrays. *Phil. Trans. R. Soc. A*, 368, 1999-2032.
- [49] D.A. Ramirez, L.E. Murr, S.J. Li, Y.X. Tian, E. Martinez, J.L. Martinez, B.I. Machado, S.M. Gaytan, F. Medina, R.B. Wicker, 2011. Open-cellular copper structures fabricated by additive manufacturing using electron beam melting. *Materials Science and Engineering, A* 528, 5379-5386.
- [50] H.X. Zhu, S.M. Thorpe, A.H. Windle, 2006. The effect of cell irregularity on the high strain compression of 2D Voronoi honeycombs. *International Journal of Solids and Structures*, 43, 1061-1078.
- [51] Oscar E., Sotomayor, Hareesh V., Tippur, 2014. Role of cell regularity and relative density on elastoplastic compression response of 3-D open-cell foam core sandwich structure generated using Voronoi diagrams. *Acta Materialia*, 78, 301-313.

- [52] X. yan, C. Rao, L. Lu, A. Sharf, H. Zhao, B. Chen, 2019. Strong 3D printing by TPMS injection. IEEE Transactions on Visualization and Computer Graphics.
- [53] Vidimče, K., Wang, S., Ragan-Kelley, J., Matusik, W. 2013. OpenFab: A Programmable Pipeline for Multi-Material Fabrication. ACM Trans. Graph. 32, 4, Article 136.
- [54] Grasshopper Plugin for Rhinoceros, <https://www.grasshopper3d.com/>, last accessed: February 26, 2019
- [55] Millipede Plugin for Grasshopper, <http://www.sawapan.eu/>, last accessed: February 26, 2019
- [56] Karamba3D Plugin for Grasshopper, <https://www.karamba3d.com/>, last accessed: February 26, 2019
- [57] Galapagos Executer for Grasshopper, <https://www.grasshopper3d.com/group/galapagos>, last accessed: February 26, 2019
- [58] Catmull and Clark Subdivision Executer for Grasshopper, <https://rhino.github.io/components/weaverbird/catmullClarkSubdivision.html>, last accessed: March 13, 2019
- [59] ANSA pre-processor v19.0.2, <https://www.beta-cae.com/ansa.htm>, last accessed: August 18, 2019
- [60] Ultimaker Cura v.4.2.1, <https://ultimaker.com/software/ultimaker-cura>, last accessed: August 9, 2019.
- [61] Öncel, A. C., Yaman, U. (2019, June). Generation of Optimized Voronoi Based Interior Structures for Improved Mechanical Properties. In 29th International Conference on FAIM Proceedings, Science Direct.
- [62] SIMP Methodology, DASSAULT SYSTEMS, Simulation, Topology Study, http://help.solidworks.com/2019/english/SolidWorks/cworks/c_simp_method_topology.htm, last accessed: September 24, 2019.

